Summer 2012

Electrodeposition and electrochemical reduction of epitaxial metal oxide thin films and superlattices

Zhen He

Department: Chemistry

ELECTRODEPOSITION AND ELECTROCHEMICAL REDUCTION OF EPITAXIAL METAL OXIDE THIN FILMS AND SUPERLATTICES

by

ZHEN HE

A DISSERTATION

Presented to the Faculty of the Graduate School of the

MISSOURI UNIVERSITY OF SCIENCE AND TECHNOLOGY

In Partial Fulfillment of the Requirements for the Degree

DOCTOR OF PHILOSOPHY

in

CHEMISTRY

2012

Approved by

Jay A. Switzer, Advisor
Pericles Stavropoulos
Jeffrey G. Winiarz
Manashi Nath
Wayne Huebner

PUBLICATION DISSERTATION OPTION

This dissertation has been prepared in the format used by *Journal of the American Chemical Society* and *Chemistry of Materials*. This dissertation includes one article that has been published in *Journal of the American Chemical Society*, one article that has been submitted to *Chemistry of Materials*, and one article that will be submitted to *Chemistry of Materials* soon. Paper I (on pages 41-56) has been published in *Journal of the American Chemical Society*, 133, 12358-12361 (2011). The supporting information of Paper I can be found in the Appendix A in this dissertation. Paper II (on pages 57-99) has been written for submission to *Chemistry of Materials*. The supporting information of Paper II can be found in the Appendix B in this dissertation. Paper III (on pages 100-116) has been submitted to *Chemistry of Materials*. The supporting information of Paper III can be found in the Appendix C in this dissertation. The Appendices D and E have the unpublished results that are relevant to this dissertation.

ABSTRACT

The focus of this dissertation is the electrodeposition and electrochemical reduction of epitaxial metal oxide thin films and superlattices. The electrochemical reduction of metal oxides to metals has been studied for decades as an alternative to pyrometallurgical processes for the metallurgy industry. However, the previous work was conducted on bulk polycrystalline metal oxides. Paper I in this dissertation shows that epitaxial face-centered cubic magnetite (Fe_3O_4) thin films can be electrochemically reduced to epitaxial body-centered cubic iron (Fe) thin films in aqueous solution on single-crystalline Au substrates at room temperature. This technique opens new possibilities to produce special epitaxial metal/metal oxide heterojunctions and a wide range of epitaxial metallic alloy films from the corresponding mixed metal oxides.

Electrodeposition, like biomineralization, is a soft solution processing method which can produce functional materials with special properties onto conducting or semiconducting solid surfaces. Paper II in this dissertation presents the electrodeposition of cobalt-substituted magnetite ($Co_xFe_{3-x}O_4$, $0<x<1$) epitaxial thin films and superlattices on Au single-crystalline substrates, which can be potentially used in spintronics and memory devices. Paper III in this dissertation reports the electrodeposition of crystalline cobalt oxide (Co_3O_4) thin films on stainless steel and Au single-crystalline substrates. The crystalline Co_3O_4 thin films exhibit high catalytic activity towards the oxygen evolution reaction in an alkaline solution. A possible application of the electrodeposited Co_3O_4 is the fabrication of highly active and low-cost photoanodes for photoelectrochemical water-splitting cells.

ACKNOWLEDGMENTS

I am heartily thankful to my advisor, Dr. Jay A. Switzer, for his supervision, encouragement, and support from the preliminary to the concluding level in my graduate studies. In the meantime, I also would like to thank all of my advisory committee, Drs. Pericles Stavropoulos, Jeffrey G. Winiarz, Manashi Nath, and Wayne Huebner, for their invaluable suggestions and guidance.

I also owe my deepest gratitude to the post-doctoral associates and fellow graduate and undergraduate students in Dr. Switzer's group and colleagues in the Department of Chemistry and Graduate Center for Materials Research, Dr. Jakub A. Koza, Dr. Elizabeth A. Kulp, Dr. Eric W. Bonannan, Dr. Guojun Mu, Dr. Rakesh V. Gudavarthy, Dr. Sansanee Boonsalee, Niharika Burla, Samantha Mathews, Allen Liu, Kyle Anderson, Andrew Miller, Caleb Hull, Matthew Willmering, for their valuable discussions and assistances. I also would like to make a special reference to Drs. Jon Reid and Mark Willey in Novellus Systems, Inc. for providing me an opportunity to work as an intern there in the summer of 2011.

Furthermore, I would like to thank my family, especially my parents and my wife, for their generous and consistent support throughout my life. Without them, this dissertation would not have been possible. I would also like to thank all of my friends for their friendships and helps to me.

Last but not least, I would like to acknowledge the Department of Energy (DE-FG02-08ER46518) and National Science Foundation (DMR-0504715 & DMR-1104801) for their generous financial support.

TABLE OF CONTENTS

LIST OF ILLUSTRATIONS

Page

Paper II

Paper III

LIST OF TABLES

Page

Paper II

1. INTRODUCTION

1.1. ELECTRODEPOSITION

Electrodeposition, commonly known as "electroplating," is a soft solution processing method which can produce materials with special properties onto conducting or semiconducting solid surfaces.[1] Electrodeposition is one of the most common methods of solution growth because it is simple, inexpensive, and capable of providing degrees of freedom and producing materials or nanostructures that cannot be easily accessed by high-vacuum vapor deposition methods. The morphology, orientation and chirality of the materials can be controlled through solution additives, pH or by controlling the applied potential or current density at the electrode surface.[2-6] Although some of these capabilities are also held by other methods of solution growth, such as chemical bath deposition, sol-gel processing, and hydrothermal synthesis, electrodeposition still has some unique properties including *i*) precise control of the departure from the equilibrium potential through the externally applied bias, *ii*) control of the stoichiometry of the deposited compounds and metal alloys through the applied potential or current density, and *iii*) control of the deposition rate through the applied current density.[1]

Electrodeposition can be used to produce a wide range of materials and architectures on different substrates. The materials that have been electrodeposited include metals,[7,8] metal alloys,[9,10] oxides,[1,4,11-13] magnetic materials,[7,14] and hybrid materials.[15,16] They can be controllably deposited as polycrystalline or epitaxial films, superlattices, nanocrystals with different shapes (e.g., cubes, triangles, rods, tubes, and spheres), porous networks, and chiral morphologies.[1] Switzer's group has focused on the epitaxial electrodeposition of thin films, superlattices and composites of functional

materials. The materials that have been electrodeposited by Switzer's group include *i*) metal oxides such as magnetite (Fe_3O_4),[17-22] bismuth oxide (Bi_2O_3),[23,24] cupric oxide (CuO),[4,5,25-29] cuprous oxide (Cu_2O),[13,30-35] zinc oxide (ZnO),[12,36,37] cobalt oxide (Co_3O_4), and lead dioxide (PbO_2),[38] *ii*) biominerals, such as calcite ($CaCO_3$),[39] and *iii*) metal chalcogenide semiconductors, such as lead sulfide (PbS)[40] and tin sulfide (SnS).[41] Part of this dissertation will focus on the electrodeposition of epitaxial metal oxide thin films and superlattices.

1.1.1. Electrodeposition of Metal Oxide Thin Films. The electrodeposition of metal oxide thin films generally follows electrochemical-chemical (EC) mechanisms,[42] in which two steps are involved. Initially, electrons are transferred between the electrode and the electrochemically active species in solution, driven by the applied potential or current. On the surface of an anode, electrons are transferred from the solution active species to the anode, whereas on the surface of a cathode, electrons are transferred from the cathode to the solution active species. Next, after the electron transfer process, chemical reactions occur at the electrode surface. The electron transfer process only occurs to the electrochemically active species at or near the electrode surface. The species away from the electrode will move towards it through mass transfer processes of diffusion, migration, and convection.[43] Diffusion is caused by a gradient of chemical potential (i.e., a concentration gradient). Migration only applies to charged bodies and is caused by a gradient of electrical potential (an electric field). Convection describes the fluid flow due to hydrodynamic transport caused by a density gradient or by external forces (e.g., stirring). Mass transfer processes "refill" the solution active species, which have been consumed in the electron transfer process to the electrode surface from the

bulk solution and assure that the electrochemical reactions at the electrode surface can continuously occur.

Following electrochemical-chemical mechanisms, generally, metal oxide thin films can be electrochemically deposited onto various kinds of substrates through two different routes.[1] For the first route, oxides can be produced by changing the oxidation state of the metal ions at the electrode surface (either by oxidation or reduction) followed by hydrolysis/condensation. For example, Fe_3O_4 films can be electrodeposited by oxidizing Fe(II) ions[17,18] at the electrode surface in a solution containing $(NH_4)_2Fe(SO_4)_2$ $6H_2O$ and KCH_3-COO via equation 1:

$$3Fe^{2+} + 4H_2O \rightarrow Fe_3O_4 + 8H^+ + 2e^- \quad (1)$$

Fe_3O_4 films could also be deposited by reducing Fe(III) to Fe(II)[19,42] at the electrode surface in a solution containing Fe(III)-TEA and NaOH via the following two equations:

$$Fe(III)(TEA) + e^- \leftrightarrows Fe(II)(TEA) \quad (2)$$

$$Fe(II)(TEA) + 8OH^- + 2Fe(III)(TEA) \rightarrow Fe_3O_4 + 3TEA + 4H_2O \quad (3)$$

For the second route, oxides can be formed by electrochemically changing the local pH at the electrode surface (by generating an acid or a base) to induce the hydrolysis/condensation reactions. For example, ZnO can be electrodeposited by generating either an acid or a base. ZnO, as an amphoteric compound, is soluble in both acidic and basic solutions. The calculated speciation distribution (upper figure) and

solubility (lower figure) of ZnO vs. pH in aqueous solution at 70 ℃ are shown in Figure 1.1.[37,44,45] ZnO has the lowest solubility at a pH of ~9.4. Therefore, ZnO can be electrodeposited by generating H^+ (or OH^-) ions when the pH is above (or below) 9.4 from a solution containing Zn^{2+} to induce the precipitation of ZnO on the electrode surface.

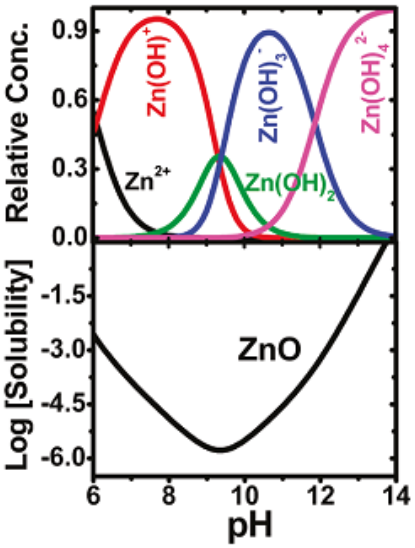

Figure 1.1. Speciation distribution (upper) and solubility (lower) of Zn(II) vs. pH in aqueous solution at 70 ℃.[37]

1.1.2. Epitaxial Electrodeposition. The term "epitaxial" (epitaxy) is used to describe a layer of a crystalline material (in most cases in the form of a thin film) grown on top of a crystalline (usually single-crystalline) substrate in an ordered fashion. In the restricted definition of epitaxy, the crystallographic orientations of a deposited film follow the crystallographic orientations of the substrate in both the in-plane and out-of-

plane directions. This usually occurs when the crystal structures and lattice parameters of the grown film and the substrate are similar. However, in the general definition, a film is epitaxial as long as the out-of-plane and in-plane orientations of the deposited film are controlled by the substrate. In this case, the orientations of the film and the substrate are not necessarily the same. The growth of the film is usually controlled by both thermodynamics and kinetics,[6] and tends to minimize the lattice mismatch between the film and the substrate. In this dissertation, general definition of epitaxy will be used.

Epitaxial growth can be easily distinguished from polycrystalline and textured growth. Polycrystalline growth usually occurs on polycrystalline substrates. The orientations of the grown films are totally random. A polycrystalline film usually has a powder diffraction pattern of the film material in the X-ray diffraction (XRD) 2θ scan and a uniform background (due to a uniform intensity of diffraction at any tilt and rotation angles) in the XRD pole figure measurement. A film of textured growth usually shows one (or several) preferred out-of-plane orientation(s) in the XRD 2θ scan, but its in-plane orientations are random, which can be exhibited by a "ring pattern" (due to more intense diffractions at the tilt angles corresponding to the preferred out-of-plane orientations) in the XRD pole figure measurement. However, an epitaxial film commonly grows with a specific out-of-plane orientation, which is controlled by the orientation of the substrate. The out-of-plane orientation of an epitaxial film does not need to match with the peak of the highest diffraction intensity in the powder diffraction pattern of the film material. The in-plane orientations of an epitaxial film are also aligned with some certain in-plane orientations of the substrate in order to minimize the lattice mismatch between the film and the substrate. An epitaxial film shows a family of peaks in the XRD

2θ scan and a "spot pattern" (showing diffraction at certain tilt and rotation angles) in the XRD pole figure measurement.

Epitaxial growth can be divided into two types: heteroepitaxy or homoepitaxy. Heteroepitaxy refers to the epitaxial growth in which the film and the substrate are of different materials. Homoepitaxy is used to describe the growth in which the film and the substrate are the same material. This method is usually used to grow a material which is more pure than the substrate or to control the doping level of the material, e.g., the growth of a doped epitaxial Si layer on a pure single-crystalline Si substrate.

Epitaxial growth has been conducted by many different techniques such as electrodeposition,[1,17,40,46] pulsed laser deposition (PLD),[47-50] molecular beam epitaxy (MBE),[51-53] chemical vapor deposition (CVD),[52,54-56] and atomic layer deposition (ALD).[57-59] Epitaxial films of metals, metal alloys, metal oxides and semiconductors such as Fe, Cu, Ni, CoFe, NiFe, Fe_3O_4, MgO, Si, and GaAs have been produced. Various kinds of single crystalline substrates have been used. Switzer's group has focused on the electrodeposition of epitaxial metal oxide thin films on single-crystalline substrates such as Au, Cu, Ni, and Si.

1.1.3. Electrodeposition of Superlattices. Superlattices are a special type of crystalline multilayer structure in which there is coherent stacking of atomic planes, and periodic modulation of the structure, or composition, or both.[60,61] The schematic of a superlattice is shown in Figure 1.2. In the superlattice shown in Figure 1.2, there are alternating layers of the material A and B. Superlattices could also be composed of alternating layers of A, B, and C, or A, B, C, and D, etc. The thickness of one period of

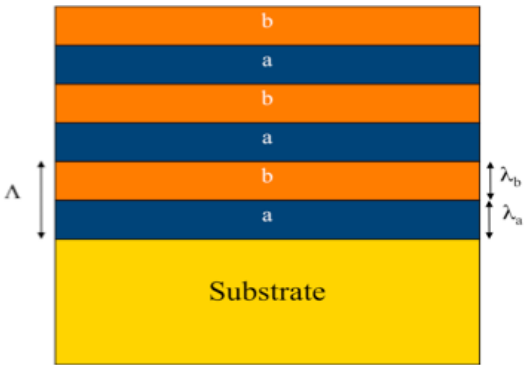

Figure 1.2. Schematic of a superlattice.

these alternating layers is called the modulation wavelength of the superlattice, labeled as Λ in Figure 1.2. For example, the modulation wavelength of the superlattice in Figure 1.2 is equal to the bilayer thickness of the A and B alternating layers ($\Lambda = \lambda_A + \lambda_B$). Compared to multilayers, superlattices are not only modulated, but also crystallographically coherent. Thus, the lattice mismatch between the alternating layers in a superlattice is typically low. The crystallographic orientations of a superlattice are determined by the substrate, typically a single-crystalline substrate. Therefore, superlattices are usually epitaxial. In a superlattice, the thickness of each individual layer can be very small, e.g., on the nanometer scale, whereas the overall thickness of a superlattice can be on the micrometer scale, or even larger. Thus, superlattices have a unique advantage because they combine nanometer-scale dimensions of individual layer thickness with the utility of large scale films that can be conveniently connected in real devices.

Long-period superlattices were first discovered in 1936 by Johannson and Linde in the CuAu system.[62] Since then many other researchers have developed superlattices in different systems and they have studied the electronic and magnetic properties of

superlattices. Of all the accomplishments in this field, the most well-known one was made by the 2007 Nobel Laureates in Physics, Albert Fert and Peter Grünberg, who found that a series of Fe/Cr superlattices exhibited extremely large changes in electrical resistivity in response to relatively small changes in magnetic field.[63-69] This phenomenon, lately called "giant magnetoresistance" (GMR) by Fert, became a driving force of the revolution in the field of data transfer and storage in the electronics industry.[70]

Although most of the work in the fabrication of superlattices was done by chemical or physical vapor deposition processes in an ultra-high vacuum, electrodeposition is also an important technique for producing superlattices. The advantages of high vacuum techniques are that they can produce very pure materials on both conductive and non-conductive substrates. Although electrodeposition requires conductive substrates, it has several advantages compared to those high-vacuum vapor deposition processes:[60,71] *i*) the operating temperature is low, which minimizes the interdiffusion between the alternating layers of different compositions, *ii*) the stoichiometry or composition of the deposited materials can be controlled by the applied overpotential, *iii*) the individual layer thickness and the overall thickness of the superlattice can be easily controlled by the passed charge according to Faraday's law, and *iv*) the cost is low.[60]

Superlattices can be electrodeposited either from a single deposition bath or multiple deposition baths. For single-bath deposition, superlattices are electrodeposited by pulsing between different potentials or current densities. In this case, layers deposited at different potentials or current densities have different stoichiometries or compositions.

The crystal structures of these layers are similar. Thus, the lattice mismatch between these alternating layers is low. Besides, since the electrode is not exposed to atmosphere and there is almost no interval between the pulsed potentials (or current densities), the interfaces between the alternating layers can be sharp. Although putting all the precursors of the deposited materials in a single bath requires more effort in solution design, this method is ideal for depositing nanostructures with a nearly unlimited number of layers.[60] Multiple bath deposition method is usually used to produce superlattices composed of alternating layers of different materials. This method is much easier from the aspect of the design of the deposition baths, but it is not as simple as single-bath method during the deposition. The electrode needs to be alternated among different baths. Unlike the single-bath method, generally this method is only able to accomplish the deposition of superlattices with a limited number of alternating layers.[60]

Switzer's group pioneered the single-bath electrodeposition of metal oxide superlattices. Defect chemistry superlattices in the magnetite (Fe_3O_4) and thallium(III) oxide (Tl_2O_3) systems were electrodeposited.[42,72] Superlattices in the Fe_3O_4 system were electrodeposited from a solution containing 87 mM Fe(III), 100 mM triethanolamine (TEA), and 2 M NaOH at 80 ℃ by pulsing between -0.99 and -1.05 $V_{Ag/AgCl}$. The alternating layers in these superlattices have different Fe(II)/Fe(III) ratios. Superlattices in the Tl_2O_3 system were deposited from a solution of 100 mM $TlNO_3$ in 1 M NaOH by pulsing the overpotential between 90 and 300 mV. Results show that the high overpotential favors oxygen vacancies, whereas the low overpotential favors cation interstitials.[72,73] In addition to defect chemistry superlattices, compositional superlattices in the $ZnFe_2O_4/Fe_3O_4$ and Pb-Tl-O systems have also been electrodeposited.[42,46,74-76]

They were deposited by pulsing the potential or current density from a solution containing the precursors of both individual layers of the superlattices. Compositional superlattices are composed of alternating layers with different ion ratios, e.g., the alternating layers with different Fe/Zn ratios in $ZnFe_2O_4/Fe_3O_4$ superlattices.

Superlattices manifest their superperiodicity by showing satellite peaks around the main Bragg peak in XRD 2θ patterns. For example, Figure 1.3 shows the XRD 2θ scan around the (400) peak for a Pb-Tl-O superlattice.[46] It clearly shows seven orders of satellite peaks due to the superperiodicity. Based on the satellites

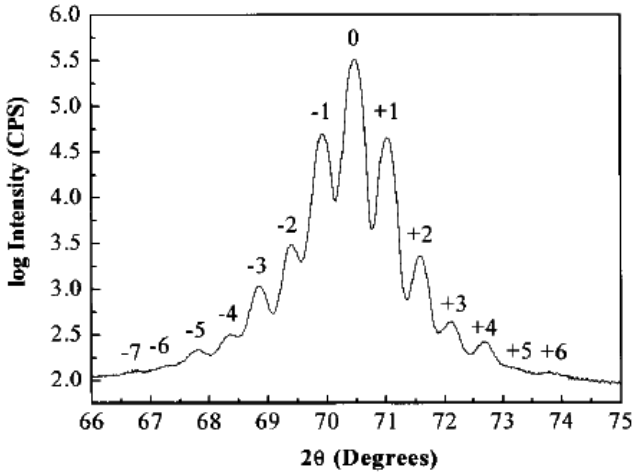

Figure 1.3. X-ray 2θ scan around the (400) reflection for a Pb-Tl-O superlattice showing seven orders of satellite peaks.[46]

in the XRD 2θ pattern, the modulation wavelength, Λ, of the superlattice can be calculated from the equation 4,[42,74] where λ is the wavelength of the X-ray source

$$\Lambda = \frac{\lambda(L_1 - L_2)}{2(\sin\theta_1 - \sin\theta_2)} \quad (4)$$

(Cu Kα = 0.1541 nm), L is the order of the satellite, and θ is the diffraction angle of satellite L.[74] Normally, the satellites in compositional superlattices are more intense than those in defect-chemistry superlattices, due to the larger Z-contrast in compositional superlattices.[42] The layered structure of a compositional superlattice with a large modulation wavelength can also be directly observed by electron microscopy. Figure 1.4 shows a high angle annular dark field (HAADF) image of a $ZnFe_2O_4/Fe_3O_4$ superlattice with a modulation wavelength of 70 nm.[42] The bright and dark bands represent the $ZnFe_2O_4$ and Fe_3O_4 layers, respectively.

In addition to the superlattices mentioned above a new compositional superlattice in the $CoFe_2O_4/Fe_3O_4$ systems has been developed. More details about this superlattice can be found in Paper II in this dissertation.

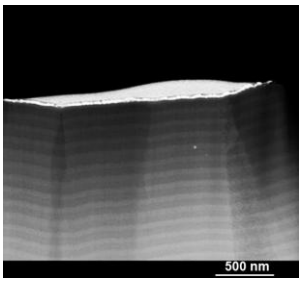

Figure 1.4. STEM-high angle annular dark field image of a zinc ferrite superlattice with a modulation wavelength of 70 nm.[42]

1.2. ELECTRODEPOSITED SPINTRONIC FILMS AND SUPERLATTICES

A recently developed technology, called spintronics (spin transport electronics or spin-based electronics), is a new concept for the design of electronics. Unlike traditional electronic devices, which use electrons or holes to carry information, spintronics use the up or down spin of the carriers to do so.[70,77] This opens up possibilities to build a new generation of devices which could have not only the properties of traditional electronics but also spin-dependent effects that arise from the interaction between the spin of the carriers and the magnetic properties of the material.[70]

The interest on spintronics started in 1988 when the giant magnetoresistive effect (GMR) was discovered in artificial thin-film materials composed of alternating ferromagnetic Fe(001) and nonmagnetic Cr(001) layers produced by molecular beam epitaxy (MBE).[63] This structure operates at room temperature and its resistivity is lowest as the magnetic moments in ferromagnetic layers are aligned or highest as they are anti-aligned when subjected to relatively small magnetic fields of 100 to 1000 Oe.[63] Based on the discovery of GMR, new structures for spin-dependent transport have been developed, of which spin valves and magnetic tunnel junctions (MTJs) are two of the most important types. A spin valve is generally a GMR-based device. It has two ferromagnetic layers separated by a thin nonmagnetic layer as shown in Figure 1.5.[70] In a spin valve, one of the two magnetic layer acts as a so-called “pinned” layer, of which the magnetization is relatively insensitive to moderate magnetic fields. An antiferromagnetic layer in intimate contact with the pinned magnetic layer (the first two layers on the top as shown in Figure 1.5) is usually used to accomplish the pinning.[78] The other magnetic layer is called the

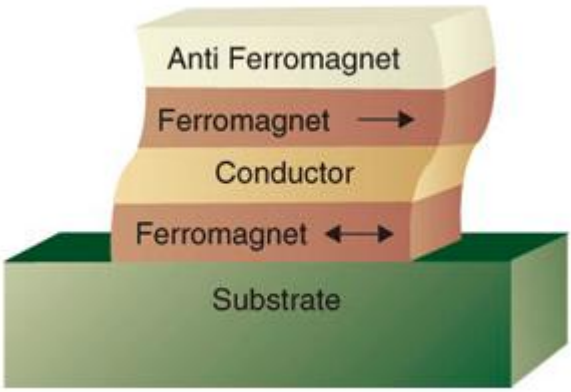

Figure 1.5. Schematic for a spin valve.[70]

"free" layer, and its magnetization can be switched by applying in-plane magnetic fields. The resistance of a spin valve can increase from 5 to 10% as the magnetizations in the two layers change from parallel to antiparallel alignment.[70] A magnetic tunnel junction (MTJ) is similar to a spin valve except for that it has a thin insulating layer instead of a nonmagnetic metal layer between the two ferromagnetic layers.[79,80] In a MTJ, when the magnetizations of the two ferromagnetic layers are aligned parallel by an applied magnetic field, electrons can tunnel across the thin insulating layer. MTJ devices usually have high resistances due to the low tunneling current density.[70]

Besides developing new structures, searching for materials which are suitable for spintronic applications is also critical. The ideal materials would combine properties of the ferromagnet and the semiconductor (ferromagnetic semiconductors (FS)), have Curie temperatures above room temperature, and be able to incorporate not only p-type dopants, but also n-type dopants.[70] However, so far no breakthrough has been made on FS for spintronics. A compromised approach is to search for materials that exhibit large carrier spin polarization, e.g., ferromagnetic oxides and related compounds. Switzer's

group has focused on the electrodeposition of metal oxide thin films and superlattices. Magnetic materials (such as Fe_3O_4 and $ZnFe_2O_4$) which can be potentially used in spintronics have been successfully deposited.[42] Fe_3O_4 is a ferrimagnetic material below its Curie temperature (about 860 K), whereas $ZnFe_2O_4$ is an antiferromagnetic material below its Neel temperature of about 10 K. They also showed that superlattices in the $Fe_3O_4/ZnFe_2O_4$ system could be electrodeposited. Electrodeposited thin films, especially the superlattices, of metal oxides could be suited for the application of spintronics.

1.2.1. Electrodeposited Fe_3O_4 Thin Films. Fe_3O_4 is a half-metallic oxide with an inverse spinel structure (space group *Fd3m*) and a lattice parameter of 8.396 Å.[42] In a unit cell of Fe_3O_4 the 8 tetrahedral sites are occupied by Fe^{3+} ions, whereas the 16 octahedral sites are equally shared by Fe^{3+} and Fe^{2+} ions. Fe_3O_4 is considered to be an attractive material for spintronics because its Curie temperature (about 860 K) is well above room temperature and it has a predicted -100% spin polarization at the Fermi level.[81,82] Switzer's group has shown that polycrystalline or epitaxial Fe_3O_4 thin films could be electrodeposited onto stainless steel, Au, and Ni substrates from an alkaline or acidic solution.[17-21,42] They also showed that defect chemistry superlattices in the Fe_3O_4 system can be electrodeposited by pulsing between two deposition potentials. An electrodeposited superlattice composed of alternating layers of materials with different magnetic properties could be promising candidate for spintronic applications.

1.2.2. Electrodeposited Cation-Substituted Fe_3O_4. By substituting Fe ions in Fe_3O_4 with other 3d transition metal ions, cation-substituted Fe_3O_4 can be obtained, e.g., cobalt ferrite ($CoFe_2O_4$),[83-87] zinc ferrite ($ZnFe_2O_4$),[42,87-89] nickel ferrite ($NiFe_2O_4$),[84,87,90] and manganese ferrite ($MnFe_2O_4$)[91,92]. The substitution does not need to be

stoichiometric, partial substitution will result in a nonstoichiometric ferrite, $M_xFe_{3-x}O_4$ ($0<x<1$; where M represents a metal other than Fe). The crystal structures of these cation-substituted Fe_3O_4 are similar to Fe_3O_4. However, the electric and magnetic properties of them could be quite different depending on the ions substituting into Fe_3O_4. For example, Fe_3O_4 is a conductor whereas other ferrites are insulators at room temperature. Fe_3O_4 is a soft magnetic material, whereas $CoFe_2O_4$ is a hard magnetic material. Thus, thin films of these ferrites can play different roles in spintronic devices depending on their electric and magnetic properties. For example, in a spin valve, Fe_3O_4 can act as a "free" layer in which the magnetization can be switched by applying a moderate magnetic field, whereas $CoFe_2O_4$ can act as a "pinned" layer in which the magnetization is not sensitive to the applied magnetic field. Besides, electrodeposited layered structures (such as superlattices) composed of epitaxial films of different ferrites could be well suited for spintronic devices.

Switzer's group has shown that zinc ferrite thin films and superlattices could be electrodeposited.[42] They suggested that the deposition followed an electrochemical-chemical mechanism (EC).[42] This mechanism should be quite general for depositing other cation-substituted ferrites as long as the stable precursor electrolytes containing both Fe ions and the other metal ions can be prepared. Paper II in this dissertation is focused on the electrodeposition of Co-substituted Fe_3O_4 ($Co_xFe_{3-x}O_4$) thin films and superlattices. More details about how the films were electrodeposited and how the electric and magnetic properties change with Co content in the films can be found there. The property differences between the individual films and superlattices are also discussed in that paper.

1.3. ELECTROCHEMICAL REDUCTION OF METAL OXIDES TO METALS

The electrochemical reduction of metal oxides (or metal hydroxides) to the corresponding metals has been studied for several decades as an alternative to pyrometallurgical processes for the metallurgy industry. This method is attractive because of several of its advantages. First of all, it is simple. Metals can be produced directly from the corresponding metal oxides (sometimes even directly from the ores) without complicated procedures. Secondly, it is inexpensive. The main equipment needed for this method are potentiostats/galvanostats, high-temperature containers (optional), and electrodes. Moreover, this method is environmentally friendly. Unlike the traditional pyrometallurgical processes which release tons of CO_2 (a major component of "greenhouse" gases) into the atmosphere every year, there are no harmful by-products being produced during the electrochemical reduction of metal oxides. Although most of the work on this topic has been focused on producing iron from its oxides/hydroxides, this method is applicable to produce other metals from their metal oxides/hydroxides. Examples include the electrochemical reduction of TiO_2 to Ti, CuO to Cu, SiO_2 to Si, and ZrO_2 to Zr.[93-97] Of these examples, Ti and Si are extremely difficult to prepare in pure form using state-of-art techniques without complicated and expensive procedures. So, developments of electrochemical reduction techniques for producing metals like Ti and Si are highly desired. Except for pure metals, metal alloys can also be produced by electrochemical reduction of the mixed powders of different metal oxides.[94,98-100] Electrochemical reduction of different metal hydroxides/oxides requires the use of different media (electrolytes) and experimental parameters, which will be addressed in the following sections.

1.3.1. Electrochemical Reduction of Iron Hydroxide/Oxide to Iron.

The electrochemcial reduction of iron hydroxide/oxide to iron is the most studied system in this field because of the large consumption of iron (steel) all over the world. Currently, the production of iron is based on pyrometallurgical processes which have added a significant amount of greenhouse gases into the earth's atmosphere. Therefore, developing breakthrough technologies to reduce the greenhouse gas emissions in the production of steel is important. Electrochemical reduction of iron oxides/hydroxides to iron is one of the possible techniques.[101] This has been studied for almost a century. In 1918, Estelle patented a process for electrolytically producing iron from a solution consisting of 30% iron(III) hydroxide, 35% sodium hydroxide, and 35% water at 100 ℃.[102] Based on Estelle's work, Angel found out that finely divided iron ore (α-Fe_2O_3) could also be used as an iron source in the same strong caustic soda solution to produce iron powder.[103] More recently, Allanore and co-workers electrochemically reduced porous iron ore (α-Fe_2O_3, hematite) particles to iron in 10 M KOH solution at 100 ℃.[104] An illustration of the setup that Allanore et al. used for the experiment is shown in Figure 1.6. For the electrochemical reduction of α-Fe_2O_3 to Fe, a dissolution/redeposition mechanism with magnetite (Fe_3O_4) as the intermediate was proposed.[101,104] The presence of the electronically conductive magnetite in the immediate vicinity of the iron metal has important consequences on the current efficiency of the reaction.[101]

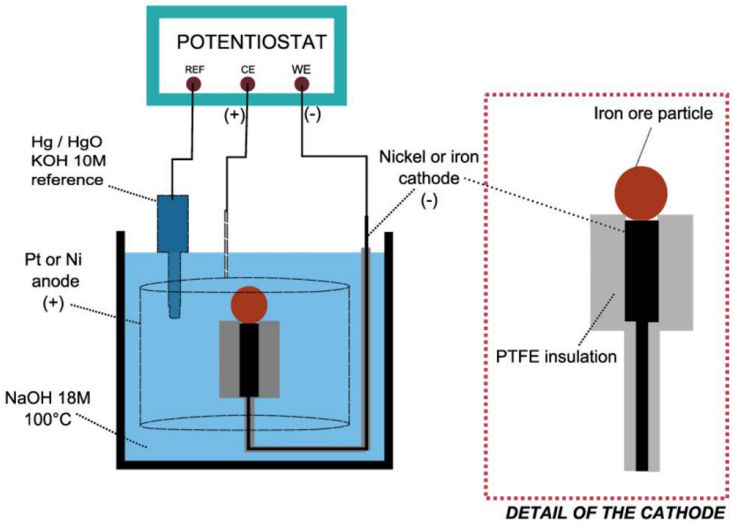

Figure 1.6. Electrochemical setup for static reduction of hematite particles.[104]

1.3.2. Producing Ti and Si by Electrochemical Reduction of TiO_2 and SiO_2.

Ti and Si are two important industrial materials because of many of the desirable properties they have. Ti is light, strong, and corrosion-resistant. Ti and its alloys are popular materials used in aircraft, spacecraft, and automotive applications.[105] They are also used in medical applications such as artificial limbs and implants, due to good biocompatibility. Silicon is a major material used in the fabrication of solar cells, silicon chips, optical fibers, and silicones.[94,106] However, these two metals are difficult to prepare in pure form. Current techniques for producing Ti and Si from their compounds are complicated and expensive.

Ti is produced by a pyrometallurgical process, called the Kroll process.[107] In this process, the titanium minerals, rutile and ilmenite, are carbochlorinated to remove oxygen, iron and other impurities, producing $TiCl_4$ vapor. This is then reduced to titanium metal by magnesium metal; the by-product, $MgCl_2$, is removed by vacuum

distillation.[107,108] The attempts to directly electrodeposit Ti from ionic solutions are also difficult because of the redox cycling of multivalent titanium ions and reactive dendritic products.[105,108]

Presently, the industrial production of Si is mainly from the carbothermal reduction of SiO_2, in which the oxygen is removed by a heterogeneous-homogeneous reaction sequence at approximately 1700 ℃, producing CO_2 as a by-product.[93,94] This process is time consuming and expensive, and it consumes charcoal and water. It also produces a huge amount of CO_2, which is one of the major greenhouse gases. In 2002, the production of Si all over the world was about 4.1×10^6 tons, resulting in the emission of about 6.5×10^6 tons of CO_2 into the atmosphere.[94]

In order to reduce the production cost and the greenhouse gas emissions, the electrochemical reduction method, as an alternative to the conventional techniques, has been developed to produce Ti and Si. Ti has been produced by the direct electrochemical reduction of solid TiO_2 in molten $CaCl_2$ at 950 ℃.[108] This method is called the FFC Cambridge process and was developed by Chen and co-workers.[108-111] In this method, the oxygen in TiO_2 is ionized at the cathode, dissolved in the molten salt and discharged at the anode. The cathodic reaction can be expressed by the following equation.[108] Two

$$TiO_x + 2xe^- \leftrightarrow Ti + xO^{2-} \qquad (5)$$

electrolytic cells for the electrochemical reduction of TiO_2 to Ti are shown in Figure 1.7.[108] These two cells operate in the same fashion except for that in the left cell the wall of the crucible itself acts as a cathode whereas in the right cell the Kanthal wire acts as a

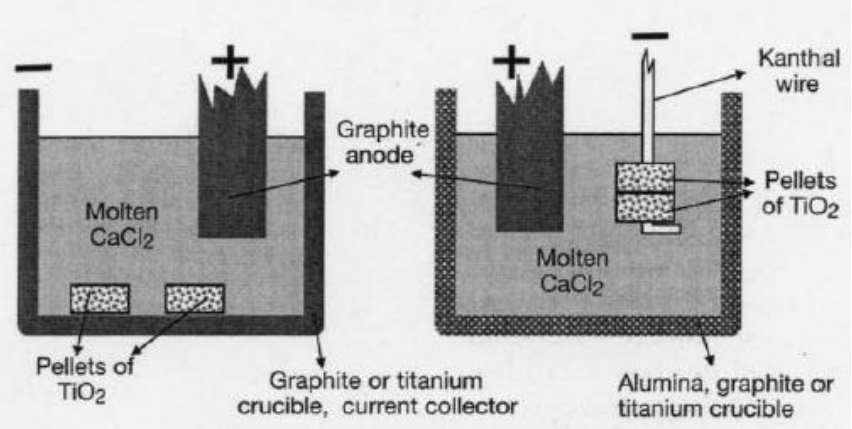

Figure 1.7. Electrolytic cells for the reduction of TiO_2 pellets.[108]

cathode. For reducing TiO_2 pellets, a voltage of 3.0 to 3.2 V is simply applied between a graphite rod anode and the wall of the crucible (left cell) or the Kanthal wire (right cell) for several hours depending on the quantity and size of the TiO_2 pellets (prepared from TiO_2 powders by pressing or slip-casting). After reduction, examination under SEM (Figure 1.8) shows that the 0.25 μm oxide powder has been transformed into Ti metal particles of about 12 μm which are slightly sintered together, similar to the Kroll titanium sponge.[108]

Reduction of SiO_2 to Si is very similar to that of TiO_2 to Ti. The oxygen in SiO_2 is removed from the solid SiO_2 by constant potential electrolysis in a molten salt. Nohira and co-workers showed the pinpoint and bulk reduction of a SiO_2 electrode (quartz plate) to Si.[93] Jin and co-workers demonstrated that porous pellets made from SiO_2 powders can be electrochemically reduced to Si powders. They also showed that silicon alloy powders can be produced by electrochemically reducing SiO_2 powders mixed with other metal oxide powders.[94]

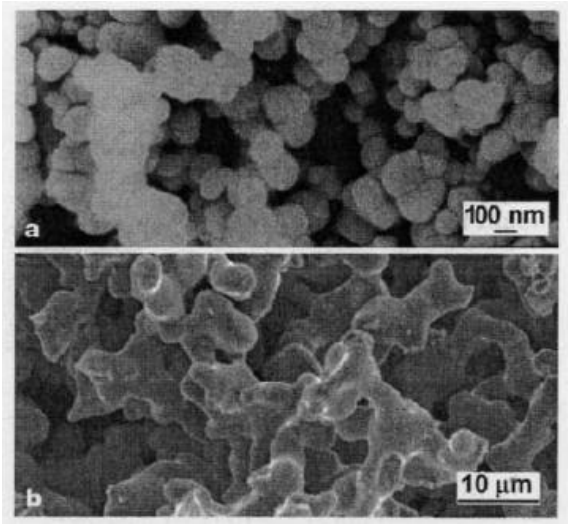

Figure 1.8. SEM images of the reduction of (a) the TiO_2 powder to (b) titanium metal.[108]

1.3.3. Electrochemical Reduction of Epitaxial Metal Oxide Films to Epitaxial Metal Films. In Switzer's group, an attempt has been made to extend the ability of controlling the in-plane and out-of-plane orientations of a thin film during electrodepositon into the process of the electrochemical reduction of metal oxides to metals has been made. In addition, more details about the electrochemical reduction process, rather than just producing metals, have been studied. Initially, it was found that an epitaxial magnetite (Fe_3O_4) thin film on a Au(111) single crystal was reduced to a shiny metallic Fe layer in 2 M NaOH solution at 80 ℃ after scanning the potential to -1.35 V vs. Ag/AgCl. This interesting observation lead to the following three questions. Was the Fe film reduced from the epitaxial Fe_3O_4 film still epitaxial? Was the orientation of the Fe film after reduction controlled by the Au single-crystalline substrate or the precursor epitaxial Fe_3O_4 film? Furthermore, could the reduction of Fe_3O_4 could happen at a lower temperature, even room-temperature?

Previous work on the electrochemical reduction of metal oxides to metals was designed to achieve large-scale and high-rate metal production as well as low CO_2 emission, and was conducted on bulk polycrystalline metal oxides. Although single-crystal Bi_2S_3 and BiOCl were reported to be electrochemically reduced to Bi metal via an electron/proton transfer reaction at ambient temperature, there was no correlation between the initial orientation of the oxide crystals and the orientation of the metal crystallites after reduction.[112,113] The possibility of transforming an epitaxial Fe_3O_4 film to an epitaxial Fe film by electrochemical reduction was studied in this dissertation research. This research could provide a new route to produce high-quality epitaxial metal and metal alloy films. Details on the electrochemical reduction of epitaxial magnetite films to epitaxial iron films will be presented in Paper I in this dissertation.

1.4. PHOTOELECTROCHEMICAL WATER SPLITTING

Considering the energy and environmental concerns due to the limited quantity of fossil-based energy and the emission of greenhouse gases from these fuels, searching for clean and renewable energy resources has attracted much attention. Solar energy is one of the most important renewable energy resources because it is decentralized, inexhaustible, and incredibly massive.[114] The magnitude of the incoming solar energy reaching the earth's surface in 1 hour is more than all of the energy consumed by humans in an entire year.[115] Thus, developing efficient ways to collect, convert, and store solar energy is a critical topic. Currently, two ways to utilize solar energy are intensively studied. One is through photovoltaics and another is through photoelectrochemical solar cells.

Photovoltaic devices are attractive because they can directly convert solar energy into electricity, which is the simplest way to utilize our biggest and most sustainable energy reservoir.[116,117] However, the contribution of the solar electricity generated from photovoltaics to the overall world energy consumption is still small, mainly due to the high cost and low efficiency of the photovoltaic devices.[118] The theoretical efficiency limit for a single-band gap solar conversion device is only 31%, and currently shipped photovoltaic modules have even lower efficiencies of about 15-20%. The calculated sale price of grid-connected photovoltaic electricity is higher than $0.25 to $0.30 per kilowatt-hour (kWh), which is much higher than current price of the electricity from power plants.[115] Therefore, attempts to lower the cost and enhance the efficiency of the photovoltaic devices are key points in this field.

The photoelectrochemical solar cell is another way to utilize solar energy. It is designed to collect, convert and store solar energy into chemical bonds, as accomplished through the photosynthesis process in nature. In other words, a photoelectrochemical solar cell should be able to roughly imitate what nature does with green plants and photosynthetic bacteria, using sunlight to drive a thermodynamically uphill reaction of abundant materials to produce fuels.[119] As early as about 3 billion years ago, photosynthetic eukaryotes showed photosynthetic properties from endosymbiosis with cyanobacteria.[120,121] However, not until recent decades has mankind been trying to learn this from nature to develop alternative energy resources to replace nonrenewable and polluting fossil fuels. The development of the photoelectrochemical solar cell also encounters the same drawbacks (i.e., low efficiency and high cost) as the photovoltaic cell does. However, it has an advantage compared to photovoltaics. Unlike the

photovoltaic cell, which can produce electricity only when there is sunlight, the photoelectrochemical solar cell can convert solar energy to storable fuels that can be used anytime (e.g., at night). Therefore, the photoelectrochemical solar cell and photovoltaics can be complementary to each other. In the daytime, the photovoltaics can produce electricity and provide power to operate the electrochemical solar cell (if necessary), and at night the stored fuels produced by the photoelectrochemical solar cell in the daytime can be used to continuously provide power.

Generally, three requirements need to be fulfilled for any system built on the purpose of collecting, converting and storing solar energy.[122] Firstly, sunlight should be absorbed efficiently to produce excited electron states in the light-absorbing material (usually a semiconductor). To satisfy the first requirement, the semiconductor should have proper band gap in order to efficiently absorb a wide range of the spectrum of the sunlight that reaches the earth's surface. Photons having energy lower than the band gap of the material will not be absorbed, whereas photons having energy higher than the band gap of the material will be absorbed and the excess energy of the photons will be converted to heat.[114,115] Secondly, the photoinduced free charge carriers (electrons and its accompanying electron vacancies (holes)) in the semiconductor must be separated in space to prevent the recombination. The electrons/holes must travel to the semiconductor/liquid junction to react with solution species in order to convert and store solar energy into fuels produced by the oxidation/reduction reactions at the surface of the semiconductor.[114] Thirdly, the photoexcited charge should be energetically and kinetically able to drive a chemical reaction at the semiconductor surface, which converts solution species into a fuel, e.g., splitting water to produce H_2.[123]

Solar water splitting is an attractive path to harvest sunlight into a storable and clean fuel. Water and sunlight are cheap, clean and renewable resources. The fuel generated by solar water splitting, hydrogen (H_2), is a clean-burning fuel that only produces water as the waste product.[114,123,124] Fujishima and Honda introduced the concept of sunlight-assisted water splitting to the public by their paper about water oxidation at the surface of crystalline TiO_2 photoelectrodes under UV light irradiation.[125] This concept was then used by Bard to design a photocatalytic system.[126,127] A cartoon illustrating the similarities and differences among photosynthesis, solar water splitting, and photovoltaics is shown in Figure 1.9. For photosynthesis (left in Figure 1.9), plants

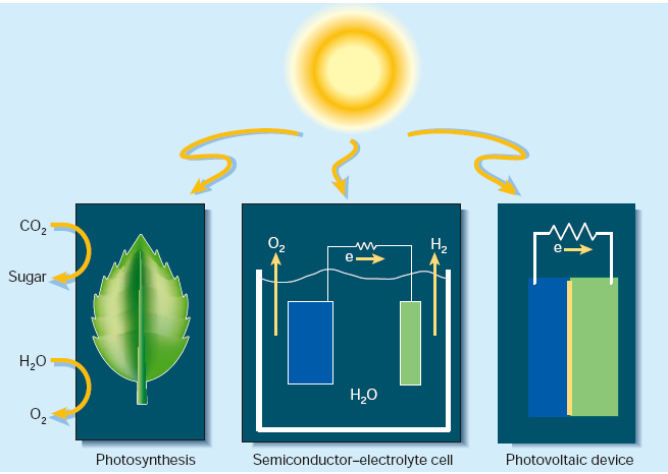

Figure 1.9. Energy-conversion strategies for creating fuel or electricity from sunlight.[123]

use sunlight to convert CO_2 and H_2O to sugars (fuel) and O_2. For solar water splitting (center of Figure 1.9), a photoelectrochemical cell uses sunlight to split water into H_2 (at

the cathode) and O_2 (at the anode). For photovoltaics (right of Figure 1.9), sunlight is converted directly into electricity using a p-n junction of semiconductors.

Water splitting into H_2 and O_2 is an uphill reaction with the standard Gibbs free energy change (ΔG^0) of 237 kJ/mol or 1.23 eV. Thus, theoretically, to accomplish solar water splitting without any other assistance, the used photoelectrode material should be able to absorb the radiant light with photon energies larger than 1.23 eV (1000 nm and shorter).[128] At the same time, the band gap energy (E_g) of the semiconductor needs to be smaller than 3.0 eV (400 nm) in order to absorb visible light, which is the largest portion of the solar spectrum on the earth's surface. Moreover, the electrochemical potentials E^o (H^+/H_2) and E^o (O_2/H_2O) should fall in between the conduction band-edge energy (E_{cb}) and valence band-edge energy (E_{vb}) as shown in Figure 1.10.[114,129] Therefore,

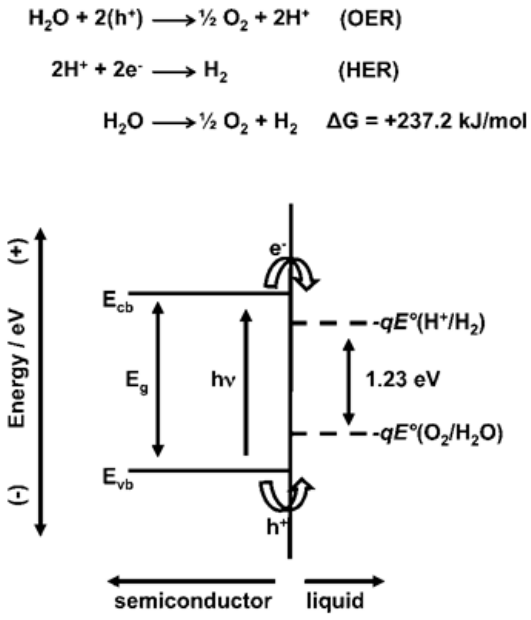

Figure 1.10. An illustration showing the energy band positions of a semiconductor material for water splitting (under acidic conditions).[114]

semiconductors with specific band gaps are commonly used as light absorbers and they can satisfy the first and second requirements (as mentioned previously) for solar water splitting cell because they generally have broad and strong optical absorption characteristics and the electric fields at the semiconductor/electrolyte interface facilitate effective charge separation.[123] However, the third requirement is the toughest one. In this case, if the photoexcited electrons are not energetically and kinetically able to split water spontaneously, a small external bias is usually applied to drive the reaction to occur. Although many materials have been tested as photoelectrodes, the ideal material has still not been found. On one hand, some semiconductors can absorb sunlight effectively, but they cannot sustain photoinduced water splitting. On the other hand, some materials that are good catalysts for water splitting and stable in solution, but they do not absorb sunlight effectively.[123] Therefore, lack of stable and high-efficient photoelectrode materials becomes the bottleneck of solar water splitting. Besides using a single semiconductor as the photoelectrode, functionalizing the surface of a semiconductor with a thin layer of H_2 or O_2 evolving catalysts has been considered to be a promising technique to improve the performance of the semiconductor photoelectrodes for solar water splitting.

1.4.1. Photocathode Materials for Solar Water Splitting. The ideal materials for photocathodes should be able to supply sufficient cathodic current for water splitting and stable in aqueous solution.[128] In addition, the potential of the conduction band edge of the photocathode must be more negative than the hydrogen redox potential. If it is more positive than the hydrogen redox potential, an external bias will be needed to split water. There are two different mechanisms to evolve H_2 depending on the pH of the

electrolyte. As shown by the following equations, if the electrolyte is acidic, the hydrogen evolution reaction (HER) will proceed mainly by the reduction of protons. If the electrolyte has a high pH, the H_2 will be produced by reducing H_2O. The photoexcited

$$2H^+ + 2e^- \rightarrow H_2 \quad (6)$$

$$2H_2O + 2e^- \rightarrow H_2 + 2OH^- \quad (7)$$

electrons in the photocathode are driven toward the semiconductor/electrolyte interface to reduce H_2O or H^+ to H_2, while the holes are swept into the bulk of the photocathode. Many materials as pure, modified or composite forms have been tested as photocathode materials, such as p-GaP,[130] InP with Ru catalyst islands on the surface,[131] Cu_2O (protected by an ultrathin Al/Zn/Ti layer),[132] Cu-Ti-O nanotube arrays,[133] $CuGaSe_2$,[134] and F-doped Co_3O_4.[135]

1.4.2. Photoanode Materials for Solar Water Splitting. The materials used as oxygen evolving photoanodes are usually n-type semiconductors so that the photogenerated holes can be driven toward the surface by the electric field which arises from the band bending.[114] Besides a proper band gap and band edge positions, the semiconductor needs to be stable under light-induced water oxidation conditions and should be inexpensive.

Many efforts have been put into developing low-cost and efficient photoanode materials for photoelectrochemical oxidation of water. Besides TiO_2, which has been extensively studied following the initial work of Fujishima and Honda,[125] other metal oxides such as $SrTiO_3$ and $KTaO_3$ have also been tested.[136-138] Such metal oxides with

wide band gap (greater than 3 eV) can drive the unassisted photoelectrolysis of water under solar illumination. However, since they can only absorb a small portion of the solar spectrum because of their large band gap, their solar-to-chemical conversion efficiencies are less than 1%.[138-140] The theoretical limitation on the attainable solar conversion efficiency for the single-band gap semiconductor cells that drive the unassisted photoelectrolysis of water is typically about 2%.[114] Materials with moderate band gaps, such as Fe_2O_3 (~2.3 eV) and WO_3 (~ 2.7 eV), which can enhance the absorption of the solar spectrum, have also been considered as photoanode materials.[114,141-143] However, these materials usually have low saturation current densities at relatively high bias due to their modest electronic conductivities and moderate band gaps.[141,144] Small band gap materials, such as Si (bandgap 1.1eV), are capable of absorbing a large portion of the solar spectrum. However, most of them suffer so-called "photocorrosion" at the highly oxidative potential required for water oxidation, and thus cannot be used alone as photoanodes.[114,145]

Another approach of making an efficient and stable photoanode is to cover Si with a thin layer (or layers) of material(s) which can protect Si from being oxidized under the water oxidation conditions. The protecting layer should be a good oxygen evolving catalyst. If not, a layer of oxygen evolving catalyst needs to be put on top of the protecting layer in order to facilitate the oxygen evolution reaction as well as enhance the efficiency of the solar water splitting cell. The protecting layer(s) and the catalyst layer(s) need to fulfill several requirements, *i*) they should be corrosion-resistant under the solar water oxidation conditions for a considerably long time; *ii*) they should not inhibit the light absorption by Si; *iii*) they should be conductive in order to have a higher

efficiency.[145] Chen et al.[145] demonstrated that atomic layer-deposited (ALD) TiO_2 (2 nm) can stabilize the silicon photoanode and a thin Ir layer (3 nm) can be used as an oxygen evolving catalyst. The TiO_2 layer is thin enough to allow the electrons to tunnel through to fill the photogenerated holes in the Si substrate. By using this functionalized Si photoanode, the potential required to obtain a current density of 1 mA/cm^2 shifts about 200 mV lower than the thermodynamic water oxidation potential. Besides precious metals, such as Ir and Ru, oxygen evolving catalysts composed of earth abundant elements have also received much attention. An amorphous Co-phosphate catalyst (Co-Pi) developed by Nocera and co-workers have been shown to exhibit good catalytic activity towards oxygen evolution reaction at neutral pH.[146-150] It can also be attached to semiconducting metal oxides (e.g., Fe_2O_3,[142,151] WO_3 thin films,[152] and ZnO rods[153]) to enhance the efficiency of photoelectrochemical water splitting.[149] Nocera et al. have found the actual active species in Co-Pi is the Co(IV) compound produced during the water oxidation process.[154,155]

In Paper III in this dissertation, a method of the electrodeposition of crystalline Co_3O_4 films on stainless steel substrates is presented. Previous attempts to deposit Co_3O_4 films by other groups have led to the formation of amorphous and/or hydrated layers before annealing. Here, for the first time, the electrodeposition of crystalline Co_3O_4 films without any heat treatment is achieved. The crystalline Co_3O_4 films have higher catalytic activity towards the oxygen evolution reaction than Nocera's Co-Pi catalyst.[146] The next step will be to deposit a crystalline Co_3O_4 film onto a good light absorber, such as Si (or Si with a protecting layer), in an attempt to make an efficient and stable photoanode. It is also shown using a Au(111) single crystal as the substrate, that an epitaxial Co_3O_4 film

can be electrodeposited. This opens up the possibility to study the catalytic activity towards oxygen evolution reaction of different Co_3O_4 crystal planes exposed to the electrolyte. Different Co_3O_4 crystal planes have been shown to possess different catalytic activities towards reactions such as the oxidation of CO to CO_2 and methane combustion.[156,157]

REFERENCES

(1) Switzer, J. A.; Hodes, G. *MRS Bull.* **2010**, *35*, 743.

(2) Siegfried, M. J.; Choi, K.-S. *Adv. Mater.* **2004**, *16*, 1743.

(3) Siegfried, M. J.; Choi, K.-S. *Angew. Chem. Int. Ed.* **2005**, *44*, 3218.

(4) Switzer, J. A.; Kothari, H, M.; Poizot, P.; Nakanishi, S.; Bohannan, E. W. *Nature* **2003**, *425*, 490.

(5) Bohannan, E. W.; Kothari, H. M.; Nicic, I. M.; Switzer, J. A. *J. Am. Chem. Soc.* **2004**, *126*, 488.

(6) Switzer, J. A.; Kothari, H. M.; Bohannan, E. W. *J. Phys. Chem. B* **2002**, *106*, 4027.

(7) Gundel, A.; Devolder, T.; Chappert, C.; Schmidt, J. E.; Cortes, R.; Allongue, P. *Physica B* **2004**, *354*, 282.

(8) Damian, A.; Maroun, F.; Allongue, P. *Phys. Rev. Lett.* **2009**, *102*, 196101.

(9) Lay, M. D.; Stickney, J. L. *J. Am. Chem. Soc.* **2003**, *125*, 1352.

(10) Nakanishi, S.; Sakai, S.; Nagai, T.; Nakato, Y. *J. Phys. Chem. B* **2005**, *109*, 1750.

(11) Switzer, J. A. *J. Electrochem. Soc.* **1986**, *133*, 722.

(12) Liu, R.; Vertegel, A. A.; Bohannan, E. W.; Sorenson, T. A.; Switzer, J. A. *Chem. Mater.* **2001**, *13*, 508.

(13) Liu, R.; Bohannan, E. W.; Switzer, J. A.; Oba, F.; Ernst, F. *Appl. Phys. Lett.* **2003**, *83*, 1944.

(14) Allongue, P.; Maroun, F.; Jurca, H. F.; Tournerie, N.; Savidand, G.; Cortes, R. *Surf. Sci.* **2009**, *603*, 1831.

(15) Goux, A.; Pauporte, T.; Yoshida, T.; Lincot, D. *Langmuir* **2006**, *22*, 10545.

(16) Takei, T.; Dong, Q.; Yonesaki, Y.; Kumada, N.; Kinomura, N. *Langmuir* **2011**, *27*, 126.

(17) Nikiforov, M. P.; Vertegel, A. A.; Shumsky, M. G.; Switzer, J. A. *Adv. Mater.* **2000**, *12*, 1351.

(18) Sorenson, T. A.; Morton, S. A.; Waddill, G. D.; Switzer, J. A. *J. Am. Chem. Soc.* **2002**, *124*, 7604.

(19) Kothari, H. M.; Kulp, E. A.; Limmer, S. J.; Poizot, P.; Bohannan, E. W.; Switzer, J. A. *J. Mater. Res.* **2006**, *21*, 293.

(20) Kulp, E. A.; Kothari, H. M.; Limmer, S. J.; Yang, J.; Gudavarthy, R. V.; Bohannan, E. W.; Switzer, J. A. *Chem. Mater.* **2009**, *21*, 5022.

(21) Gudavarthy, R. V.; Gorantla, S.; Mu, G.; Kulp, E. A.; Gemming, T.; Eckert, J.; Switzer, J. A. *Chem. Mater.* **2011**, *23*, 2017.

(22) Gudavarthy, R. V.; Miller, A. S.; Bohannan, E. W.; Kulp, E. A.; He, Z.; Switzer, J. A. *Electrochimi. Acta* **2011**, *56*, 10550.

(23) Switzer, J. A.; Shumsky, M. G.; Bohannan, E. W. *Science* **1999**, *284*, 293.

(24) Bohannan, E. W.; Jaynes, C. C.; Shumsky, M. G.; Barton, J. K.; Switzer, J. A. *Solid State Ionics* **2000**, *131*, 97.

(25) Sarkar, S. K.; Burla, N.; Bohannan, E. W.; Switzer, J. A. *J. Am. Chem. Soc.* **2007**, *129*, 8972.

(26) Poizot, P.; Hung, C.-J.; Nikiforov, M. P.; Bohannan, E. W.; Switzer, J. A. *Electrochem. Solid-State Lett.* **2003**, *6*, C21.

(27) Kothari, H. M.; Kulp, E. A.; Boonsalee, S.; Nikiforov, M. P.; Bohannan, E. W.; Poizot, P.; Nakanishi, S.; Switzer, J. A. *Chem. Mater.* **2004**, *16*, 4232.

(28) Bohannan, E. W.; Nicic, I. M.; Kothari, H. M.; Switzer, J. A. *Electrochimi. Acta* **2007**, *53*, 155.

(29) Gudavarthy, R. V.; Burla, N.; Kulp, E. A.; Limmer, S. J.; Sinn, E.; Switzer, J. A. *J. Mater. Chem.* **2011**, *21*, 6209.

(30) Golden, T. D.; Shumsky, M. G.; Zhou, Y.; VanderWerf, R. A.; Van Leeuwen, R. A.; Switzer, J. A. *Chem. Mater.* **1996**, *8*, 2499.

(31) Barton, J. K.; Vertegel, A. A.; Bohannan, E. W.; Switzer, J. A. *Chem. Mater.* **2001**, *13*, 952.

(32) Switzer, J. A.; Liu, R.; Bohannan, E. W.; Ernst, F. *J. Phys. Chem. B* **2002**, *106*, 12369.

(33) Liu, R.; Oba, F.; Bohannan, E. W.; Ernst, F.; Switzer, J. A. *Chem. Mater.* **2003**, *15*, 4882.

(34) Liu, R.; Kulp, E. A.; Oba, F.; Bohannan, E. W.; Ernst, F.; Switzer, J. A. *Chem. Mater.* **2005**, *17*, 725.

(35) Oba, F.; Ernst, F.; Yu, Y.; Liu, R.; Kothari, H. M.; Switzer, J. A. *J. Am. Ceram. Soc.* **2005**, *88*, 253.

(36) Limmer, S. J.; Kulp, E. A.; Switzer, J. A. *Langmuir* **2006**, *22*, 10535.

(37) Mu, G.; Gudavarthy, R. V.; Kulp, E. A.; Switzer, J. A. *Chem. Mater.* **2009**, *21*, 3960.

(38) Vertegel, A. A.; Bohannan, E. W.; Shumsky, M. G.; Switzer, J. A. *J. Electrochem. Soc.* **2001**, *148*, C253.

(39) Kulp, E. A.; Switzer, J. A. *J. Am. Chem. Soc.* **2007**, *129*, 15120.

(40) Vertegel, A. A.; Shumsky, M. G.; Switzer, J. A. *Angew. Chem. Int. Ed.* **1999**, *38*, 3169.

(41) Boonsalee, S.; Gudavarthy, R. V.; Bohannan, E. W.; Switzer, J. A. *Chem. Mater.* **2008**, *20*, 5737.

(42) Switzer, J. A.; Gudavarthy, R. V.; Kulp, E. A.; Mu, G.; He, Z.; Wessel, A. J. *J. Am. Chem. Soc.* **2010**, *132*, 1258.

(43) Bard, A. J.; Faulkner, L. R. "*Electrochemical Methods: Fundamentals and Applications"*, 1980.

(44) Goux, A.; Pauporte, T.; Chivot, J.; Lincot, D. *Electrochimi. Acta* **2005**, *50*, 2239.

(45) Hubert, C.; Naghavi, N.; Canava, B.; Etcheberry, A.; Lincot, D. *Thin Solid Films* **2007**, *515*, 6032.

(46) Kothari, H. M.; Vertegel, A. A.; Bohannan, E. W.; Switzer, J. A. *Chem. Mater.* **2002**, *14*, 2750.

(47) Kawae, T.; Hu, J.; Naganuma, H.; Nakajima, T.; Terauchi, Y.; Okamura, S.; Morimoto, A. *Thin Solid Films* **2011**, *519*, 7727.

(48) Chambers, S. A. *Adv. Mater.* **2010**, *22*, 219.

(49) Guo, H.; Burgess, J.; Street, S.; Gupta, A.; Calvarese, T. G.; Subramanian, M. A. *Appl. Phys. Lett.* **2006**, *89*, 022509/1.

(50) Tsubouchi, K.; Ohkubo, I.; Kumigashira, H.; Matsumoto, Y.; Ohnishi, T.; Lippmaa, M.; Koinuma, H.; Oshima, M. *Appl. Phys. Lett.* **2008**, *92*, 262109/1.

(51) Reiner, J. W.; Kolpak, A. M.; Segal, Y.; Garrity, K. F.; Ismail-Beigi, S.; Ahn, C. H.; Walker, F. J. *Adv. Mater.* **2010**, *22*, 2919.

(52) Opel, M. *J. Phys. D* **2012**, *45*, 033001/1.

(53) Capan, C.; Sun, G. Y.; Bowden, M. E.; Chambers, S. A. *Appl. Phys. Lett.* **2012**, *100*, 052106/1.

(54) Bahlawane, N.; Kohse-Hoeinghaus, K.; Weimann, T.; Hinze, P.; Roehe, S.; Baeumer, M. *Angew. Chem. Int. Ed.* **2011**, *50*, 9957.

(55) Suh, S.; Hoffman, D. M.; Atagi, L. M.; Smith, D. C.; Liu, J.-R.; Chu, W.-K. *Chem. Mater.* **1997**, *9*, 730.

(56) Yamaguchi, T.; Aoki, S.; Sadakata, N.; Kohno, O.; Osanai, H. *Appl. Phys. Lett.* **1989**, *55*, 1581.

(57) Chong, Y. T.; Yau, E. M. Y.; Nielsch, K.; Bachmann, J. *Chem. Mater.* **2010**, *22*, 6506.

(58) Rauwel, E.; Clavel, G.; Willinger, M.-G.; Rauwel, P.; Pinna, N. *Angew. Chem. Int. Ed.* **2008**, *47*, 3592.

(59) Hamalainen, J.; Munnik, F.; Ritala, M.; Leskela, M. *Chem. Mater.* **2008**, *20*, 6840.

(60) Switzer, J. A. "*Electrochemistry of Nanomaterials"* **2001**, 67.

(61) Schuller, I. K. *Phys. Rev. Lett.* **1980**, *44*, 1597.

(62) Jones, H. *J. Phys. C.* **1969**, *2*, 733.

(63) Baibich, M. N.; Broto, J. M.; Fert, A.; Nguyen Van Dau, F.; Petroff, F.; Eitenne, P.; Creuzet, G.; Friederich, A.; Chazelas, J. *Phys. Rev. Lett.* **1988**, *61*, 2472.

(64) Etienne, P.; Chazelas, J.; Creuzet, G.; Friederich, A.; Massies, J.; Nguyen Van Dau, F.; Fert, A. *J. Cryst. Growth* **1989**, *95*, 410.

(65) Barthelemy, A.; Fert, A.; Baibich, M. N.; Hadjoudj, S.; Petroff, F.; Etienne, P.; Cabanel, R.; Lequien, S.; Nguyen Van Dau, F.; Creuzet, G. *J. Appl. Phys.* **1990**, *67*, 5908.

(66) Barthelemy, A.; Baibich, M. N.; Broto, J. M.; Cabanel, R.; Creuzet, G.; Etienne, P.; Fert, A.; Friedrich, A.; Lequien, S.; et al. *Mater. Res. Soc. Symp. Proc.* **1989**, *151*, 43.

(67) Levy, P. M.; Zhang, S.; Fert, A. *Phys. Rev. Lett.* **1990**, *65*, 1643.

(68) Levy, P. M.; Ounadjela, K.; Zhang, S.; Wang, Y.; Sommers, C. B.; Fert, A. *J. Appl. Phys.* **1990**, *67*, 5914.

(69) Binasch, G.; Gruenberg, P.; Saurenbach, F.; Zinn, W. *Phys. Rev. B* **1989**, *39*, 4828.

(70) Wolf, S. A.; Awschalom, D. D.; Buhrman, R. A.; Daughton, J. M.; von Molnar, S.; Roukes, M. L.; Chtchelkanova, A. Y.; Treger, D. M. *Science* **2001**, *294*, 1488.

(71) Switzer, J. A. "*Handbook of Nanophase Materials"* **1997**, 63.

(72) Switzer, J. A.; Hung, C. J.; Breyfogle, B. E.; Shumsky, M. G.; Van Leeuwen, R.; Golden, T. D. *Science* **1994**, *264*, 1573.

(73) Hung, C.-J.; Gui, J.; Switzer, J. A. *Appl. Phys. Lett.* **1997**, *71*, 1637.

(74) Switzer, J. A.; Shane, M. J.; Phillips, R. J. *Science* **1990**, *247*, 444.

(75) Switzer, J. A.; Raffaelle, R. P.; Phillips, R. J.; Hung, C. J.; Golden, T. D. *Science* **1992**, *258*, 1918.

(76) Phillips, R. J.; Golden, T. D.; Shumsky, M. G.; Bohannan, E. W.; Switzer, J. A. *Chem. Mater.* **1997**, *9*, 1670.

(77) Prinz, G. A. *Science* **1998**, *282*, 1660.

(78) Dieny, B.; Speriosu, V. S.; Metin, S.; Parkin, S. S. P.; Gurney, B. A.; Baumgart, P.; Wilhoit, D. R. *J. Appl. Phys.* **1991**, *69*, 4774.

(79) Moodera, J. S.; Kinder, L. R.; Wong, T. M.; Meservey, R. *Phys. Rev. Lett.* **1995**, *74*, 3273.

(80) Miyazaki, T.; Tezuka, N. *J. Magn. Magn. Mater.* **1995**, *151*, 403.

(81) Yanase, A.; Siratori, K. *J. Phys. Soc. Jpn.* **1984**, *53*, 312.

(82) Zhang, Z.; Satpathy, S. *Phys. Rev. B* **1991**, *44*, 13319.

(83) Olsson, R. T.; Salazar-Alvarez, G.; Hedenqvist, M. S.; Gedde, U. W.; Lindberg, F.; Savage, S. J. *Chem. Mater.* **2005**, *17*, 5109.

(84) Sun, D.; Zhang, J.; Sun, D. *Adv. Mater. Res.* **2011**, *236-238*, 1893.

(85) Salazar-Alvarez, G.; Olsson, R. T.; Sort, J.; Macedo, W. A. A.; Ardisson, J. D.; Baro, M. D.; Gedde, U. W.; Nogues, J. *Chem. Mater.* **2007**, *19*, 4957.

(86) Song, Q.; Zhang, Z. J. *J. Am. Chem. Soc.* **2004**, *126*, 6164.

(87) Haetge, J.; Suchomski, C.; Brezesinski, T. *Inorg. Chem.* **2010**, *49*, 11619.

(88) Veith, M.; Haas, M.; Huch, V. *Chem. Mater.* **2005**, *17*, 95.

(89) Hastings, J. M.; Corliss, L. M. *Phys. Rev.* **1956**, *102*, 1460.

(90) Luders, U.; Barthelemy, A.; Bibes, M.; Bouzehouane, K.; Fusil, S.; Jacquet, E.; Contour, J.-P.; Bobo, J.-F.; Fontcuberta, J.; Fert, A. *Adv. Mater.* **2006**, *18*, 1733.

(91) Sun, S.; Zeng, H.; Robinson, D. B.; Raoux, S.; Rice, P. M.; Wang, S. X.; Li, G. *J. Am. Chem. Soc.* **2004**, *126*, 273.

(92) Vestal, C. R.; Zhang, Z. J. *Nano Lett.* **2003**, *3*, 1739.

(93) Nohira, T.; Yasuda, K.; Ito, Y. *Nat. Mater.* **2003**, *2*, 397.

(94) Jin, X.; Gao, P.; Wang, D.; Hu, X.; Chen, G. Z. *Angew. Chem. Int. Ed.* **2004**, *43*, 733.

(95) Xiao, W.; Jin, X.; Deng, Y.; Wang, D.; Chen, G. Z. *J. Electroanal. Chem.* **2010**, *639*, 130.

(96) Peng, J.; Jiang, K.; Xiao, W.; Wang, D.; Jin, X.; Chen, G. Z. *Chem. Mater.* **2008**, *20*, 7274.

(97) Han, W.-K.; Choi, J.-W.; Hwang, G.-H.; Hong, S.-J.; Lee, J.-S.; Kang, S.-G. *Appl. Surf. Sci.* **2006**, *252*, 2832.

(98) Wood, A. J. M.; Copcutt, R. C.; Chen, G. Z.; Fray, D. J. *Adv. Eng. Mater.* **2003**, *5*, 650.

(99) Fray, D. J.; Copcutt, R. C.*patent GB5414*, **2003**.

(100) Yan, X. Y.; Fray, D. J. *Adv. Funct. Mater.* **2005**, *15*, 1757.

(101) Allanore, A.; Lavelaine, H.; Valentin, G.; Birat, J. P.; Delcroix, P.; Lapicque, F. *Electrochimi. Acta* **2010**, *55*, 4007.

(102) Estelle, A. T. C.*US patent 1275161*, **1918**.

(103) Angel, E. G. R. *US patent 2622063*, **1952**.

(104) Allanore, A.; Lavelaine, H.; Valentin, G.; Birat, J. P.; Lapicque, F. *J. Electrochem. Soc.* **2008**, *155*, E125.

(105) Hartman, A. D.; Gerdemann, S. J.; Hansen, J. S. *JOM* **1998**, *50*, 16.

(106) Shah, A.; Torres, P.; Tscharner, R.; Wyrsch, N.; Keppner, H. *Science* **1999**, *285*, 692.

(107) Kroll, W. *Trans. Electrochem. Soc.* **1940**, *78*, 12 pp.

(108) Chen, G. Z.; Fray, D. J.; Farthing, T. W. *Nature* **2000**, *407*, 361.

(109) Ma, M.; Wang, D.; Wang, W.; Hu, X.; Jin, X.; Chen, G. Z. *J. Alloys Compd.* **2006**, *420*, 37.

(110) Centeno-Sanchez, R. L.; Fray, D. J.; Chen, G. Z. *J. Mater. Sci.* **2007**, *42*, 7494.

(111) Schwandt, C.; Alexander, D. T. L.; Fray, D. J. *Electrochimi. Acta* **2009**, *54*, 3819.

(112) Pyper, O.; Hahn, B.; Schoellhorn, R. *J. Mater. Chem.* **1997**, *7*, 465.

(113) Pfletschinger, G.; Hahn, B.; Schoellhorn, R. *Solid State Ionics* **1996**, *84*, 151.

(114) Walter, M. G.; Warren, E. L.; McKone, J. R.; Boettcher, S. W.; Mi, Q.; Santori, E. A.; Lewis, N. S. *Chem. Rev.* **2010**, *110*, 6446.

(115) Lewis, N. S. *Science* **2007**, *315*, 798.

(116) Fan, Z.; Javey, A. *Nat. Mater.* **2008**, *7*, 835.

(117) Barnham, K. W. J.; Mazzer, M.; Clive, B. *Nat. Mater.* **2006**, *5*, 161.

(118) Goetzberger, A.; Hebling, C. *Solar Energy Materials & Solar Cells* **2000**, *62*, 1.

(119) Bard, A. J.; Fox, M. A. *Acc. Chem. Res.* **1995**, *28*, 141.

(120) Gray, M. W. *Int. Rev Cytol.* **1992**, *141*, 233.

(121) Xiong, J.; Fischer, W. M.; Inoue, K.; Nakahara, M.; Bauer, C. E. *Science* **2000**, *289*, 1724.

(122) Tan, M. X.; Laibinis, P. E.; Nguyen, S. T.; Kesselman, J. M.; Stanton, C. E.; Lewis, N. S. *Prog. Inorg. Chem.* **1994**, *41*, 21.

(123) Lewis, N. S. *Nature* **2001**, *414*, 589.

(124) Lewis, N. S.; Nocera, D. G. *Proc. Natl. Acad. Sci. U S A* **2006**, *103*, 15729.

(125) Fujishima, A.; Honda, K. *Nature* **1972**, *238*, 37.

(126) Bard, A. J. *Science* **1980**, *207*, 139.

(127) Bard, A. J. *J. Phys. Chem.* **1982**, *86*, 172.

(128) Walter, M. G.; Warren, E. L.; McKone, J. R.; Boettcher, S. W.; Mi, Q.; Santori, E. A.; Lewis, N. S. *Chem. Rev.* **2011**, *111*, 5815.

(129) Chen, X.; Shen, S.; Guo, L.; Mao, S. S. *Chem. Rev.* **2010**, *110*, 6503.

(130) Aspnes, D. E.; Studna, A. A. *Phys. Rev. B* **1983**, *27*, 985.

(131) Aharon-Shalom, E.; Heller, A. *J. Electrochem. Soc.* **1982**, *129*, 2865.

(132) Paracchino, A.; Laporte, V.; Sivula, K.; Gratzel, M.; Thimsen, E. *Nat. Mater.* **2011**, *10*, 456.

(133) Mor, G. K.; Varghese, O. K.; Wilke, R. H.; Sharma, S.; Shankar, K.; Latempa, T. J.; Choi, K. S.; Grimes, C. A. *Nano Lett.* **2008**, *8*, 1906.

(134) Marsen, B.; Cole, B.; Miller, E. L. *Solar Energy Materials & Solar Cells* **2008**, *92*, 1054.

(135) Gasparotto, A.; Barreca, D.; Bekermann, D.; Devi, A.; Fischer, R. A.; Fornasiero, P.; Gombac, V.; Lebedev, O. I.; Maccato, C.; Montini, T.; Van Tendeloo, G.; Tondello, E. *J. Am. Chem. Soc.* **2011**, *133*, 19362.

(136) Domen, K.; Naito, S.; Soma, M.; Onishi, T.; Tamaru, K. *J. Chem. Soc.* **1980**, 543.

(137) Ishihara, T.; Nishiguchi, H.; Fukamachi, K.; Takita, Y. *J. Phys. Chem. B* **1999**, *103*, 1.

(138) Paulauskas, I. E.; Katz, J. E.; Jellison, G. E., Jr.; Lewis, N. S.; Boatner, L. A.; Brown, G. M. *J. Electrochem. Soc.* **2009**, *156*, B580.

(139) Morisaki, H.; Watanabe, T.; Iwase, M.; Yazawa, K. *Appl. Phys. Lett.* **1976**, *29*, 338.

(140) Mavroides, J. G.; Tchernev, D. I.; Kafalas, J. A.; Kolesar, D. F. *Mater. Res. Bull.* **1975**, *10*, 1023.

(141) Kay, A.; Cesar, I.; Graetzel, M. *J. Am. Chem. Soc.* **2006**, *128*, 15714.

(142) Zhong, D. K.; Gamelin, D. R. *J. Am. Chem. Soc.* **2010**, *132*, 4202.

(143) Sivula, K.; Zboril, R.; Le Formal, F.; Robert, R.; Weidenkaff, A.; Tucek, J.; Frydrych, J.; Gratzel, M. *J. Am. Chem. Soc.* **2010**, *132*, 7436.

(144) Sivula, K.; Le Formal, F.; Gratzel, M. *Chem. Mater.* **2009**, *21*, 2862.

(145) Chen, Y. W.; Prange, J. D.; Duhnen, S.; Park, Y.; Gunji, M.; Chidsey, C. E.; McIntyre, P. C. *Nat. Mater.* **2011**, *10*, 539.

(146) Kanan, M. W.; Nocera, D. G. *Science* **2008**, *321*, 1072.

(147) Kanan, M. W.; Surendranath, Y.; Nocera, D. G. *Chem. Soc. Rev.* **2009**, *38*, 109.

(148) Lutterman, D. A.; Surendranath, Y.; Nocera, D. G. *J. Am. Chem. Soc.* **2009**, *131*, 3838.

(149) Pijpers, J. J.; Winkler, M. T.; Surendranath, Y.; Buonassisi, T.; Nocera, D. G. *Proc. Natl. Acad. Sci. U S A* **2011**, *108*, 10056.

(150) Reece, S. Y.; Hamel, J. A.; Sung, K.; Jarvi, T. D.; Esswein, A. J.; Pijpers, J. J.; Nocera, D. G. *Science* **2011**, *334*, 645.

(151) Zhong, D. K.; Sun, J.; Inumaru, H.; Gamelin, D. R. *J. Am. Chem. Soc.* **2009**, *131*, 6086.

(152) Seabold, J. A.; Choi, K.-S. *Chem. Mater.* **2011**, *23*, 1105.

(153) Steinmiller, E. M. P.; Choi, K.-S. *Proc. Natl. Acad. Sci. U S A* **2009**, *106*, 20633.

(154) McAlpin, J. G.; Surendranath, Y.; Dinca, M.; Stich, T. A.; Stoian, S. A.; Casey, W. H.; Nocera, D. G.; Britt, R. D. *J. Am. Chem. Soc.* **2010**, *132*, 6882.

(155) Surendranath, Y.; Kanan, M. W.; Nocera, D. G. *J. Am. Chem. Soc.* **2010**, *132*, 16501.

(156) Xie, X.; Li, Y.; Liu, Z. Q.; Haruta, M.; Shen, W. *Nature* **2009**, *458*, 746.

(157) Hu, L.; Peng, Q.; Li, Y. *J. Am. Chem. Soc.* **2008**, *130*, 16136.

PAPER

I. Room-Temperature Electrochemical Reduction of Epitaxial Magnetite Films to Epitaxial Iron Films

Zhen He, Rakesh V. Gudavarthy, Jakub A. Koza, and Jay A. Switzer*

Department of Chemistry and Graduate Center for Materials Research, Missouri University of Science and Techology, Rolla, MO 65409-1170, USA

ABSTRACT

The electrochemical reduction of oxides to metals has been studied for decades. Earlier work produced polycrystalline bulk metals. Here, we report that pre-electrodeposited *epitaxial* face-centered cubic magnetite thin films can be electrochemically reduced to *epitaxial* body-centered cubic iron thin films in aqueous solution on single-crystalline gold substrates at room temperature. This technique opens up new possibilities to produce special epitaxial metal/metal oxide heterojunctions and a wide range of epitaxial metallic alloys films from the corresponding mixed metal oxides.

MAIN TEXT

The electrochemical reduction of metal oxides to the corresponding metals has been studied for several decades as an alternative route to pyrometallurgical processes for the metallurgy industry because of its simplicity, environmental friendliness, and low cost.[1-16] Fray and Chen pioneered this field with their work on the direct electrochemical reduction of titanium dioxide to titanium in molten calcium chloride at 950 ℃.[3-6] Cox and Fray also showed that iron(III) oxide could be electrochemically reduced to iron in molten NaOH at 530 ℃ by the same method.[7] In recent work, Allanore and co-workers

electrochemically reduced porous iron ore (α-Fe_2O_3, hematite) particles to iron in 10 M KOH solution at 100 ℃. They proposed a dissolution/re-deposition mechanism with magnetite (Fe_3O_4) as the intermediate.[8,9] In addition to TiO_2 and Fe_2O_3, more insulating oxides such as SiO_2 and ZrO_2 can also be reduced to Si and Zr, respectively.[10-13] Kang and co-workers showed that nano-size Cu particles can be fabricated by electrochemically reducing CuO nano-particles in neutral solution at 300 K.[14] However, the previous work in this field was designed to achieve large-scale and high-rate metal production as well as low CO_2 emissions, and it was conducted on bulk polycrystalline metal oxides. Although single-crystal Bi_2S_3 and BiOCl were reported to be electrochemically reduced to Bi metal via an electron/proton transfer reaction at ambient temperature, there was no correlation between the initial orientation of the oxide crystals and the orientation of the metal crystallites after reduction.[15,16] That is, the order of the single crystals was lost after reduction. Here, we report that *epitaxial* face-centered cubic (fcc) Fe_3O_4 thin films on gold single-crystalline substrates can be electrochemically reduced to *epitaxial* body-centered cubic (bcc) Fe thin films in 2 M NaOH solution at room temperature.

Fe_3O_4 is a half-metallic metal oxide with the inverse spinel structure and a cubic lattice parameter a = 0.8396 nm (space group *Fd*3*m*). Its conductive nature makes it a good candidate to study the electrochemical reduction to Fe. The epitaxial transformation of fcc-Fe_3O_4 to bcc-Fe is interesting to study because a pure solid-state transformation would require an ordered atom rearrangement in a solid at low temperature, with a large volume shrinkage from fcc-Fe_3O_4 to bcc-Fe. Fe has a lattice parameter of a = 0.2866 nm (space group *Im*3*m*). The volume of one Fe_3O_4 unit cell is 0.5919 nm^3, containing 24 Fe

atoms that can form 12 unit cells of bcc-Fe with a total volume of 0.2825 nm^3. Thus, the transformation from fcc-Fe_3O_4 to bcc-Fe will cause a 52.3% shrinkage in volume. Considering the large volume change during the transformation and the low ion mobility in solids at low temperature, it is surprising that the Fe films reduced from the precursor Fe_3O_4 layers are still epitaxial.

The electrochemical reduction of Fe_3O_4 to Fe was studied at temperatures ranging from 25 to 80 ℃ by linear sweep voltammetry (LSV). The potential was scanned from the open circuit potential (OCP) to -1.5 V vs. Ag/AgCl on the pre-deposited 200 nm thick Fe_3O_4 films[17] on a Au(110) single crystal and on a bare Au(110) single crystal in 2 M NaOH solution (see Figure 1). The LSV on the bare Au(110) shows only the cathodic current for water reduction starting at a potential of about -1.35 V vs. Ag/AgCl. The potential at which water reduction occurs on both the bare Au electrode and the Fe_3O_4 electrodes is shifted to more negative potentials than the thermodynamic potential due to a kinetic overpotential. The LSVs on the pre-deposited Fe_3O_4 films on Au(110) all have one cathodic peak before water reduction which is due to the reduction of the Fe_3O_4 films. The reduction of Fe_3O_4 begins at about -1.20 V at all the temperatures. Based on these LSVs, the films were electrochemically reduced by applying -1.22 V vs. Ag/AgCl. This potential is on the positive edge of the cathodic peaks for film reduction. The cathodic current density was typically 1-2 mA/cm^2 for reduction at 25 ^oC. If the films were reduced using the potentials corresponding to the peak currents (e.g., -1.4 V vs. Ag/AgCl at 25 ^oC), the rapid film reduction led to exfoliation of the film.

The out-of-plane orientations of the pre-deposited Fe_3O_4 films (about 600 nm thick) and the Fe films (about 200 nm thick) electrochemically reduced from the

precursor Fe_3O_4 films by applying a constant potential of -1.22 V vs. Ag/AgCl were determined by X-ray diffraction (XRD) θ-2θ scans. Plots of logarithm of intensity versus 2θ for the precursor Fe_3O_4 films (black line) and the Fe films (red line) on Au(100), Au(110) and Au(111) single-crystalline substrates are shown in Figure 2A-C. As we showed in previous work,[18,19] Fe_3O_4 films grow with a [111] out-of-plane orientation on both Au(100) and Au(111) and a [110] out-of-plane orientation on Au(110). The out-of-plane orientations of the Fe films after reduction are [100] on Au(100), [110] on Au(111), and [211] on Au(110). Different out-of-plane orientations of the Fe films were obtained on Au(100) and Au(111) after reduction, whereas the precursor Fe_3O_4 films have the same out-of-plane orientation. Hence, the orientations of the Fe films are controlled by the Au substrates instead of the precursor Fe_3O_4 films. This suggests that the reduction starts at the Fe_3O_4/Au interface. Control of the orientations of both Fe_3O_4 and Fe layers by the Au substrates is an interesting phenomenon that might be applicable to produce special Fe_3O_4/Fe heterojunctions by partially reducing the precursor Fe_3O_4 films (Supporting Information (SI) Figure S2), which are not likely obtainable by other direct deposition techniques, because the orientation of the upper layer is usually controlled by the directly contacted bottom layer (SI Figure S1).

Texture analysis was used in order to probe the in-plane orientations of the precursor Fe_3O_4 films and the Fe films after reduction on all three Au single crystals. The (311) pole figures of the precursor Fe_3O_4 films on Au single crystals are shown in Figure 2D-F. The pole figures demonstrate that the Fe_3O_4 films were epitaxially deposited on all three types of Au single crystals.[18] The pole figures of both the Fe_3O_4 precursor films and the Fe films after electrochemical reduction have spot patterns instead of ring patterns,

showing that the films have both out-of-plane and in-plane order. The epitaxial relationships are determined by comparing the experimentally measured pole figures to calculated stereographic projections (SI Figure S3). The (110) pole figure of the Fe film on Au(100) in Figure 2G shows that the epitaxial relationship for the Fe film on Au(100) is Fe(100)[001]//Au(100)[011]. The (110) pole figure of Fe (Figure 2H) on Au(110) shows that there are two Fe domains on Au(110): Fe(211)[$01\bar{1}$]//Au(110)[001] and Fe(211)[$01\bar{1}$]//Au(110)[$00\bar{1}$]. The (211) pole figure of Fe film on Au(111) shown in Figure 2I shows that there are three domains of Fe film on the Au(111) substrate: Fe(110)[$1\ \bar{1}\ 0$]//Au(111)[$\bar{1}\ \bar{1}\ 2$], Fe(110)[$1\ \bar{1}\ 0$]//Au(111)[$2\ \bar{1}\ \bar{1}$], and Fe(110)[$1\bar{1}0$]//Au(111)[$\bar{1}2\bar{1}$].

The lattice mismatch between the Fe films and the Au single-crystalline substrates can be calculated based on the Fe/Au interface models shown in Figure 3, which were generated according to the epitaxial relationships obtained from the XRD θ-2θ scans and pole figure measurements. As shown in Figure 3A, on Au(100), the Fe(100) film and the Au(100) substrate has only -0.62% lattice mismatch along both Au[011] and Au[$01\bar{1}$] directions. However, on Au(110), the lattice mismatches of the Fe(211) and the Au(110) planes are -13.94% and -0.61% along the two orthogonal Au[$1\bar{1}0$] and [001] directions (Figure 3B). The situation on Au(111) is similar to that on Au(110). The Fe(110) and Au(111) planes have a small mismatch of -0.62% along Au[$\bar{1}10$] and a large mismatch of -18.80% along Au[$\bar{1}\bar{1}2$]. Therefore, the sequence of the lattice mismatches of Fe films on Au single crystals from small to large is Fe(100) on Au(100) < Fe(211) on Au(110) < Fe(110) on Au(111).

Another way to determine whether the reduction of Fe_3O_4 to Fe starts at the Au/Fe_3O_4 interface or at the Fe_3O_4/electrolyte interface is direct observation based on cross-sectional SEM images and plan-view photomicrographs of a partially reduced Fe_3O_4 film on Au. The cross-sectional SEM image of the Fe_3O_4 film before partial reduction (Figure 4a) on an Au sputtered glass substrate shows that the Fe_3O_4 film (top layer) has a columnar structure and the bright Au layer has a thickness of about 100 nm which matches with the manufacturer's description (1000 Å). After partial reduction (Figure 4B) the upper Fe_3O_4 and the Au layer are unchanged. Between the Au and Fe_3O_4 a layer of Fe nano-particles with a thickness of about 100 to 150 nm can be seen. The insets in Figure 4C are plan-view photographs of the as-deposited magnetite film, partially reduced magnetite film, and Fe film after com plete reduction. The surface of the electrodeposited Fe_3O_4 film on Au(110) has a black appearance with a crystal size of 200 to 300 nm (as shown in SI Figure S4). After partial reduction, the XRD θ-2θ scan (Figure 4C) confirms that part of the precursor Fe_3O_4(110) film has been reduced to a Fe(211) film. However, the photograph of the partially reduced magnetite film shows no obvious change of the Fe_3O_4 film surface. After completely reducing at room temperature until the cathodic current reached a plateau, there was a very thin layer of brownish-black film loosely attached to the surface that could be easily removed by flushing with distilled water. XRD and Raman analysis of this surface film show that it is Fe_3O_4, but the grain size measured by SEM was larger than that of the initial Fe_3O_4. After the top unreduced layer was removed, the Fe film with a shiny metallic gloss was exposed and the crystal size is around 100 to 150 nm based on the SEM image (SI Figure S4). These direct observations suggest that the reduction of Fe_3O_4 to Fe does not start at the

Fe_3O_4/electrolyte interface but, rather, at the Fe_3O_4/Au interface, which agrees with the indirect deduction based on the X-ray characterization results.

In order to further analyze the Fe reduction product, magnetic investigations were performed. Hysteresis loops of the as-deposited Fe_3O_4 thin film as well as the Fe layer obtained after the reduction on the Au(110) crystal are shown in Figure 5. For both of the films the easy axis of magnetization lies in the film plane. From the hysteresis loops obtained normal to the film plane, anisotropy fields have been estimated (indicated by arrows in Figure 5) to be ~0.55 T and ~1.7 T for as-deposited Fe_3O_4 and Fe films, respectively. The value for the Fe_3O_4 film is very close to the saturation magnetization of Fe_3O_4 indicating a predominant contribution of shape anisotropy, as already reported by other researchers.[20] The hysteresis loop for the Fe film has a significantly larger anisotropy field than Fe_3O_4. The estimated anisotropy field is very close to the saturation magnetization of pure Fe, which further proves that the reduction product is Fe. Additionally, as mentioned, the Fe_3O_4/Fe heterostructures with different epitaxial relationships can be formed, which may show interesting exchange coupling phenomena.

From our experiments it is not possible to determine whether the reduction of Fe_3O_4 to Fe occurs by a solid-state transformation or through a dissolution/re-deposition route. The fact that the reaction occurs at the Au/Fe_3O_4 interface suggests a solid-state transformation, whereas the large currents observed in Figure 1 are more consistent with the dissolution/redeposition route. The solid-state transformation would occur by reducing Fe_3O_4 to Fe and O^{2-}(eq. 1). The O^{2-} would then be transported to the surface (eq. 2), where it would react with H_2O to produce OH^-(eq. 3).

$$Fe_3O_4 + 8e^- \leftrightarrows 3Fe + 4O^{2-}_{bulk} \quad (1)$$

$$4O^{2-}_{bulk} \leftrightarrows 4O^{2-}_{surface} \quad (2)$$

$$4O^{2-}_{surface} + 4H_2O \leftrightarrows 8OH^- \quad (3)$$

However, the diffusion coefficient of O^{2-} in magnetite would be exceedingly small at room temperature, because it has been measured[21] to be 5.6×10^{-19} cm^2/s at 500 ^oC, compared with values in the 10^{-6} cm^2/s range for aqueous ions. Of course, transport of O^{2-} along grain boundaries or in nanophase material at the Au/Fe_3O_4 interface could be much faster than the previously measured bulk values. It is also possible that the O^{2-} ions do not need to diffuse through the entire film, but they can be released directly into electrolyte that has infiltrated through the capillaries between the columnar grains of Fe_3O_4. This would be in line with the three-phase interlines (3PIs) model.[5,22,23] The dissolution/redeposition route is consistent with the mechanism proposed by Allanore et al. for reduction of Fe_2O_3 in strongly alkaline solution. This route would occur according to eqs. 4 and 5. In this case the Fe_3O_4 is electrochemically reduced to a soluble Fe(II) species such as $Fe(OH)_3^-$, which is then reduced at the Au electrode to Fe. Again, for this mechanism to explain the deposition of Fe at the Au surface, it is necessary to invoke the concept of infiltration of electrolyte into the film.

$$Fe_3O_4 + 2e^- + 4H_2O + OH^- \leftrightarrows 3Fe(OH)^{3-} \quad (4)$$

$$3Fe(OH)^{3-} + 6e^- \leftrightarrows 3Fe + 9OH^- \quad (5)$$

In addition to Fe_3O_4 to Fe conversion, our preliminary experimental results also showed that alloy films with a controlled metal ratio can be produced by electrochemical reduction of the corresponding mixed metal oxide films. We electrochemically reduced a cobalt-substituted Fe_3O_4 film and measured the cobalt concentrations in both the precursor oxide film and the metallic film after reduction. The results show that the atomic cobalt concentrations are 16.2% in the precursor oxide film and 16.0% in the metallic film after reduction, with the XRD pattern of the metallic film after reduction matching with the CoFe alloy. This indicates that the metals concentration ratio in the alloy film can be determined by the ratio in the precursor mixed metal oxide film.

We have shown that epitaxial Fe_3O_4 films on single-crystal Au can be electrochemically reduced to epitaxial Fe films that maintain the single-crystal-like order of the Fe_3O_4 precursor (see scheme in Figure 6). The reduction starts at the Fe_3O_4/Fe interface instead of the Fe_3O_4/solution interface, with the orientation of the resulting Fe film determined by the Au substrate. In addition to producing pure Fe films, we have shown that Fe_3O_4/Fe heterojunctions can be produced by partially reducing the Fe_3O_4, and that Fe/Co alloys can be produced from cobalt-substituted Fe_3O_4. The method should be quite general. For example, we anticipate that it should be possible to reduce epitaxial films of other metal oxides such as Bi_2O_3,[15,24,25] Cu_2O,[26] and CuO[27] to the corresponding epitaxial metals. Because the orientation of the films are determined by the single-crystal substrate, it is interesting to speculate whether amorphous films of SiO_2 could be reduced in nonaqueous solvents or molten salts to epitaxial films of Si on ordered substrates.[10-12] This would provide an inexpensive method to produce large-scale epitaxial Si films for electronic and photovoltaic applications.

ASSOCIATED CONTENT

Supporting Information. Experimental details. This material is available free of charge via the Internet at http://pubs.acs.org.

AUTHOR INFORMATION

Corresponding Author

jswitzer@mst.edu

ACKNOWLEDGEMENT

This work was supported by the U.S. Department of Energy, Office of Basic Energy Science, under Grant No. DE-FG0208ER46518.

REFERENCES

(1) Oswin, H. G.; Cohen, M. *J. Electrochem. Soc.* **1957**, 104, 9.

(2) LeDuc, J. A. M.; Loftfield, R. E.; Vaaler, L. E. *J. Electrochem. Soc.* **1959**, 106, 659.

(3) Chen, G. Z.; Fray, D. J.; Farthing, T. W. *Nature* **2000**, 407, 361.

(4) Jiang, K.; Hu, X.; Ma, M.; Wang, D.; Qiu, G.; Jin, X.; Chen, G. Z. *Angew. Chem., Int. Ed.* **2006**, 45, 428.

(5) Li, W.; Jin, X.; Huang, F.; Chen, G. Z. *Angew. Chem., Int. Ed.* **2010**, 49, 3203.

(6) Centeno-Sanchez, R. L.; Fray, D. J.; Chen, G. Z. *J. Mater. Sci.* **2007**, 42, 7494.

(7) Cox, A.; Fray, D. J. *J. Appl. Electrochem.* **2008**, 38, 1401.

(8) Allanore, A.; Lavelaine, H.; Valentin, G.; Birat, J. P.; Delcroix, P.; Lapicque, F. *Electrochim. Acta* **2010**, 55, 4007.

(9) Allanore, A.; Lavelaine, H.; Valentin, G.; Birat, J. P.; Lapicque, F. *J. Electrochem. Soc.* **2008**, 155, E125.

(10) Nohira, T.; Yasuda, K.; Ito, Y. *Nat. Mater.* **2003**, 2, 397.

(11) Jin, X.; Gao, P.; Wang, D.; Hu, X.; Chen, G. Z. *Angew. Chem., Int. Ed.* **2004**, 43, 733.

(12) Xiao, W.; Jin, X.; Deng, Y.; Wang, D.; Chen, G. Z. *J. Electroanal. Chem.* **2010**, 639, 130.

(13) Peng, J.; Jiang, K.; Xiao, W.; Wang, D.; Jin, X.; Chen, G. Z. *Chem. Mater.* **2008**, 20, 7274.

(14) Han, W.-K.; Choi, J.-W.; Hwang, G.-H.; Hong, S.-J.; Lee, J.-S.; Kang, S.-G. *Appl. Surf. Sci.* **2006**, 252, 2832.

(15) Pyper, O.; Hahn, B.; Schoellhorn, R. *J. Mater. Chem.* **1997**, 7, 465.

(16) Pfletschinger, G.; Hahn, B.; Schoellhorn, R. *Solid State Ionics* **1996**, 84, 151.

(17) Kothari, H. M.; Kulp, E. A.; Limmer, S. J.; Poizot, P.; Bohannan, E. W.; Switzer, J. A. *J. Mater. Res.* **2006**, 21, 293.

(18) Kulp, E. A.; Kothari, H. M.; Limmer, S. J.; Yang, J.; Gudavarthy, R. V.; Bohannan, E. W.; Switzer, J. A. *Chem. Mater.* **2009**, 21, 5022.

(19) Switzer, J. A.; Gudavarthy, R. V.; Kulp, E. A.; Mu, G.; He, Z.; Wessel, A. J. *J. Am. Chem. Soc.* **2010**, 132, 1258.

(20) Horng, L.; Chern, G.; Chen, M. C.; Kang, P. C.; Lee, D. S. *J. Magn. Magn. Mater.* **2004**, 270, 389.

(21) Castle, J. E.; Surman, P. L. *J. Phys. Chem.* **1967**, 71, 4255.

(22) Deng, Y.; Wang, D.; Xiao, W.; Jin, X.; Hu, X.; Chen, G. Z. *J. Phys. Chem. B* **2005**, 109, 14043.

(23) Xiao, W.; Jin, X.; Deng, Y.; Wang, D.; Chen, G. Z. *Chem.--Eur. J.* **2007**, 13, 604.

(24) Switzer, J. A.; Shumsky, M. G.; Bohannan, E. W. *Science* **1999**, 284, 293.

(25) Qiu, Y.; Liu, D.; Yang, J.; Yang, S. *Adv. Mater.* **2006**, 18, 2604.

(26) Switzer, J. A.; Hung, C. J.; Bohannan, E. W.; Shumsky, M. G.; Golden, T. D.; Van Aken, D. C. *Adv. Mater.* **1997**, 9, 334.

(27) Switzer, J. A.; Kothari, H. M.; Poizot, P.; Nakanishi, S.; Bohannan, E. W. *Nature* **2003**, 425, 490.

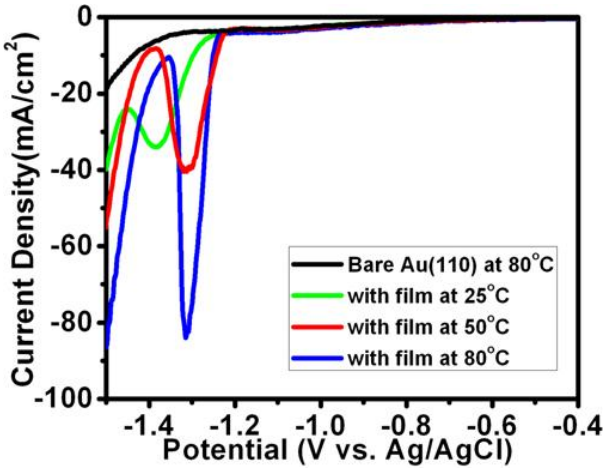

Figure 1. Linear sweep voltammograms on a bare Au(110) single crystal and on Au(110) with pre-deposited Fe_3O_4 films. All the voltammograms were run at a scan rate of 25 mV/s and stirring rate of 200 rpm in 2 M NaOH.

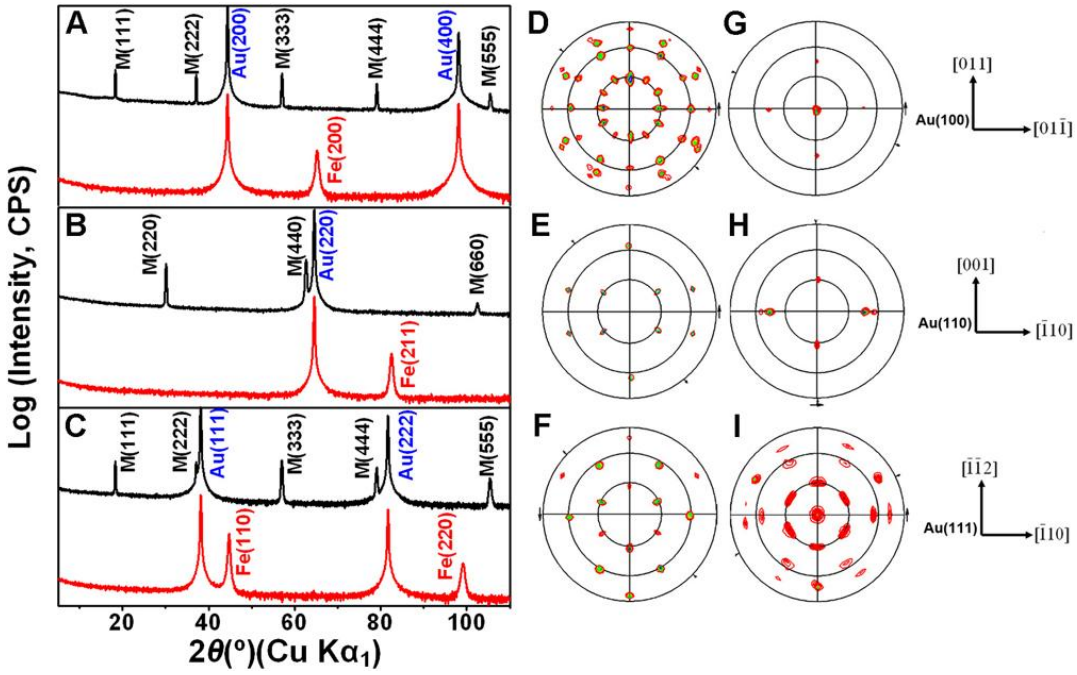

Figure 2. X-ray diffraction characterization of electrodeposited Fe_3O_4 films and the corresponding Fe films electrochemically reduced from the precursor Fe_3O_4 films. θ-2θ scans of Fe_3O_4 and Fe films on (A) Au(100), (B) Au(110) and (C) Au(111). Black lines represent scans on Fe_3O_4 and red lines represent scans on Fe films. The symbol 'M' in this figure represents magnetite (Fe_3O_4). (311) pole figures of the Fe_3O_4 films on (D) Au(100), (E) Au(110) and (F) Au(111). (110) pole figures of Fe on (G) Au(100) and (H) Au(110), and (I) (211) pole figure of Fe on Au(111).

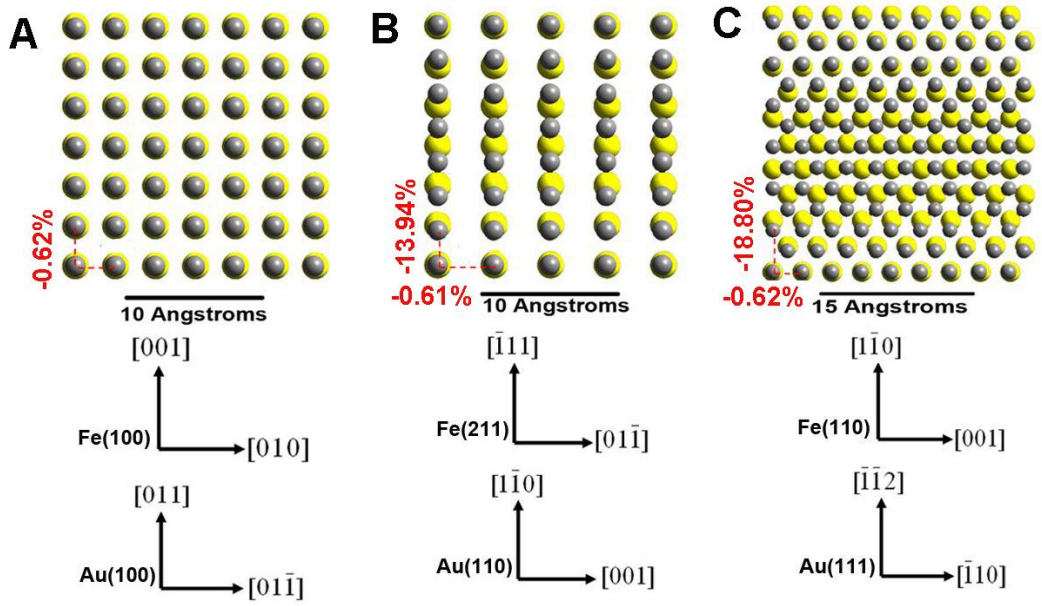

Figure 3. Interface models of the Fe films reduced from the precursor Fe_3O_4 films on (A) Au(100), (B) Au(110) and (c) Au(111). The yellow balls represent Au atoms while the grey balls on the top represent Fe atoms.

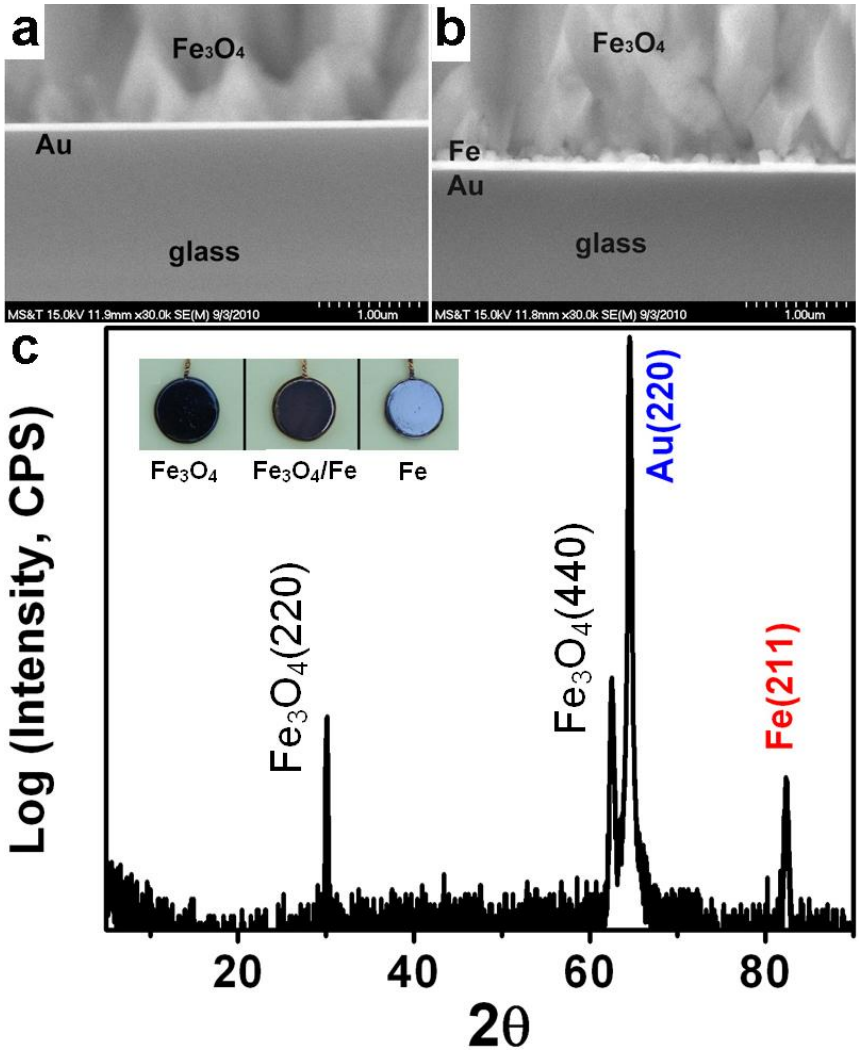

Figure 4. Evidence that the reduction of Fe_3O_4 to Fe starts at the Fe_3O_4/Au interface. SEM cross-sectional images of precursor Fe_3O_4 film on Au sputtered glass (A) before and (B) after partial reductions. (C) X-ray θ-2θ scan of partially reduced Fe_3O_4 film on a Au(110) single crystal. The insets in (C) are plan-view photographs of the as-deposited Fe_3O_4 film (left), partially reduced Fe_3O_4 film (middle), and the Fe film (right) completely reduced from the Fe_3O_4 film on Au(110).

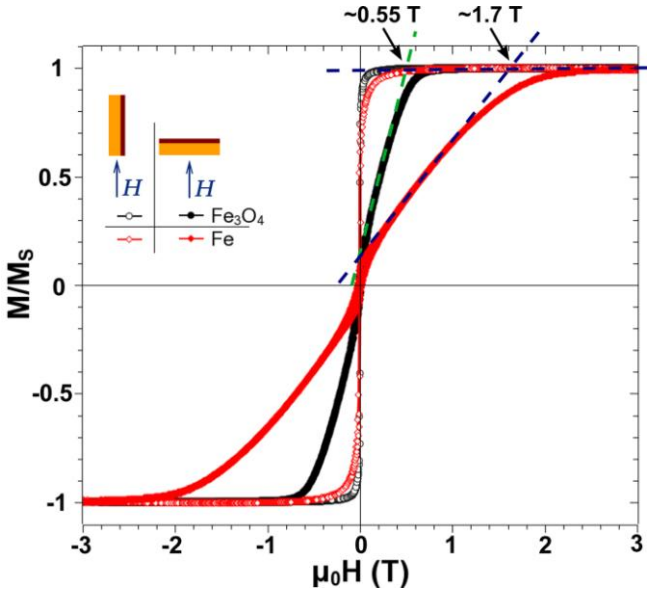

Figure 5. Normalized magnetization vs. magnetic field hysteresis loops of the as-deposited Fe_3O_4 film and the Fe film reduced from the precursor Fe_3O_4 film on a single-crystal Au(110) substrate.

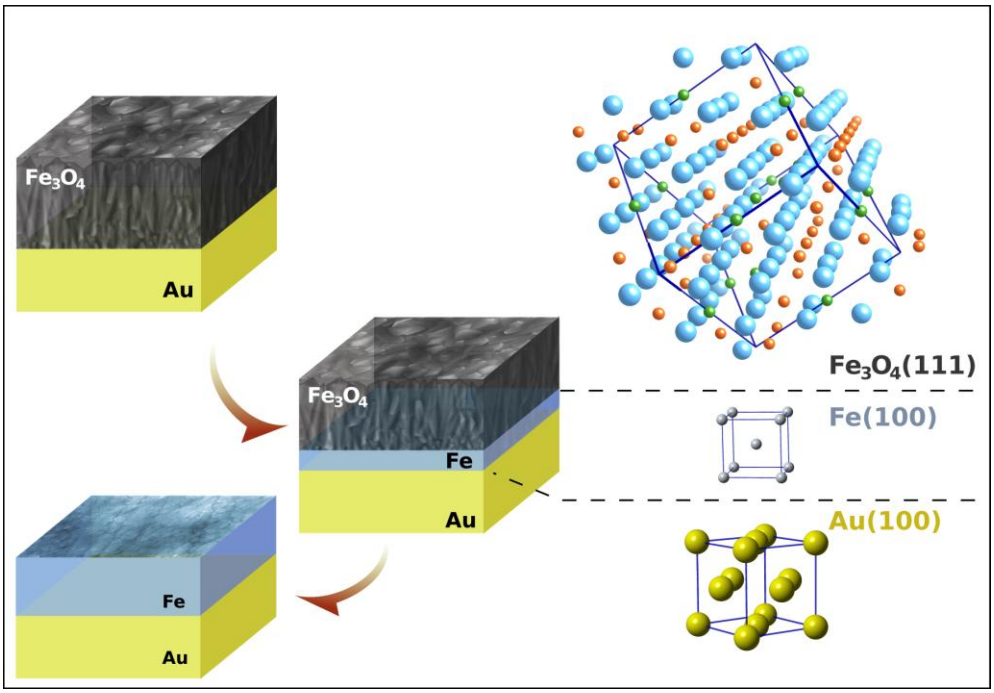

Figure 6. Scheme for the reduction of epitaxial Fe_3O_4 film to epitaxial Fe film on an Au single-crystalline substrate. The reduction of Fe_3O_4(111) to Fe(100) on Au(100) is shown as an example.

II. Electrodeposition of $Co_xFe_{3-x}O_4$ Epitaxial Films and Superlattices

Zhen He, Jakub A. Koza, Guojun Mu, Andrew S. Miller, Eric W. Bohannan, and Jay A. Switzer*

Department of Chemistry and Graduate Center for Materials Research, Missouri University of Science and Technology, Rolla, MO 65409-1170, USA

KEYWORDS: electrodeposition, cobalt ferrite, epitaxial, superlattices, resistance switching

ABSTRACT

Spinel ferrites are of interest because of their potential applications in spintronics (spin-based electronics), memories, and magnetoreception devices. Cobalt ferrite ($CoFe_2O_4$) is an inverse spinel ferrite. The utility of $CoFe_2O_4$ is mainly based on its high coercivity and magnetocrystalline and shape anisotropy. The magnetic and electric properties of $CoFe_2O_4$ depend on its Co:Fe ratio. In this paper, a one-step electrodeposition of $Co_xFe_{3-x}O_4$ ($0<x<1$) thin films from an alkaline Fe^{3+}-Co^{2+}-triethanolamine solution is presented. The atomic Co:Fe ratio in the deposited $Co_xFe_{3-x}O_4$ thin films can be tuned by controlling the deposition potential. Effects of the chemical composition on the structure and the electric and magnetic properties of the $Co_xFe_{3-x}O_4$ films were investigated. Superlattices in the $Co_xFe_{3-x}O_4$ system were also electrodeposited from the same solution by simply pulsing between two potentials. Compared to $Co_xFe_{3-x}O_4$ individual films, superlattices exhibit resistance switching and a more pronounced negative differential resistance (NDR) feature at lower current during

perpendicular transport measurements. $Co_xFe_{3-x}O_4$ superlattices also show more complex magnetization switching behaviors than individual films. All $Co_xFe_{3-x}O_4$ films and superlattices show angular-dependent magnetoresistance, which has potential application in mimicking the magnetoreception systems in animals such as homing pigeons and magnetotactic bacteria.

INTRODUCTION

Spinel ferrites have received intense attention because of their potential applications in magnetic tunnel junctions (MTJs), magnetic random access memories (MRAMs), spin valves, resistive random access memories (RRAMs), microwave devices, biomedicines, and multiferroic nanostructures.[1-8] The chemical composition of stoichiometric spinel ferrites can be represented as MFe_2O_4, in which M is usually a 3d transition metal or a combination of them. When M=Fe, the resulting spinel ferrite, Fe_3O_4, is the oldest and the most studied magnetic material in history. Fe_3O_4 is of interest because it is ferrimagnetic below a high Curie temperature (~ 860 K) and has a predicted -100% spin polarization at the Fermi Level.[9,10] Recently, research on spinel ferrites has been focusing on mixed ferrites, in which the Fe ions of Fe_3O_4 are partially substituted by other 3d transition metal ions. By substituting to different degrees, stoichiometric or non-stoichiometric mixed ferrites with varied structural, magnetic, and electric properties can be formed. Examples include the increase of the magnetoresistance (MR) by Zn or Ni substitution,[11,12] improvement of the thermodynamic stability by Mn substitution,[13] and increase of resistivity by Co, Zn, or Mn substitution.[14-17]

Spinel ferrites have a face-centered cubic (fcc) structure. Depending on how the divalent and trivalent ions are distributed between the 8 tetrahedral sites (A sites) and 16 octahedral sites (B sites) in one unit cell, they can be divided into two types: normal spinel and inverse spinel. In normal spinel, all the A sites are occupied by divalent ions whereas in inverse spinel, all the A sites are occupied by trivalent ions. Fe_3O_4 has an inverse spinel structure. For mixed ferrites, Mn^{2+} and Zn^{2+} tend to occupy the A sites, while Co^{2+} and Ni^{2+} prefer to occupy the B sites.[18-20]

Cobalt ferrite, $CoFe_2O_4$, has a Curie temperature of ~ 790 K, below which it exhibits ferrimagnetism. Like Fe_3O_4, it has an inverse spinel structure[19,20] or near inverse spinel structure depending on its thermal history.[21,22] The magnetic moments of the Fe^{2+} and Fe^{3+} ions at the octahedral and tetrahedral sites antiferromagnetically cancel each other out, resulting in a net magnetic moment between 2.73 to 3 μ_B/f.u. due to the Co^{2+} ions at the octahedral sites. It has a high coercivity compared to other ferrites, like Fe_3O_4, which makes it a potential candidate for various magnetic applications, such as the pinning layer of spin valves or magnetic tunnel junctions. It has been reported recently by different groups that the electric and magnetic properties of the $CoFe_2O_4$ films are tunable by controlling the atomic Co:Fe ratio, microstructure, and residual strain.[15,23-28] At room temperature, Fe_3O_4 is a conductor (~ 4×10^{-5} Ω m) and $CoFe_2O_4$ is an insulator (~ 10^5 Ω m). The resistivity of the Co-substituted Fe_3O_4, $Co_xFe_{3-x}O_4$ ($0<x<1$), increases as the atomic cobalt concentration increases. This fact makes $Co_xFe_{3-x}O_4$ with certain Co:Fe ratios better candidates than Fe_3O_4 as an efficient spin injector, as it can have both large spin polarization at the Fermi level and a small conductivity mismatch with semiconductors.[27,29-31] $CoFe_2O_4$ films have the largest magnetic anisotropy constant

among the cubic ferrites.[3] For applications in spintronic devices and understanding the large anisotropy of Co atoms in a spinel structure, the growth of epitaxial films of $Co_xFe_{3-x}O_4$ is critical. Thin films of $Co_xFe_{3-x}O_4$ have been synthesized by pulsed laser deposition (PLD),[28,32] molecular beam epitaxy (MBE),[27] cosputtering technique,[15,25], laser molecular beam epitaxy (LMBE),[33] and atomic layer deposition (ALD).[34] To our best knowledge, there is no report on the electrodeposition of crystalline $Co_xFe_{3-x}O_4$ thin films without first depositing CoFe metal precursors.[35,36] In this paper, we report a one-step electrodeposition method for epitaxial $Co_xFe_{3-x}O_4$ films. The Co:Fe ratio in the $Co_xFe_{3-x}O_4$ films can be tuned by simply varying the deposition potential. Effects of the chemical composition on the structure and electric and magnetic properties of the $Co_xFe_{3-x}O_4$ films are discussed in this paper.

Besides epitaxial $Co_xFe_{3-x}O_4$ films, compositional superlattices in the $Co_xFe_{3-x}O_4$ system can also be electrodeposited from the same solution by simply pulsing between two potentials. We have shown in previous work that we can electrodeposit both defect chemistry and compositional superlattices.[8,37-39] Superlattices have a unique advantage because they combine nanometer-scale dimensions of individual layer thickness with the utility of large-scale films (e.g. micrometer scale) that can be conveniently connected in real devices. For some applications, nanophase materials are needed to fulfill the property requirements, however they are difficult to manipulate. Our $Co_xFe_{3-x}O_4$ superlattice shows a resistance switching and negative differential resistance (NDR) feature at lower current compared to the individual $Co_xFe_{3-x}O_4$ films. It also shows different behaviors in the magnetic and magneto-transport measurements, which could be due to the exchange coupling between the alternating layers and also the shape anisotropy of nano-scale

individual layers in the superlattice. Moreover, all the $Co_xFe_{3-x}O_4$ individual films and superlattices show angular-dependent magnetoresistance (MR). Utilizing this property, $Co_xFe_{3-x}O_4$ could be potentially used in direction-sensing sensors by mimicking the Fe_3O_4-based magnetoreception in animals, such as the alternating structure of the Fe_3O_4 platelets/Fe_2O_3 clusters in the beak of a homing pigeon[40] and the aligned Fe_3O_4 single crystal cubes in magnetotactic bacteria.[41]

EXPERIMENTAL SECTION

Electrodeposition of $Co_xFe_{3-x}O_4$ films and superlattices. $Co_xFe_{3-x}O_4$ films were electrodeposited onto Au-sputtered glass or Au single-crystalline substrates from a stirred solution containing 50 mM Fe^{3+}, 50 mM Co^{2+}, 100 mM triethanolamine (TEA), and 2 M NaOH at 80 °C by applying constant potentials using a Brinkmann PGSTAT 30 Autolab potentiostat. To study the structure and composition of $Co_xFe_{3-x}O_4$, films were deposited onto Au- sputtered glass substrates in the potential range between -0.95 and -1.03 $V_{Ag/AgCl}$ at increments of -0.02 $V_{Ag/AgCl}$. For epitaxial studies, $Co_xFe_{3-x}O_4$ films were electrodeposited onto Au(111) single crystals. Superlattices of $Co_xFe_{3-x}O_4$ were also deposited on Au(111) single crystals from the same solution by pulsing between -1.03 and -0.95 $V_{Ag/AgCl}$. Before deposition, Au(111) single crystals were electropolished in a solution containing 25 vol% ethylene glycol, 25 vol% HCl, and 50 vol% ethanol at 55 °C by applying an anodic current density of $\sim$1.5 A/cm^2.

X-ray diffraction (XRD) and Raman spectroscopy characterization. The electrodeposited $Co_xFe_{3-x}O_4$ films and superlattices were analyzed by using a high-resolution Philips X-Pert MRD X-ray diffractometer with a CuKα1 radiation source (λ =

0.154056 nm). The θ-2θ scans were obtained using the line focus mode with a hybrid monochromator consisting of a Göbel X-ray mirror and a Ge[220] 2-bounce, 2-crystal monochromator as the primary optic and a 0.18° thin film collimator as the secondary optic. The texture analysis (pole figure) was operated in the point focus mode using a 2 mm × 2 mm crossed slit collimator with a Ni filter as the primary optic and a 0.27° parallel plate collimator with a flat graphite monochromator as the secondary optic. Pole figures were run by first setting the diffraction angle, 2θ, for a plane that was not parallel with the surface of the material. Then, the tilt angle, χ, was changed from 0° to 90° with an interval of 3°, rotating the azimuthal angle at each tilt angle from φ = 0° to 360° with an interval of 3°.

Raman spectra of the films were measured using a Horiba Jobin-Yvon Lab Ram Aramis Microscope with a HeNe laser (λ=633 nm) as the excitation source with an incident power of about 5 mW in order to prevent the samples from being oxidized. Fe_3O_4 and $Co_xFe_{3-x}O_4$ films for Raman spectroscopy measurements were electrodeposited onto Au sputtered glass.

Surface morphology and composition investigations. The surface morphologies and Co:Fe ratios of the $Co_xFe_{3-x}O_4$ films were studied by a Hitachi S-4700 field-emission scanning electronic microscope (FE-SEM) equipped with an energy dispersive spectroscopy (EDS) system at an accelerating voltage of 15 kV. The atomic Co:Fe ratio of the $Co_xFe_{3-x}O_4$ films was determined by measuring the Co:Fe ratio at 5 different spots of the sample using EDS and then averaging the values.

Resistivity measurements. The resistivity of the $Co_xFe_{3-x}O_4$ films was measured by using four-point probe measurement. The $Co_xFe_{3-x}O_4$ films with different Co:Fe ratios

were deposited at -0.95, -0.97, -0.99, -1.01, -1.03 $V_{Ag/AgCl}$ onto gold sputtered glass. The thickness of the films was determined by using Dektak IIA Surface Profilometer. Before the resistivity measurement, the films were peeled off onto a non-conducting microscope glass slide using a commercial adhesive. The four-point resistivity of the films was measured in air using an Alessi model CPS-06 contact station with Keithley model 220 programmable current source and model 181 nanovoltmeter.

Resistance switching studies. The current-voltage (*iV*) curves of the $Co_xFe_{3-x}O_4$ films and superlattices were measured at 77K (in liquid N_2) using an EG&G Princeton Applied Research PARSTAT 2273 potentiostat/galvanostat. One silver wire was attached to the film surface with indium metal while another silver wire was connected to the gold substrate. For *iV* curves, the working electrode and sensor leads from the potentiostat were connected to the film surface. The reference and counter electrode leads from the potentiostat were connected to the gold substrate. The bias was measured as the applied current was swept from 0 to 2 A at 50 mA/s. The instrumental limit for the PARSTAT 2273 potentiostat/galvanostat is ±2 A.

Magnetic properties measurements. Magnetic and magnetotransport property measurements of the $Co_xFe_{3-x}O_4$ films and superlattices were performed in the Quantum Design Physical Property Measurement System (PPMS). The magnetic properties were measured with a Vibrating Sample Magnetometer (VSM) option in the direction of the film plane and normal to the film plane at different temperatures up to a field strength of 3.5 T, which was sufficient to saturate all the investigated samples. The contribution of the diamagnetic substrate was subtracted. The magnetoresistance (MR) and resistance vs. temperature dependence was measured by a resistivity option of the PPMS with a

horizontal rotator that allows performing of angular-dependent measurements. Two silver wires were attached to the film and to the Au substrate respectively by using pressed In contacts. The resistance was measured with a two-point method normal to the film plane. The MR was measured up to a field strength of 5 T. The angular-dependent MR was determined in a magnetic field of 2 T.

RESULTS AND DISCUSSION

The electrodeposition of $Co_xFe_{3-x}O_4$ is believed to follow an electrochemical-chemical (EC) mechanism, similar to what we previously proposed for the electrodeposition of magnetite and zinc ferrite.[8,42] It can be described by the following two equations:

$$Fe(TEA)^{3+} + e^- \rightarrow Fe(TEA)^{2+} \quad (1)$$

$$(1\text{-}x)Fe(TEA)^{2+} + xCo(TEA)^{2+} + 2Fe(TEA)^{3+} + 8OH^- \rightarrow$$

$$Co^{2+}{}_xFe^{2+}{}_{(1-x)}Fe^{3+}{}_2O_4 + 3TEA + 4H_2O \quad (2)$$

Four linear sweep voltammograms (LSVs) at 50 mV/s on a Au rotating-disk electrode (RDE) in different solutions are shown in Figure 1a. These solutions all contain 2 M NaOH and 100 mA TEA, but different concentrations of Fe^{3+} and Co^{2+}. The LSVs are used to find the potential window where the Fe^{3+} is reduced to Fe^{2+} while Co^{2+} is not reduced. The black LSV run in the NaOH-TEA solution shows only the cathodic current for H_2O reduction starting at ~ -1.15 $V_{Ag/AgCl}$. The blue LSV in the solution with Co^{2+} shows that the $Co(TEA)^{2+}$ is reduced at ~ -1.05 $V_{Ag/AgCl}$. The red LSV in the solution

with Fe^{3+} shows the reduction of $Fe(TEA)^{3+}$ to $Fe(TEA)^{2+}$ starting at ~ -0.95 $V_{Ag/AgCl}$, then becoming mass-transport-limited at ~ -1.15 $V_{Ag/AgCl}$. The green LSV was run in the standard $Co_xFe_{3-x}O_4$ deposition solution containing both Co^{2+} and Fe^{3+}. It overlaps with the red LSV in the potential range of -0.95 to -1.03 $V_{Ag/AgCl}$, which indicates that in this potential range the cathodic current arises entirely from the reduction of $Fe(TEA)^{3+}$ to $Fe(TEA)^{2+}$. By comparing these four LSVs, the potential window for $Co_xFe_{3-x}O_4$ deposition is determined to lie between -0.95 and -1.03 $V_{Ag/AgCl}$. From the red LSV, the concentration of the $Fe^{3+}$and Fe^{2+} at the electrode surface can be calculated using eqs 3 and 4, where i is the measured current at a given potential, $i_{l,c}$ is the limiting cathodic

$$\frac{i}{i_{l,c}} = \frac{C_{Fe(II)}(surface)}{C_{Fe(III)}(bulk)} \tag{3}$$

$$C_{Fe(III)}(surface)+C_{Fe(II)}(surface)=C_{Fe(III)}(bulk) \tag{4}$$

current, $C_{Fe(III)}$(bulk) is the bulk concentration of Fe^{3+} in the solution, and $C_{Fe(III)}$(surface) and $C_{Fe(II)}$(surface) are the Fe^{3+} and Fe^{2+} concentrations at the electrode surface, respectively. The calculated surface concentrations of Fe^{3+}, Fe^{2+} and Co^{2+} are shown in Figure 1b. Because the Co^{2+} is electrochemically inactive at potentials more positive than -1.03 $V_{Ag/AgCl}$, so the concentration of Co^{2+} at the electrode surface remains constant, shown as the blue horizontal line in Figure 1b. At low overpotential, the surface concentration of Fe^{2+} is nearly equal to zero, whereas at high overpotential, where the mass transport limit is reached, the surface concentration of Fe^{2+} is approximately equal

to the bulk concentration of Fe^{3+} (50 mM). For the $Co_xFe_{3-x}O_4$ films deposited at any applied potential in the deposition window (between the two green dashed lines in Figure 1b), if we assume the Fe^{3+} in the $Co_xFe_{3-x}O_4$ is always stoichiometric (since there are no trivalent ion competing with it), then the Co^{2+}:Fe^{2+} ratio in the $Co_xFe_{3-x}O_4$ lattices should be controlled by their concentration ratio at the electrode surface, similar to what was shown for zinc ferrite electrodeposition.[8] Therefore, the Co:Fe ratio in the $Co_xFe_{3-x}O_4$ films is tunable by varying the deposition potential.

The morphologies and the atomic Co:Fe ratios of the $Co_xFe_{3-x}O_4$ films deposited at -0.95, -0.97, -0.99, -1.01 and -1.03 $V_{Ag/AgCl}$ on Au-sputtered glass were measured by a FE-SEM equipped with EDS system. The SEM images in Figure S1 (see the Supporting Information) show that there is no significant morphological difference between these films, as they all show pyramidal microstructures on the top surface. The film deposited at -1.03 $V_{Ag/AgCl}$ is slightly smoother. The dependence of the EDS-measured atomic Co concentrations on the deposition potential is shown in Figure 2 (red squares). The result indicates that the Co:Fe ratio in the $Co_xFe_{3-x}O_4$ films varies with the deposition potential. More Co^{2+} ions are substituted into the film at less negative potentials, which is consistent with the proposed mechanism (eqs 3 and 4). As the deposition potential goes to more negative values, more Fe^{3+} ions are reduced to Fe^{2+}, resulting in a decrease of the Co^{2+}:Fe^{2+} ratio at the electrode surface. Thus, Co composition is lower in the films deposited at more negative potentials. By assuming that the Co^{2+}:Fe^{2+} ratio in a $Co_xFe_{3-x}O_4$ film is equal to the Co^{2+}:Fe^{2+} ratio at the electrode surface, we can calculate the atomic Co^{2+} concentration in the $Co_xFe_{3-x}O_4$ film deposited at any potential based on the Co^{2+} and Fe^{2+} concentration profiles in Figure 1b. The black curve in Figure 2 shows the

calculated atomic Co^{2+} concentration as a function of the deposition potential. The calculated and measured Co content of the films varying in the deposition potential share the same trend, however the calculated content is higher than the measured one. This suggests that the Co^{2+}:Fe^{2+} ratio in the $Co_xFe_{3-x}O_4$ film is proportional, rather than equal, to the Co^{2+}:Fe^{2+} ratio at the electrode surface. This could be due to a slow kinetic reaction rate of Co^{2+} substitution, as the deviation between the Co content in the film and at the electrode surface is even larger when the growth rate of the film is faster (shown in Figure 7) at more negative potentials. The green dashed line in Figure 2 shows the atomic Co^{2+} concentration in stoichiometric cobalt ferrite (~33.3%). Theoretically, stoichiometric $CoFe_2O_4$ could be deposited by applying a potential positive enough (where almost no Fe^{3+} is reduced to Fe^{2+}), although nucleation might become a problem under that condition.

The effect of the Co composition on the structure of the $Co_xFe_{3-x}O_4$ films is investigated by using XRD and Raman spectroscopy. The θ-2θ scans of the $Co_xFe_{3-x}O_4$ films deposited at different potentials are shown in Figure S2 (in the Supporting Information). They all match with the X-ray pattern of fcc-$CoFe_2O_4$ except for slight peak shifting, which is not easily seen before careful analysis. The lattice parameters of the $Co_xFe_{3-x}O_4$ films are estimated using Nelson-Riley function plots (see the Supporting Information, Figure S3). The dependence of the lattice parameters on the deposition potential is shown in Figure 3 (the black squares). It increases as the deposition potential becomes more positive, as more Co^{2+} is substituted into the film. This result is in agreement with several other papers.[43,44] However, illustrated in Figure 3, the measured lattice parameters of the $Co_xFe_{3-x}O_4$ film are larger than either the lattice parameter of

bulk Fe_3O_4 (0.8396 nm, red dashed line) or $CoFe_2O_4$ (0.8392 nm, blue dashed line). The change of the film lattice parameter is not consistent with the Vegard's law. These divergences could be due to non-stoichiometric O contents in the films or the abnormal Co^{2+} distribution in both tetrahedral and octahedral sites, or both, compared to bulk inverse spinel cobalt ferrite.[44-46]

The concept that Co ions substitute Fe ions in the lattices is further supported by comparing the Raman spectra of the $Co_xFe_{3-x}O_4$ and Fe_3O_4 films as shown in Figure 3b. The Fe_3O_4 film was electrodeposited at -1.065 $V_{Ag/AgCl}$ from the Fe^{3+}-TEA-NaOH solution and is close to stoichiometric Fe_3O_4.[8] $Co_xFe_{3-x}O_4$ films were deposited at the different potentials as labeled in Figure 3b. The Raman spectrum of the Fe_3O_4 film (black curve) at room-temperature shows three Raman shift peaks at about 304, 537, and 668 cm^{-1} in the range of 200—1000 cm^{-1} as reported by other research groups.[47-50] For the spectra of the $Co_xFe_{3-x}O_4$ films, two fingerprint peaks of cobalt ferrite appear at about 466 and 626 cm^{-1}. Their intensities increase as the Co content increases. In addition, the Raman shift peaks of Fe_3O_4 at ~668 cm^{-1} slightly shift to larger wavelength as Co ions are substituted into the film. All the spectra of the $Co_xFe_{3-x}O_4$ films, especially the one of the film deposited at -0.95 $V_{Ag/AgCl}$, match well with the Raman spectra of cobalt ferrite reported by other investigators.[49,51] The differences between the Raman spectra of Fe_3O_4 and the $Co_xFe_{3-x}O_4$ films indicate an effective substitution of Fe by Co in the $Co_xFe_{3-x}O_4$ films.[49]

In addition to the structures, the electric properties of the $Co_xFe_{3-x}O_4$ films are also related to the amount of Co^{2+} substituted in the film. The resistivity of the different $Co_xFe_{3-x}O_4$ films was measured by using a four-point probe measurement. The resistivity

as a function of the x value in the $Co_xFe_{3-x}O_4$ is shown in Figure 4. It is clear that as more Co^{2+} is substituted into the film, the resistivity of the film increases exponentially. This observed trend of the resistivity is consistent with the fact that bulk Fe_3O_4 is a conductor whereas bulk $CoFe_2O_4$ is an insulator. This also shows that from one deposition bath, we can easily tune the resistivity of the $Co_xFe_{3-x}O_4$ film by controlling the deposition potential.

Epitaxial $Co_xFe_{3-x}O_4$ films can also be electrodeposited onto Au single crystals. The X-ray θ-2θ scan and the pole figure of the $Co_xFe_{3-x}O_4$ film deposited on a Au(111) single crystal at -1.03 $V_{Ag/AgCl}$ are shown in Figure 5a-b. The film shows a [111] out-of-plane orientation. Of all the {111} family peaks, the intensity of the (333) peak is much greater than the other peaks. This is due to the presence of <511> orientations, a d-spacing of {511} planes is the same as {333} planes in cubic structure. The observed <511> orientations are the result of the twinning on {111} planes.[52] The (311) pole figure of the $Co_xFe_{3-x}O_4$ film deposited on Au(111) shows a spot pattern, which indicates the film is not only out-of-plane oriented, but also in-plane oriented. That is, the $Co_xFe_{3-x}O_4$ film is epitaxial. By comparing the $Co_xFe_{3-x}O_4$ (311) pole figure with the $Co_xFe_{3-x}O_4$ (111) and (511) stereographic projections probing (311) type reflections, the spots at the tilt angles, χ, of 9.5°, 41.0°, 66.0°, and 86.7° are due to [511] orientations. The spots at χ = 29.5°, 58.5°, and 80° are the overlapped reflections from [111] and [511] orientations. The number of (511) domains is determined using the reflections at χ = 9.5°, since a single domain of (511) has only one spot at this χ. So, 6 domains of [511] orientation are present: $Co_xFe_{3-x}O_4[511](01\bar{1})//Au[111](0\bar{1}1)$, $Co_xFe_{3-x}O_4[511](0\bar{1}1)//Au[111](0\bar{1}1)$, $Co_xFe_{3-x}O_4[511](\bar{1}41)//Au[111](0\bar{1}1)$, $Co_xFe_{3-x}O_4[511](1\bar{4}\bar{1})//Au[111](0\bar{1}1)$, Co_xFe_{3-}

$_xO_4$[511]($\bar{1}$14)//Au[111](0$\bar{1}$1), $Co_xFe_{3-x}O_4$[511](1$\bar{1}\bar{4}$)//Au[111](0$\bar{1}$1). The number of (111) domain(s) could be 1 or 2 based on this pole figure and it is not easy to determine because all the reflections from [111] orientation are overlapped with those from [511] orientations. However, considering this $Co_xFe_{3-x}O_4$ has very similar crystal structure to the Fe_3O_4 we deposited on Au(111) in previous work,[53] it is more likely that it has two antiparalleled domains of [111] orientation: $Co_xFe_{3-x}O_4$[111](01$\bar{1}$)//Au[111](0$\bar{1}$1) and $Co_xFe_{3-x}O_4$[111](0$\bar{1}$1)//Au[111](0$\bar{1}$1).

Superlattices in $Co_xFe_{3-x}O_4$ system were electrodeposited onto Au(111) single crystals by pulsing the potential between -0.95 and -1.03 $V_{Ag/AgCl}$. The bilayer thickness (modulation wavelength of the superlattice) can be controlled by the dwell time at each pulsed potential. The overall thickness of the superlattice is determined by the product of the modulation wavelength and number of bilayers (same as the number of pulsed potential cycles). Three $Co_xFe_{3-x}O_4$ superlattices (#1 to #3) with different modulation wavelengths were deposited. The dwell time of each pulsed potential and the numbers of bilayers of these superlattices are listed in Table 1. The X-ray θ-2θ patterns of the $Co_xFe_{3-x}O_4$ superlattices are almost the same as that of the epitaxial film. But the $Co_xFe_{3-x}O_4$ superlattices manifest themselves by showing satellite peaks around the (333) Bragg peak in the X-ray θ-2θ patterns (Figure 6) due to the superperiodicity.[8,54-56] Based on the position of the satellite peaks, the modulation wavelength of each superlattice can be calculated according to eq 5,[54] where the λ is the wavelength of the X-ray source (CuKα1

$$\Lambda = \frac{\lambda(L_1 - L_2)}{2(\sin\theta_1 - \sin\theta_2)} \qquad \textbf{(5)}$$

= 0.15401 nm), L is the order of the satellite, and θ is the diffraction angle of satellite L. The modulation wavelengths of the $Co_xFe_{3-x}O_4$ superlattices #1 to #3 were calculated to be about 37, 22, and 11 nm, respectively.

The modulation wavelengths of these three $Co_xFe_{3-x}O_4$ superlattices can also be determined by using an electrochemical quartz crystal microbalance (EQCM). The current/time (red) and thickness/time transients (blue) of 5 pulsed potential cycles for the electrodeposition of the $Co_xFe_{3-x}O_4$ superlattices #1 to #3 are shown in Figure 7a-c in order. In this study, we assume that the density of $Co_xFe_{3-x}O_4$ is equal to that of bulk $CoFe_2O_4$ (5.29 g/cm^3). It can be seen that compared to -0.95 $V_{Ag/AgCl}$, -1.03 $V_{Ag/AgCl}$ results in a higher cathodic current density and growth rate. The thickness of each individual layer of the bilayers in the superlattices is estimated based on the thickness/time transients (blue lines) in the plots. The bilayer thicknesses (modulation wavelength) of the three $Co_xFe_{3-x}O_4$ superlattices are determined to be about 35, 24, and 12 nm according to the EQCM results. They agree very well with the calculated results based on the XRD patterns (in Figure 6).

The resistance switching studies performed on the $Co_xFe_{3-x}O_4$ superlattices #1 and two individual epitaxial films at 77 K are shown in Figure 8a-c. The two epitaxial $Co_xFe_{3-x}O_4$ films were deposited at -0.95 and -1.03 $V_{Ag/AgCl}$. There is no significant difference between the *iV* curves of the $Co_xFe_{3-x}O_4$ superlattices with different modulation wavelengths. However, the *iV* curves of the individual film and the superlattices are different. All the *iV* curves show a similar non-ohmic shape and low-to-high resistance switching. This is possibly due to field-driven oxidation of Fe^{2+} to Fe^{3+} in the film, which forms the more resistive γ-Fe_2O_3 at the interface between the metallic anode electrode

and the film.[8,57] Following the low-to-high resistance switching, the *iV* curves of the superlattice (Figure 8a) and the -0.95 $V_{Ag/AgCl}$ $Co_xFe_{3-x}O_4$ film (Figure 8b) all show oscillations of the bias voltage, accompanied by a negative differential resistance (NDR) feature. The resistances of the films abruptly decrease after the oscillation, as shown by the continuous NDR feature for the superlattice and the near-vertical current increase to 2 A (instrument limit) for the -0.95 $V_{Ag/AgCl}$ film. This high-to-low resistance switching is due to the insulator-to-metal phase transition (Verwey transition).[8,58,59] The *iV* curve of the -1.03 $V_{Ag/AgCl}$ film only shows the low-to-high resistance switching in our measured current range. Although the *iV* curves of the superlattice and the -0.95 $V_{Ag/AgCl}$ film have similar behaviors, it should be noted that the phase transition of the superlattice happens at lower current, which is probably due to the nanolayering of the superlattice. The phase transition in the superlattice might be facilitated by residual strain in the superlattice.[8]

The magnetic properties of $Co_xFe_{3-x}O_4$ films are also affected by the chemical composition. In order to study how coercivity (H_C) and saturation magnetization (M_S) of the $Co_xFe_{3-x}O_4$ are related to its composition, VSM measurements were performed for the films deposited at different potentials on Au sputtered glass substrates. Figure 9a shows the in- and out-of-plane hysteresis loops measured at 300 K for 1±0.1 μm thick $Co_xFe_{3-x}O_4$ films deposited at -0.97 and -1.03 $V_{Ag/AgCl}$ and the Fe_3O_4 film deposited at -1.065 $V_{Ag/AgCl}$[8]. The easy axis of magnetization lies in the film plane, displayed by a square shape of the in-plane hysteresis loops. The H_C of the $Co_xFe_{3-x}O_4$ film increases with Co^{2+} content, and is significantly higher than that of the magnetite film as shown in the inset of Figure 9a. Note that all films, including magnetite, have columnar structure, (111) fiber texture, similar grain size and roughness, comparable strain, and very close lattice

parameters (see Figure 3).[8,42,53] Hence, the difference in H_C of the films with the same thickness can be assigned to the compositional variations. The M_S of the films were also calculated based on their hysteresis loops. The M_S of $Co_xFe_{3-x}O_4$ as a function of the Co composition is shown in Figure 9b. The M_S increases as cobalt composition decreases, and the M_S of all investigated $Co_xFe_{3-x}O_4$ films are lower than that of the electrodeposited Fe_3O_4 (M_S=86.6 emu g^{-1}), indicated by a green arrow in Figure 9b. The measured M_S of the electrodeposited Fe_3O_4 (86.6 emu g^{-1}) is lower than that of bulk material (93.2 emu g^{-1}).[60] This could be due to a presence of anti-phase boundaries (APB's) in our electrodeposited Fe_3O_4 film,[42,61] which causes a reduction of M_S.[62] This could also be due to an overestimation of the mass of the film, as we assume our film is as dense as bulk Fe_3O_4. The M_S of our electrodeposited $Co_xFe_{3-x}O_4$ films agree well with the reported M_S for bulk $CoFe_2O_4$ within the range of 67.9 – 74.5 emu g^{-1} (patterned area in Figure 9b).[27] Considering the lower Co content in our electrodeposited $Co_xFe_{3-x}O_4$ films compared to stoichiometric $CoFe_2O_4$, one would expect the M_S of our films to be higher. However, it has been reported that thin cobalt ferrite films exhibit significantly lower magnetization compared to the bulk material.[27,62] This could also be the case of the APB's effect, which will be discussed in following sections. The increase of H_C and reduction of M_S with increasing Co content is expected and in agreement with previously published results.[26,27,60] Cobalt ferrite characterizes large magnetocrystalline anisotropy (first-order cubic magnetocrystalline anisotropy term of stoichiometric $CoFe_2O_4$, K_1=290 kJ m^{-3}) compared to magnetite (K_1=-11 kJ m^{-3}),[60] even for very non-stoichiometric compositions.[63] A large increase of the magnetocrystalline anisotropy due to doping magnetite with cobalt leads to enhanced H_C and reduced M_S.

The composition of the $Co_xFe_{3-x}O_4$ also affects the temperature of metal-to-insulator transition (MIT, also called Verwey transition). Figure 10 shows the resistance as a function of temperature for $Co_xFe_{3-x}O_4$ films deposited at -0.95 and -1.03 $V_{Ag/AgCl}$, and the $Co_xFe_{3-x}O_4$ superlattice #1 on Au(111) single-crystal substrates. It can be seen that the -1.03 $V_{Ag/AgCl}$ film, with a composition close to magnetite, undergoes a transition at a temperature of about 80 K (inset of Figure 10). However, no apparent Verwey transition is noticed in the -0.95 $V_{Ag/AgCl}$ film. This is in agreement with the results published by other researchers that magnetite has a Verwey transition at about 120 K while cobalt ferrite has no obvious transition temperature.[15,27,58,64] On the other hand, the $Co_xFe_{3-x}O_4$ superlattice shows a broad transition at a higher temperature (~ 100 K).

It is known that bilayers of $CoFe_2O_4/Fe_3O_4$[64,65] and (Mn, Zn)$Fe_2O_4/CoFe_2O_4$[66] exhibit exchange coupling between individual layers, which is manifested by two-step magnetization loops. This could also be the case for electrodeposited $Co_xFe_{3-x}O_4$ superlattices. Figure 11a shows the in-plane hysteresis loops measured on $Co_xFe_{3-x}O_4$ superlattice #1 on Au(111) substrate at different temperatures. The ones measured above the Verwey transition temperature of 100 K show only single-step loops, indicating that the superlattice behaves as a single-phase material above the Verwey transition temperature. Weak signatures of two-step hysteresis loops (marked by the arrows in the inset of Figure 11a) are observed for those measured at temperatures below 100 K. The exchange coupling between individual layers in the superlattice is not strong because the two individual layers in the superlattice have relatively similar H_C and magnetocrystalline anisotropies.[63] Figure 11b shows the out-of-plane hysteresis loops measured for superlattice #1 at 77 and 300 K. These two temperatures are intentionally selected in

order to show the differences in the shape of the out-of-plane hysteresis loops above and below the Verwey transition of the $Co_xFe_{3-x}O_4$ superlattice. For the loop measured at 300 K, the feature in the low field region can be explained in two different ways. It could simply be the misalignment of the sample on the Au single-crystal substrates (it is much easier to align the samples on Au sputtered glass substrates using a different sample holder, Figure 9a), which causes the appearance of the in-plane magnetization in the out-of-plane measurements. It could also be caused by a complex switching of the magnetization due to the nano-scale thickness of the individual layers in the superlattice. In this case, the magnetization would tilt from the out-of-plane direction into the film plane, rotate in the film plane, and then tilt again towards the out-of-plane with an opposite direction to the initial magnetization state. The loop measured at 77 K is much richer in features. Besides a higher H_C due to the increased magnetocrystalline anisotropy, the loop shows two inflection points (indicated by the arrows in Figure 11b) at fields of about ± 3 kOe. This could be an indication of the exchange coupling between individual layers in the superlattice, as the shape of the loop is not just a simple superposition of the two loops of the individual films (inset of Figure 11b).

The $Co_xFe_{3-x}O_4$ films and superlattices were further analyzed by magneto-transport measurements. The magnetoresistance (MR) of the -1.03 $V_{Ag/AgCl}$ $Co_xFe_{3-x}O_4$ film measured in and out of the film plane at 300 K is shown in Figure 12a-b as an example, since all the MR curves of the $Co_xFe_{3-x}O_4$ films and superlattices are similar. The MR is determined by eq 6, where R_H is the resistance in magnetic field H and R_0 is

$$MR = \frac{R_H - R_0}{R_0} \times 100\% \quad (6)$$

the resistance in zero field. It is apparent that this $Co_xFe_{3-x}O_4$ film exhibits MR at 300 K regardless of the orientation of the film surface relative to the magnetic field. The in-plane curve (Figure 12a) shows the so-called 'butterfly' effect at low magnetic fields, which indicates that the low field MR shape could be caused by a spin-polarized tunneling across the grain boundaries or spin-disordered scattering at the grain boundaries.[67] If it is due to the former reason, the square of magnetization, $C(M/M_S)^2$, should fit to the in-plane MR curve. However, these do not fit to each other as shown in Figure 12a. Hence, we attribute this 'butterfly' effect to spin-disordered scattering at the grain boundaries.[67] At high magnetic field, the magnetization in the VSM measurement saturates (red curve in the inset of Figure 12a), however, an almost linear increase of the MR is observed in magneto-transport measurements. This can be explained by the spin-polarized transport across the APB's.[68] Because the volume fraction of the APB's in the film is exceedingly small, their effect is hard to see in the global magnetization measured with VSM mode. The out-of-plane MR in Figure 12b has a quadratic shape at low fields followed by a linear dependence in the magnetic field range of about 2.5 to 5 kOe. This is in good agreement with the modeling results reported by Eerenstein *et al.* and is probably due to spin-polarized transport across atomically sharp antiferromagnetically coupled boundaries.[68] Similar results were also seen for sputtered Co-doped Fe_3O_4 films.[15] However, in our case, a deviation of the MR from linearity at high fields is observed. As pointed out by Tripathy *et al.*, this might be because the model proposed by Eerenstein *et*

al. considers only uniaxial anisotropy, neglecting magnetocrystalline anisotropy, which is not negligible in the $Co_xFe_{3-x}O_4$.

Magneto-transport measurements were also conducted at lower temperature (77 K). The low temperature in-plane MR curves, irrespective of the film composition, have a very similar shape to the curve measured at 300 K (Figure 12a), except that the maxima in the curves corresponding to H_C appear at higher magnetic fields (not shown in the paper). Figure 13a show the 77 K out-of-plane MR curves (lines) and the derivative of magnetization (dM/dH, points) curves of the -1.03 $V_{Ag/AgCl}$ $Co_xFe_{3-x}O_4$ individual film. Instead of a single maximum observed in the MR curve measured at 300 K, the 77 K MR curve shows two maxima corresponding to the H_C of the film, as illustrated by dM/dH curves (points in Figure 13a). On the other hand, the out-of-plane MR curves of superlattice #1 at 77 K (Figure 13b) are much richer in features. Two local maxima and a minimum are observed in each scan direction. The minimum corresponds to the H_C of the superlattice (the sharp maximum in the dM/dH curve in Figure 13b) and the maxima corresponds to the inflection points previously shown in its hysteresis loop (Figure 11b). The shapes of the hysteresis loop and MR curve at low temperature indicate a complex magnetization switching mechanism in the superlattice, including exchange coupling between the two individual layers. In this case, the two layers in the superlattice switch independently in certain magnetic fields with one of the two layers acting as a pinning layer. However, the exact mechanism requires further investigations.

Angular-dependent MR of the $Co_xFe_{3-x}O_4$ individual films and superlattices were measured at 20 kOe magnetic field (all films are saturated at this field) as shown in Figure 14a-c. The MR shown in the Figure 14 is normalized by using eq 7, where R_Φ is

$$R_{Normalized} = \frac{R_{\Phi} - R_0}{R_0} \quad (7)$$

the resistance in magnetic field (20 kOe) applied at the angle of Φ relative to the in-plane direction of the film and R_0 is the MR in the same magnetic field applied along the in-plane direction of the film. According to Figure 14, all the films, irrespective of the composition, show angular-dependence of MR in applied magnetic field at some of the measured temperatures. For the $Co_xFe_{3-x}O_4$ film deposited at -0.95 $V_{Ag/AgCl}$ (in Figure 14a), minimum MR appears at the tilt angle of 90°, and it drops as the temperature decreases. Considering that the film is in magnetic saturation (except for the APB's), this is due to the increase of the magnetocrystalline anisotropy constant, which increases inversely proportional to the temperature. In the case of the film deposited at -1.03 $V_{Ag/AgCl}$ (Figure 14b), there was no angular dependence of the MR observed at temperatures above 120 K. The curve measured at 120 K shows two minima at the tilt angles of about 60 and 120°. This temperature is relatively close to the Verwey transition temperature in this film. Therefore, the change of the shape of the curve can be assigned, in analogy to magnetite,[67,69] to a rotation of the easy magnetization axis in the film, from <111> to <100> as the temperature drops across the Verwey transition. As the temperature further decreases, the magnetocrystalline anisotropy dominates the shape of the curve, similar to the situation for -1.03 $V_{Ag/AgCl}$ film except that the minimum is broader. The $Co_xFe_{3-x}O_4$ Superlattice shows different behaviors compared to individual layers in the angular-dependent MR measurements (Figure 14c). Instead of showing minimum MR at certain tilt angles as in the case of the individual films, the superlattice

shows maximum MR at about 60 and 120° in the curves measured at 120 and 77 K. The inverse shape of the angular-dependent MR curves obtained for superlattice further suggests that the superlattice is not a simple superposition of two individual layers. It has more complex magnetization mechanism, which is already indicated in the MR and magnetization measurements. Besides the magnetocrystalline anisotropy, other factors have to be considered in the case of superlattices, such as shape anisotropy due to the nano-scale thickness of the individual layer and exchange coupling between the alternating layers in the superlattices. Although further investigations would be needed to fully understand the mechanism, the magnetic and magneto-transport measurements of the $Co_xFe_{3-x}O_4$ individual films and superlattices do show the potential applications in mimicking the magneto-reception systems in a homing pigeon[40] and magnetotactic bacteria[41].

CONCLUSIONS

Crystalline $Co_xFe_{3-x}O_4$ individual films with different Co:Fe ratios and $Co_xFe_{3-x}O_4$ superlattices were directly electrodeposited without any post treatment. The chemical compositions of the $Co_xFe_{3-x}O_4$ films along with their structural, electric and magnetic properties (such as M_S and H_C) can be easily tuned by controlling the deposition potential. The electrodeposition of $Co_xFe_{3-x}O_4$ follows the electrochemical-chemical mechanism. Besides Co and Zn,[8] this method should be quite general for substituting other ions (such as Mn, Ni) into Fe_3O_4. The electrodeposited $Co_xFe_{3-x}O_4$ films and superlattices show resistance switching behavior and a NDR feature (due to a MIT transition) in measurements at 77 K. The nanolayered structure of the $Co_xFe_{3-x}O_4$

superlattices facilitates the phase transition, as the NDR feature appears at lower current in perpendicular transport measurements (*iV* curves) compared to the individual films. According to the *iV* curves of the electrodeposited $Co_xFe_{3-x}O_4$, multiple resistance states can be accessed by varying the applied bias. This shows that the $Co_xFe_{3-x}O_4$, especially the $Co_xFe_{3-x}O_4$ superlattices, can be potentially used for multibit logic devices. $Co_xFe_{3-x}O_4$ superlattices also show more complex magnetization switching behavior in the magnetic and magnetotransport measurements. This could be due to exchange coupling between the layers with different chemical compositions and the shape anisotropy because of the nanoscale thickness of the alternating layers in the superlattices. All the $Co_xFe_{3-x}O_4$ individual films and superlattices show angular-dependent MR. This shows that $Co_xFe_{3-x}O_4$ has a potential application as a magnetoreceptor, mimicking the Fe_3O_4-based magnetoreception systems in animals such as homing pigeons and magnetotactic bacteria. Although further investigations are required, the angular-dependent MR measurements could be helpful for understanding the basic physical principles behind the navigation ability of the animals in nature.

ACCOCIATED CONTENT

Supporting Information. SEM images, XRD patterns, hysteresis loops, magnetic and magneto-transport measurements. This material is available free of charge via the Internet at http://pubs.acs.org.

AUTHOR INFORMATION

Corresponding Author

* E-mail: jswitzer@mst.edu.

ACKNOWLEGEMENTS

This work was supported by the U.S. Department of Energy, Office of Basic Energy Sciences, Division of Materials Sciences and Engineering, under Grant No. DE-FG02-08ER46518 (electrodeposition, chemical and structure characterization studies), and the National Science Foundation under Grant No. DMR-1104801 (electrical transport, resistance switching and magnetic properties studies).

REFERENCES

(1) Prinz, G. A. *Science* **1998**, *282*, 1660.

(2) Wolf, S. A.; Awschalom, D. D.; Buhrman, R. A.; Daughton, J. M.; von Molnar, S.; Roukes, M. L.; Chtchelkanova, A. Y.; Treger, D. M. *Science* **2001**, *294*, 1488.

(3) Carey, M. J.; Maat, S.; Rice, P.; Farrow, R. F. C.; Marks, R. F.; Kellock, A.; Nguyen, P.; Gurney, B. A. *Appl. Phys. Lett.* **2002**, *81*, 1044.

(4) Lee, S.; Fursina, A.; Mayo, J. T.; Yavuz, C. T.; Colvin, V. L.; Sofin, R. G.; Shvets, I. V.; Natelson, D. *Nat. Mater.* **2008**, *7*, 130.

(5) Chapline, M. G.; Wang, S. X. *Phys. Rev. B* **2006**, 74, 014418/1.

(6) Gazeau, F.; Koralsztein, J. P.; Billat, V. *Arch. Physiol. Biochem.* **1997**, *105*, 583.

(7) Zheng, H.; Wang, J.; Lofland, S. E.; Ma, Z.; Mohaddes-Ardabili, L.; Zhao, T.; Salamanca-Riba, L.; Shinde, S. R.; Ogale, S. B.; Bai, F.; Viehland, D.; Jia, Y.; Schlom, D. G.; Wuttig, M.; Roytburd, A.; Ramesh, R. *Science* **2004**, *303*, 661.

(8) Switzer Jay, A.; Gudavarthy Rakesh, V.; Kulp Elizabeth, A.; Mu, G.; He, Z.; Wessel Andrew, J. *J. Am. Chem. Soc.* **2010**, *132*, 1258.

(9) Yanase, A.; Siratori, K. *J. Phys. Soc. Jpn.* **1984**, *53*, 312.

(10) Zhang, Z.; Satpathy, S. *Phys. Rev. B* **1991**, *44*, 13319.

(11) Lie, C. T.; Kuo, P. C.; Hsu, W.-C.; Chang, I. J.; Chen, J. W. *J. Magn. Magn. Mater.* **2002**, *239*, 160.

(12) Chou, C. Y.; Kuo, P. C.; Yao, Y. D.; Sun, A. C.; Chen, S. C.; Chang, I. J.; Chen, J. W. *IEEE Trans. Magn.* **2005**, *41*, 906.

(13) Ishikawa, M.; Tanaka, H.; Kawai, T. *Appl. Phys. Lett.* **2005**, *86*, 222504/1.

(14) Snoeck, E.; Gatel, C.; Serra, R.; BenAssayag, G.; Moussy, J. B.; Bataille, A. M.; Pannetier, M.; Gautier-Soyer, M. *Phys. Rev. B* **2006**, *73*, 104434/1.

(15) Tripathy, D.; Adeyeye, A. O.; Boothroyd, C. B.; Piramanayagam, S. N. *J. Appl. Phys.* **2007**, *101*, 013904/1.

(16) Takaobushi, J.; Tanaka, H.; Kawai, T.; Ueda, S.; Kim, J.-J.; Kobata, M.; Ikenaga, E.; Yabashi, M.; Kobayashi, K.; Nishino, Y.; Miwa, D.; Tamasaku, K.; Ishikawa, T. *Appl. Phys. Lett.* **2006**, *89*, 242507/1.

(17) Takaobushi, J.; Ishikawa, M.; Ueda, S.; Ikenaga, E.; Kim, J.-J.; Kobata, M.; Takeda, Y.; Saitoh, Y.; Yabashi, M.; Nishino, Y.; Miwa, D.; Tamasaku, K.; Ishikawa, T.; Satoh, I.; Tanaka, H.; Kobayashi, K.; Kawai, T. *Phys. Rev. B* **2007**, *76*, 205108/1.

(18) Hastings, J. M.; Corliss, L. M. *Phys. Rev.* **1956**, *102*, 1460.

(19) Lee, M.-S.; Kim, T.-Y.; Lee, C.-S.; Park, J.-C.; Kim, Y. I.; Kim, D. *J. Magn. Magn. Mater.* **2004**, *268*, 62.

(20) Franke, H.; Rosenberg, M. *J. Magn. Magn. Mater.* **1977**, *4*, 186.

(21) Hu, G.; Choi, J. H.; Eom, C. B.; Harris, V. G.; Suzuki, Y. *Phys. Rev. B* **2000**, *62*, R779.

(22) Sawatzky, G. A.; Van der Woude, F.; Morrish, A. H. *Phys. Rev.* **1969**, *187*, 747.

(23) Olsson, R. T.; Salazar-Alvarez, G.; Hedenqvist, M. S.; Gedde, U. W.; Lindberg, F.; Savage, S. J. *Chem. Mater.* **2005**, *17*, 5109.

(24) Liu, B. H.; Ding, J. *Appl. Phys. Lett.* **2006**, *88*, 042506/1.

(25) Tripathy, D.; Adeyeye, A. O.; Piramanayagam, S. N.; Mah, C. S.; Gao, X.; Wee, A. T. S. *Thin Solid Films* **2006**, *505*, 45.

(26) Salazar-Alvarez, G.; Olsson, R. T.; Sort, J.; Macedo, W. A. A.; Ardisson, J. D.; Baro, M. D.; Gedde, U. W.; Nogues, J. *Chem. Mater.* **2007**, *19*, 4957.

(27) Moyer, J. A.; Vaz, C. A. F.; Negusse, E.; Arena, D. A.; Henrich, V. E. *Phys. Rev. B* **2011**, *83*, 035121/1.

(28) Huang, W.; Zhu, J.; Zeng, H. Z.; Wei, X. H.; Zhang, Y.; Li, Y. R. *Appl. Phys. Lett.* **2006**, *89*, 262506/1.

(29) Schmidt, G.; Ferrand, D.; Molenkamp, L. W.; Filip, A. T.; van Wees, B. J. *Phys. Rev. B* **2000**, *62*, R4790.

(30) Coey, J. M. D.; Chien, C. L. *MRS Bull.* **2003**, *28*, 720.

(31) Antonov, V. N.; Harmon, B. N.; Yaresko, A. N. *Phys. Rev. B* **2003**, *67*, 024417/1.

(32) Lisfi, A.; Williams, C. M. *J. Appl. Phys.* **2003**, *93*, 8143.

(33) Huang, W.; Zhou, L. X.; Zeng, H. Z.; Wei, X. H.; Zhu, J.; Zhang, Y.; Li, Y. R. *J. Cryst. Growth* **2007**, *300*, 426.

(34) Chong, Y. T.; Yau, E. M. Y.; Nielsch, K.; Bachmann, J. *Chem. Mater.* **2010**, *22*, 6506.

(35) Sartale, S. D.; Lokhande, C. D. *Ceram. Int.* **2002**, *28*, 467.

(36) Carlier, D.; Ansermet, J.-P. *J. Electrochem. Soc.* **2006**, *153*, C277.

(37) Switzer, J. A.; Hung, C. J.; Breyfogle, B. E.; Shumsky, M. G.; Van Leeuwen, R.; Golden, T. D. *Science* **1994**, *264*, 1573.

(38) Switzer, J. A.; Shane, M. J.; Phillips, R. J. *Science* **1990**, *247*, 444.

(39) Kothari, H. M.; Vertegel, A. A.; Bohannan, E. W.; Switzer, J. A. *Chem. Mater.* **2002**, *14*, 2750.

(40) Solov'yov Ilia, A.; Greiner, W. *Biophys. J.* **2007**, *93*, 1493.

(41) Johnsen, S.; Lohmann, K. J. *Phys. Today* **2008**, *61*, 29.

(42) Kothari, H. M.; Kulp, E. A.; Limmer, S. J.; Poizot, P.; Bohannan, E. W.; Switzer, J. A. *J. Mater. Res.* **2006**, *21*, 293.

(43) Nakagomi, F.; da Silva, S. W.; Garg, V. K.; Oliveira, A. C.; Morais, P. C.; Franco Junior, A.; Lima, E. C. D. *J. Appl. Phys.* **2007**, *101*, 09M514/1.

(44) Sileo, E. E.; Garcia Rodenas, L.; Paiva-Santos, C. O.; Stephens, P. W.; Morando, P. J.; Blesa, M. A. *J. Solid State Chem.* **2006**, *179*, 2237.

(45) Hou, Y. H.; Zhao, Y. J.; Liu, Z. W.; Yu, H. Y.; Zhong, X. C.; Qiu, W. Q.; Zeng, D. C.; Wen, L. S. *J. Phys. D* **2010**, *43*, 445003/1.

(46) Li, X.-H.; Xu, C.-L.; Han, X.-H.; Qiao, L.; Wang, T.; Li, F.-S. *Nanoscale Res. Lett.* **2010**, *5*, 1039.

(47) Arisi, E.; Bergenti, I.; Cavallini, M.; Riminucci, A.; Ruani, G.; Dediu, V.; Ghidini, M.; Pernechele, C.; Solzi, M. *Appl. Phys. Lett.* **2008**, *93*, 113305/1.

(48) Shebanova, O. N.; Lazor, P. *J. Solid State Chem.* **2003**, *174*, 424.

(49) Naidek, K. P.; Bianconi, F.; Rizuti da Rocha, T. C.; Zanchet, D.; Bonacin, J. A.; Novak, M. A.; Vaz, M. d. G. F.; Winnischofer, H. *J. Colloid Interf. Sci.* **2011**, *358*, 39.

(50) Li, J.-M.; Huan, A. C. H.; Wang, L.; Du, Y.-W.; Feng, D. *Phys. Rev. B* **2000**, *61*, 6876.

(51) Wang, W. H.; Ren, X. *J. Cryst. Growth* **2006**, *289*, 605.

(52) Sorenson, T. A.; Morton, S. A.; Waddill, G. D.; Switzer, J. A. *J. Am. Chem. Soc.* **2002**, *124*, 7604.

(53) Kulp, E. A.; Kothari, H. M.; Limmer, S. J.; Yang, J.; Gudavarthy, R. V.; Bohannan, E. W.; Switzer, J. A. *Chem. Mater.* **2009**, *21*, 5022.

(54) Switzer, J. A.; Shane, M. J.; Phillips, R. J. *Science* **1990**, *247*, 444.

(55) Switzer, J. A.; Raffaelle, R. P.; Phillips, R. J.; Hung, C. J.; Golden, T. D. *Science* **1992**, *258*, 1918.

(56) Switzer, J. A.; Hung, C. J.; Breyfogle, B. E.; Shumsky, M. G.; Van Leeuwen, R.; Golden, T. D. *Science* **1994**, *264*, 1573.

(57) Odagawa, A.; Katoh, Y.; Kanzawa, Y.; Wei, Z.; Mikawa, T.; Muraoka, S.; Takagi, T. *Appl. Phys. Lett.* **2007**, *91*, 133503/1.

(58) Verwey, E. J. W. *Nature* **1939**, *144*, 327.

(59) Rooksby, H. P.; Willis, B. T. M. *Nature* **1953**, *172*, 1054.

(60) Coey, J. M. D. *Magnetism and Magnetic Materials*; Cambridge University Press: Cambridge, 2010.

(61) Gudavarthy, R. V.; Gorantla, S.; Mu, G.; Kulp, E. A.; Gemming, T.; Eckert, J.; Switzer, J. A. *Chem. Mater.* **2011**, *23*, 2017.

(62) Yanagihara, H.; Uwabo, K.; Minagawa, M.; Kita, E.; Hirota, N. *J. Appl. Phys.* **2011**, *109*, 07C122/1.

(63) Bozorth, R. M.; Tilden, E. F.; Williams, A. J. *Phys. Rev.* **1955**, *99*, 1788.

(64) Ramos, A. V.; Matzen, S.; Moussy, J.-B.; Ott, F.; Viret, M. *Phys. Rev. B* **2009**, *79*, 014401/1.

(65) Ziese, M.; Hoehne, R.; Bollero, A.; Semmelhack, H. C.; Esquinazi, P.; Zimmer, K. *Euro. Phys. J. B* **2005**, *45*, 223.

(66) Suzuki, Y.; van Dover, R. B.; Gyorgy, E. M.; Phillips, J. M.; Felder, R. J. *Phys. Rev. B* **1996**, *53*, 14016.

(67) Ziese, M.; Hohne, R.; Semmelhack, H. C.; Reckentin, H.; Hong, N. H.; Esquinazi, P. *Euro. Phys. J. B* **2002**, *28*, 415.

(68) Eerenstein, W.; Palstra, T. T. M.; Saxena, S. S.; Hibma, T. *Phys. Rev. Lett.* **2002**, *88*, 247204.

(69) Bollero, A.; Ziese, M.; Hoehne, R.; Semmelhack, H. C.; Koehler, U.; Setzer, A.; Esquinazi, P. *J. Magn. Magn. Mater.* **2004**, *285*, 279.

Table 1. Parameters used to deposit the three $Co_xFe_{3-x}O_4$ superlattices.

$Co_xFe_{3-x}O_4$ superlattices	Dwell Time (s)		# of Bilayers
	-1.03 V	-0.95 V	
#1	3	15	100
#2	2	10	200
#3	1	5	300

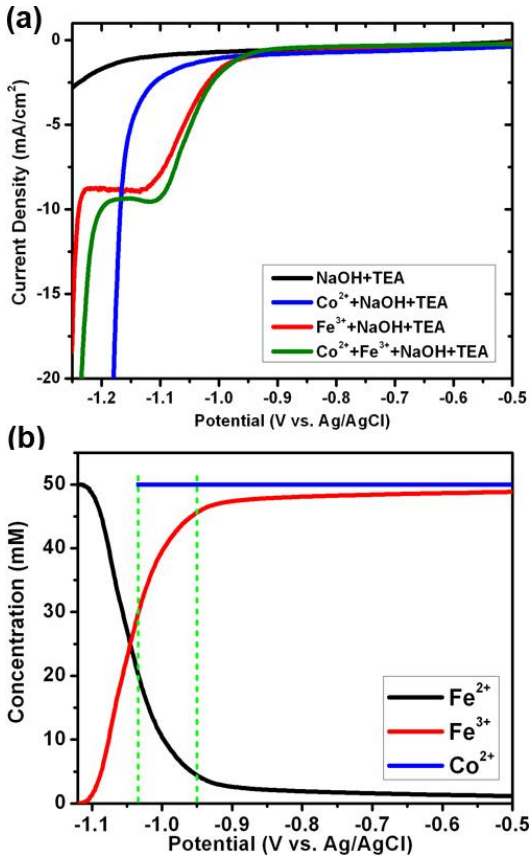

Figure 1. Electrochemistry of the $Co_xFe_{3-x}O_4$ deposition solution. (a) Linear sweep voltammograms of the NaOH-TEA solution (black), Fe^{3+}-TEA-NaOH solution (red), Co^{2+}-TEA-NaOH (blue) and Fe^{3+}-Co^{2+}-TEA-NaOH solution (green) at 80 ℃ scanned at 50 mV/s on a Au rotating-disk electrode at 100 rpm. All the solutions contain 2 M NaOH and 100 mM TEA. The concentrations of Fe^{3+} and Co^{2+} are 50 mM in the corresponding solutions. (b) The concentrations of Fe^{3+}, Fe^{2+}, and Co^{2+} at the electrode surface as a function of potential in the $Co_xFe_{3-x}O_4$ deposition solution. The two green dashed lines indicate the $Co_xFe_{3-x}O_4$ deposition window from -0.95 to -1.03 $V_{Ag/AgCl}$

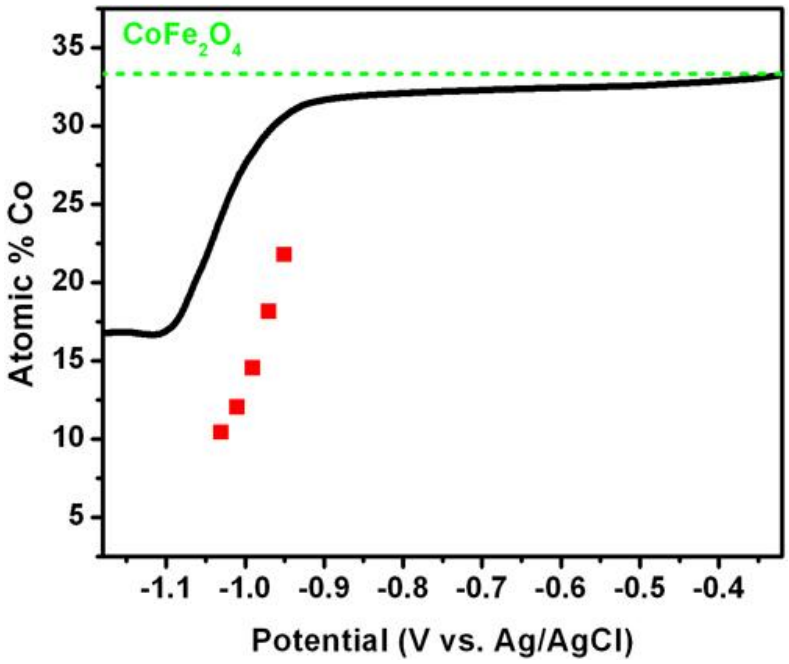

Figure 2. Comparison of the measured and calculated Co^{2+} compositions in $Co_xFe_{3-x}O_4$ films deposited at different potentials. The red squares show the compositions of Co^{2+} measured by EDS in the electrodeposited $Co_xFe_{3-x}O_4$ films. The black curve shows the calculated Co^{2+} composition in the $Co_xFe_{3-x}O_4$ films as a function of the deposition potential. The calculation is based on the assumption that Fe^{3+} is always stoichiometric in the $Co_xFe_{3-x}O_4$ film and the Co^{2+}:Fe^{2+} ratio in the $Co_xFe_{3-x}O_4$ film is equal to their ratio at the electrode surface. The green dashed line shows the theoretical atomic Co^{2+} ratio in stoichiometric cobalt ferrite.

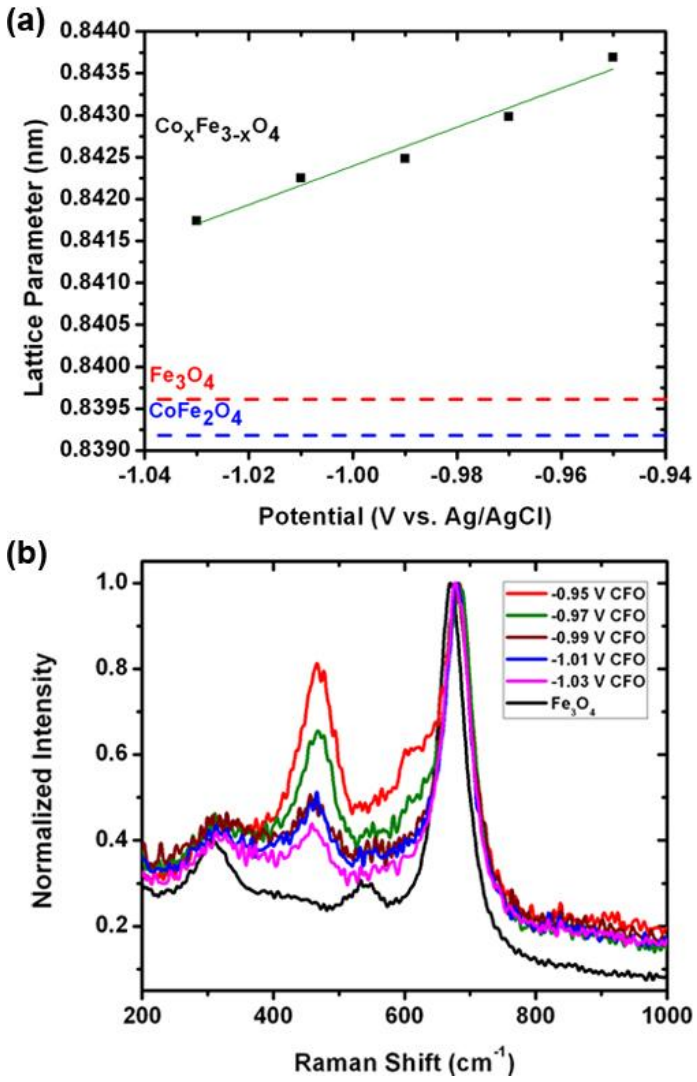

Figure 3. XRD and Raman characterization of the $Co_xFe_{3-x}O_4$ films deposited at different potentials. (a) The lattice parameter of the $Co_xFe_{3-x}O_4$ films as a function of deposition potential. The experimentally measured lattice parameters of the $Co_xFe_{3-x}O_4$ films deposited at different potentials are shown as black squares. The linear fit of them is shown as the green line. The red and blue dashed lines indicate the lattice parameters of stoichiometric bulk magnetite and cobalt ferrite. (b) Comparison of the Raman spectra of the $Co_xFe_{3-x}O_4$ and Fe_3O_4 films.

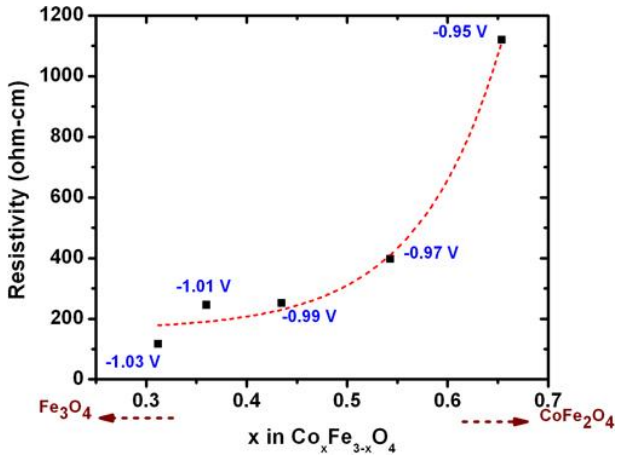

Figure 4. Resistivity as a function of the Co composition in the $Co_xFe_{3-x}O_4$ films. The black squares are the measured resistivity of the $Co_xFe_{3-x}O_4$ films deposited at different potentials as shown by the blue labels. The red dashed line is the exponentially fitted curve of the measured resistivity data. The x value in $Co_xFe_{3-x}O_4$ is calculated based on the Co:Fe ratio in the $Co_xFe_{3-x}O_4$ films measured by EDS.

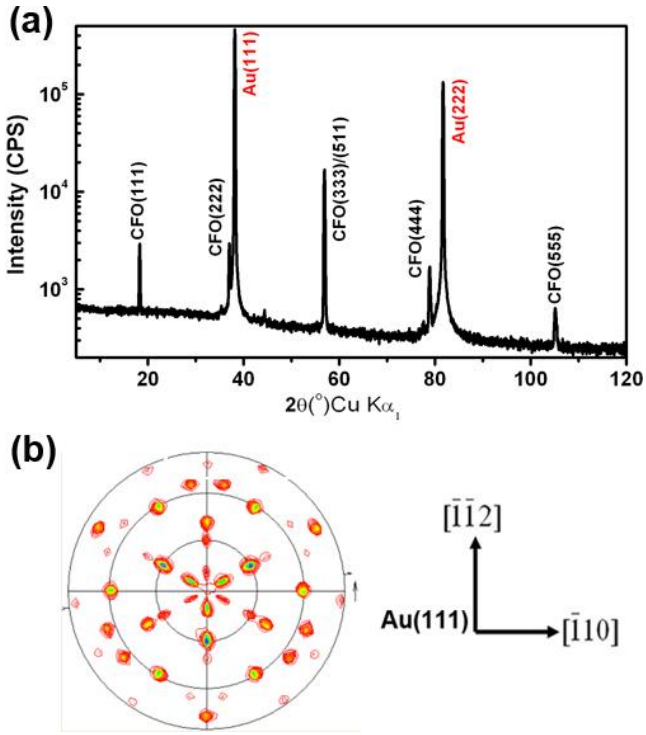

Figure 5. X-ray diffraction of a $Co_xFe_{3-x}O_4$ film electrodeposited at -1.03 $V_{Ag/AgCl}$ on a Au(111) single crystal. (a) 2θ scan of the $Co_xFe_{3-x}O_4$ film. (b) (311) pole figure of the $Co_xFe_{3-x}O_4$ film. The in-plane orientations of the Au(111) substrate were also measured and are shown as the arrows with directions.

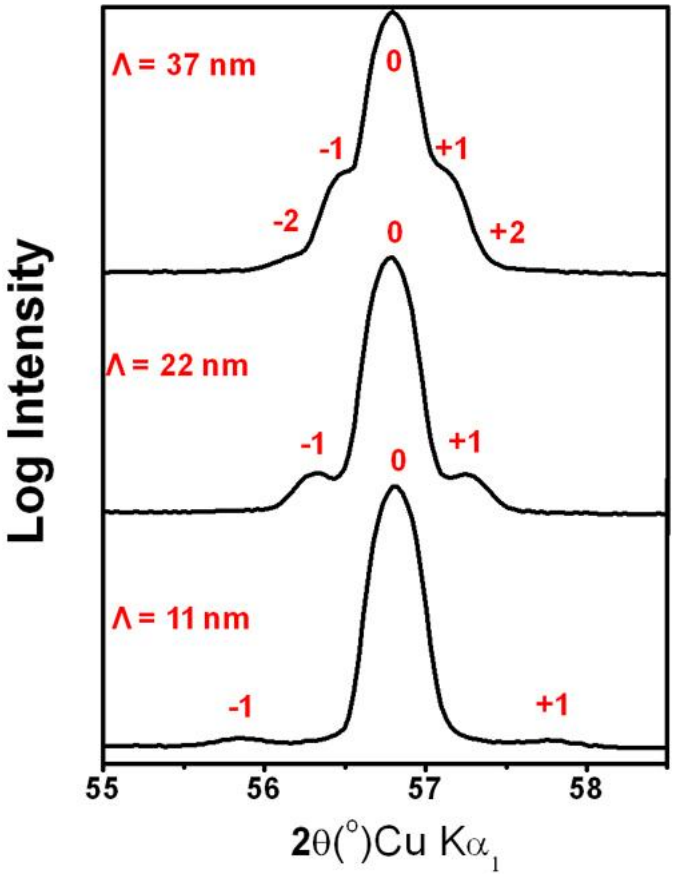

Figure 6. X-ray diffraction 2θ scans around the (333) reflection of the $Co_xFe_{3-x}O_4$ superlattices (#1 to #3 from top to bottom) showing satellite peaks around the main Bragg peak. The calculated modulation wavelengths of the $Co_xFe_{3-x}O_4$ superlattices are shown next to the corresponding scans.

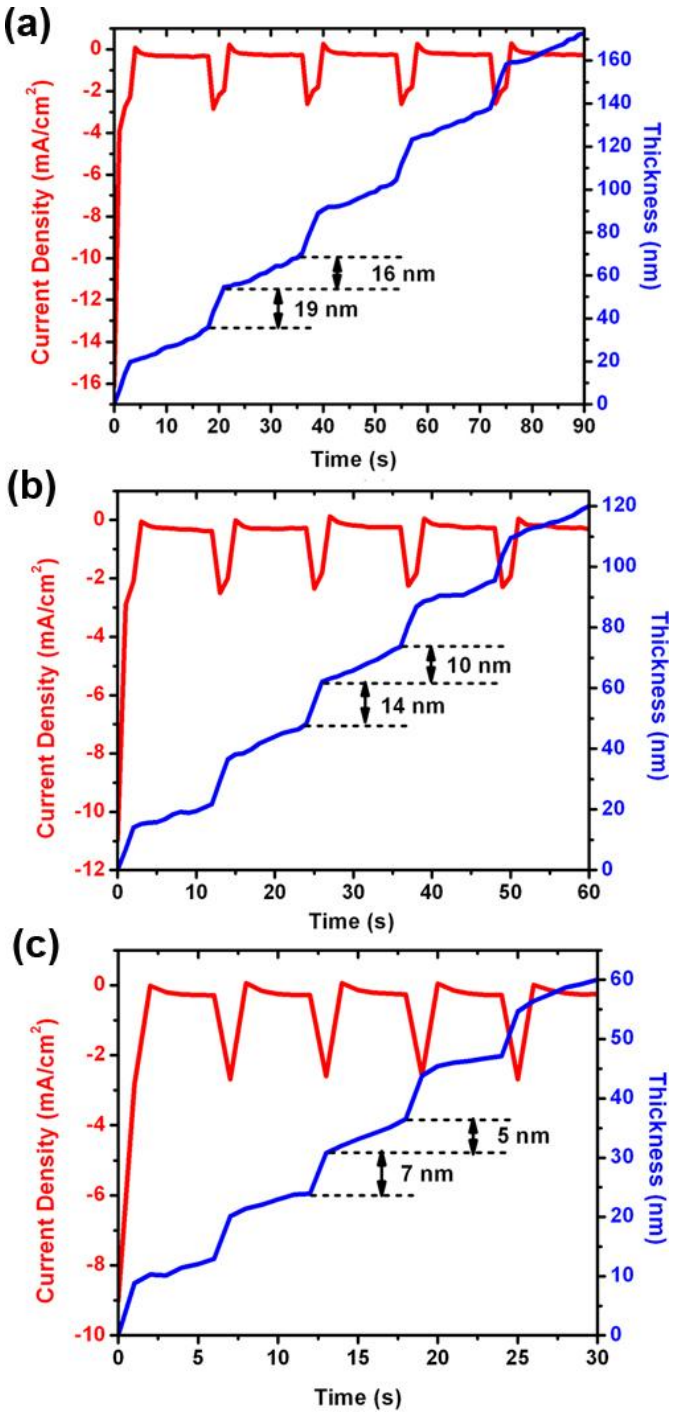

Figure 7. Electrochemical quartz crystal microbalance (EQCM) measurements for the $Co_xFe_{3-x}O_4$ superlattices (a) #1, (b) #2, and (c) #3 (see Table 1). Red curves are current/time transients and blue curves are thickness/time transients.

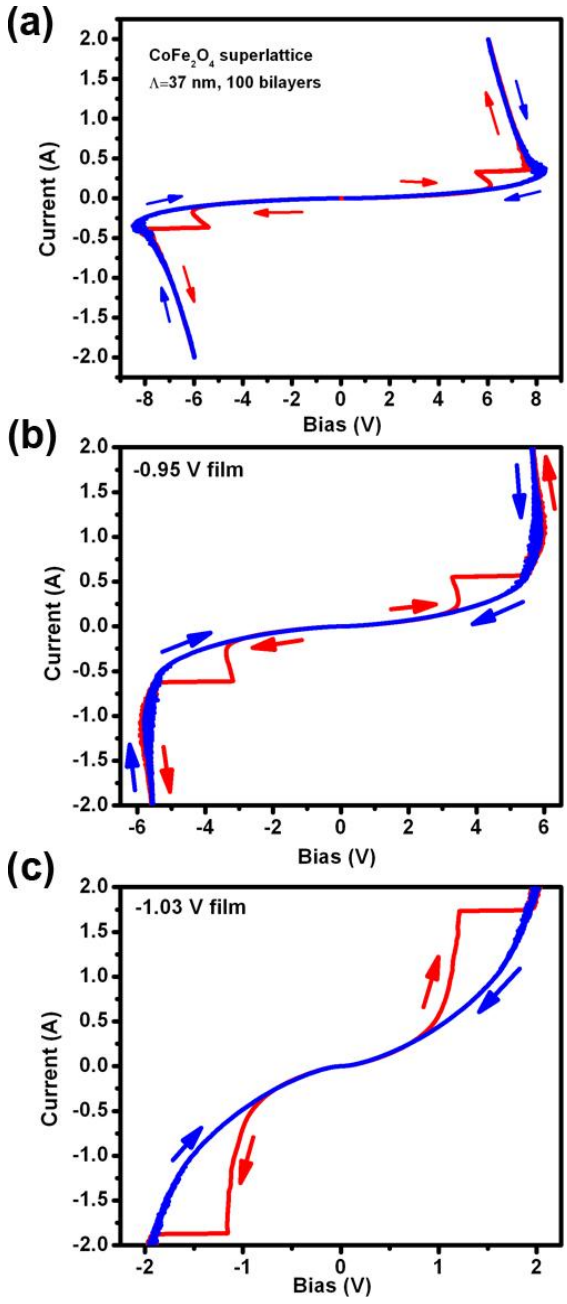

Figure 8. Resistance switching of (a) $Co_xFe_{3-x}O_4$ superlattice #1, (b) -0.95 $V_{Ag/AgCl}$ $Co_xFe_{3-x}O_4$ film, and (c) -1.03 $V_{Ag/AgCl}$ $Co_xFe_{3-x}O_4$ film on Au(111) at 77 K. The iV curve was run with the current flowing perpendicular to the films by scanning the applied current at 50 mA/s. In each curve, the forward scan is red and the reverse scan is blue.

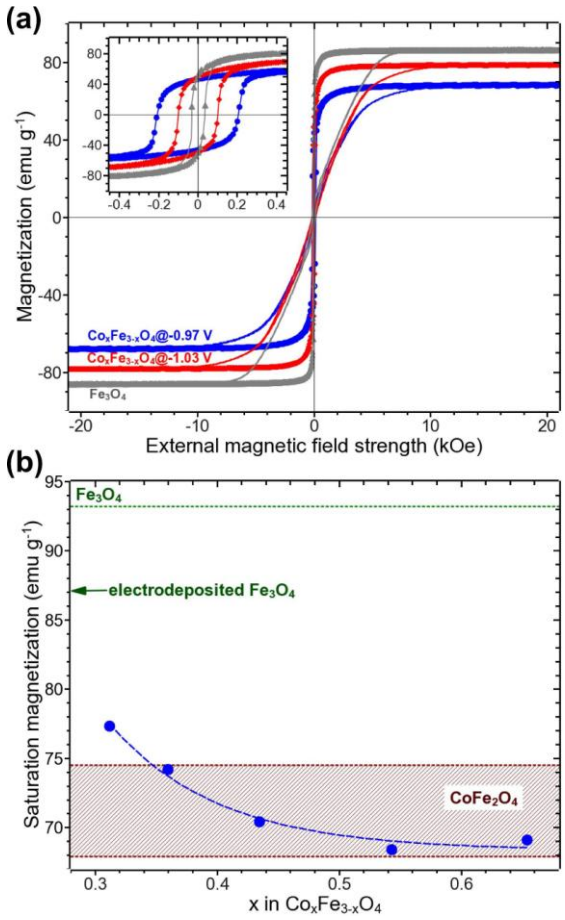

Figure 9. Magnetic characterization of the $Co_xFe_{3-x}O_4$ films with different Co/Fe ratios deposited on Au sputtered glass substrates. (a) In-plane (line with points) and out-of-plane hysteresis loops measured at 300 K and scan rate of 100 Oe/s for 1 ± 0.1 μm thick Fe_3O_4 film and the $Co_xFe_{3-x}O_4$ films deposited at -0.97 and -1.03 $V_{Ag/AgCl}$. The inset in (a) shows the high resolution scans (10 Oe/s) close to the origin in order to highlight the coercivity changes with the composition of the films. (b) The M_S of the $Co_xFe_{3-x}O_4$ films as a function of the composition of the films. Green arrow indicates the measured M_S of the electrodeposited Fe_3O_4 thin film. The theoretical M_S values of bulk Fe_3O_4 and $CoFe_2O_4$ are also shown as a green dashed line and a patterned area, respectively, in the figure.

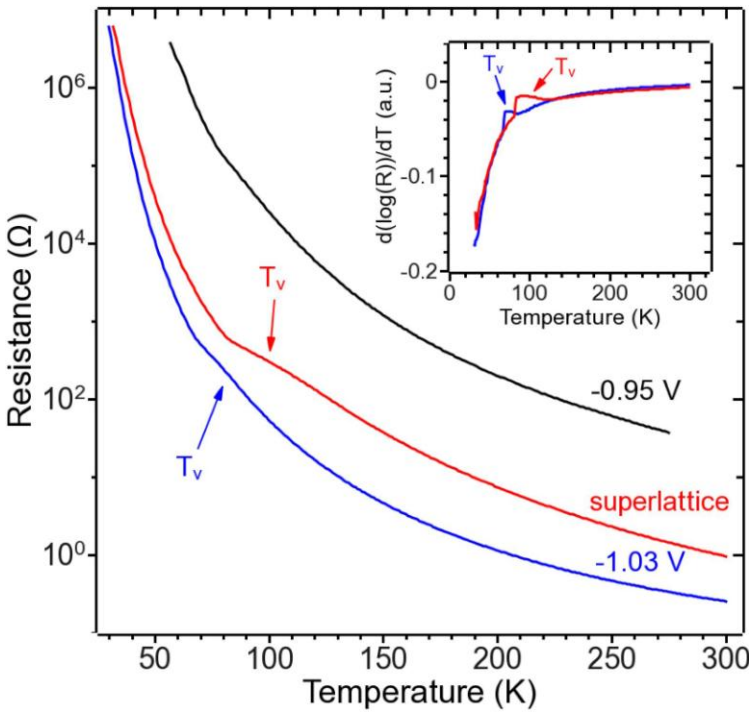

Figure 10. Resistances as a function of temperature for the $Co_xFe_{3-x}O_4$ films deposited at -0.95 (black curve), -1.03 $V_{Ag/AgCl}$ (blue curve) and superlattice #1 (red curve). The inset shows the differentiation of logarithm of resistance vs. temperature plots. It is used to determine the Verwey transition temperatures of these films.

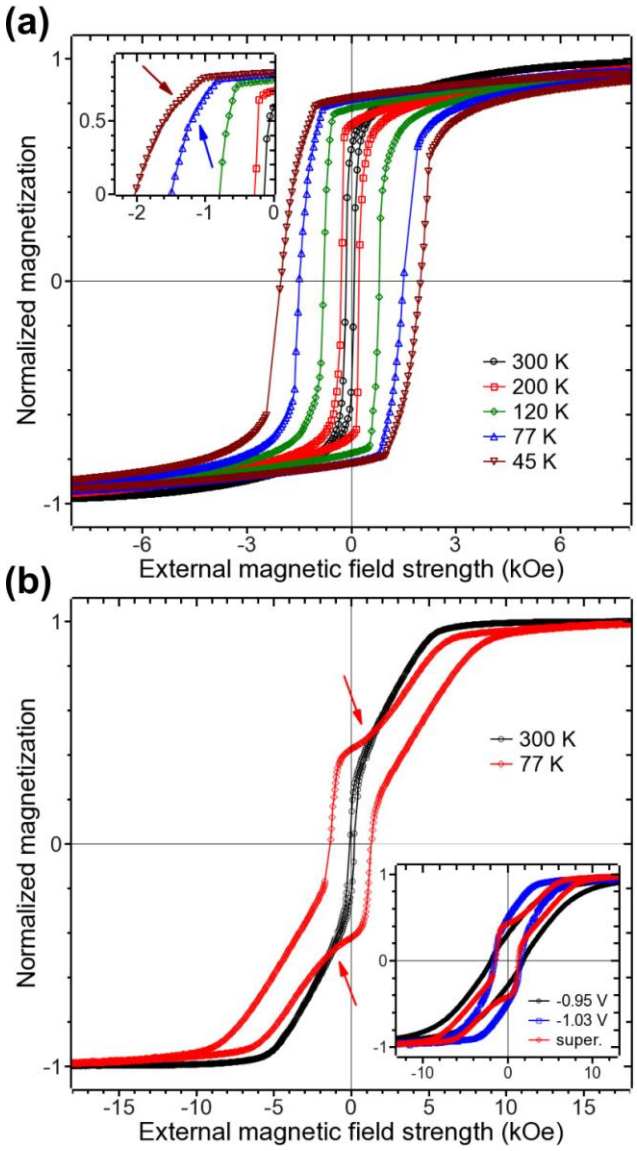

Figure 11. Hysteresis loops of the $Co_xFe_{3-x}O_4$ superlattices #1 measured (a) in plane and (b) out-of-plane at different temperatures as labeled. The inset in (a) shows the magnified part where the signatures of two-step loops at low temperatures are indicated by arrows. The inset in (b) compares the 77 K out-of-plane hysteresis loops of $Co_xFe_{3-x}O_4$ superlattices #1 and two individual films deposited at -0.95 and -1.03 $V_{Ag/AgCl}$ on Au(111) substrates.

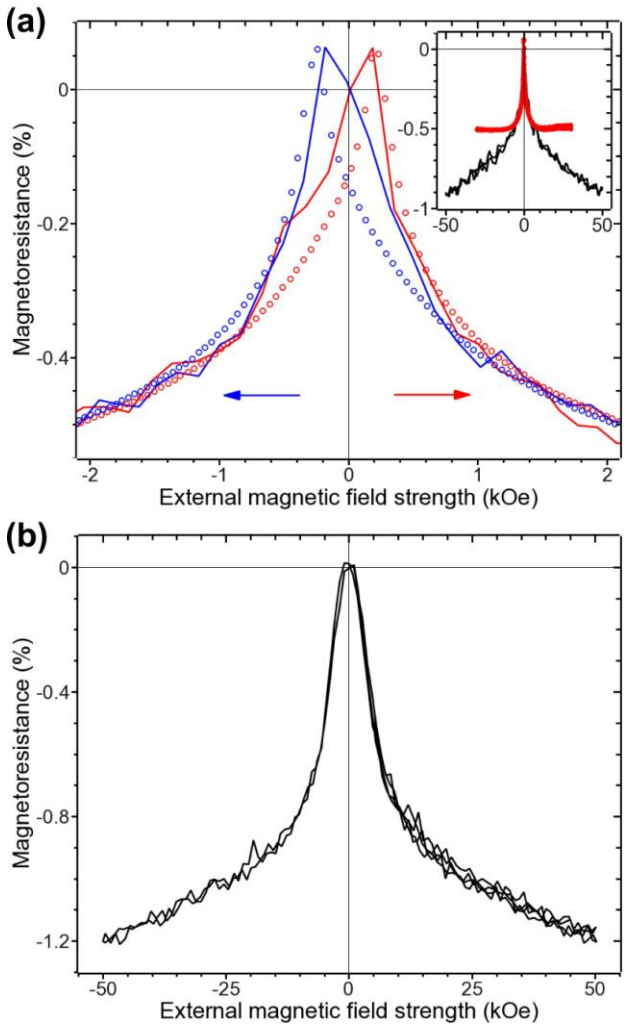

Figure 12. Magnetoresistance of a -1.03 $V_{Ag/AgCl}$ $Co_xFe_{3-x}O_4$ film on a Au(111) single crystal measured at 300 K with the magnetic field applied (a) in and (b) out of the film plane. Blue curves represent the scans from positive to negative while red curves represent the scans from negative to positive in magnetic field. The points in (a) are the square of magnetization, $C(M/M_S)^2$, calculated from VSM hysteresis loop of the same film. The black curve in the inset of (a) is the MR measured up to 50 kOe and the red curve in the inset of (a) is the square of magnetization fit.

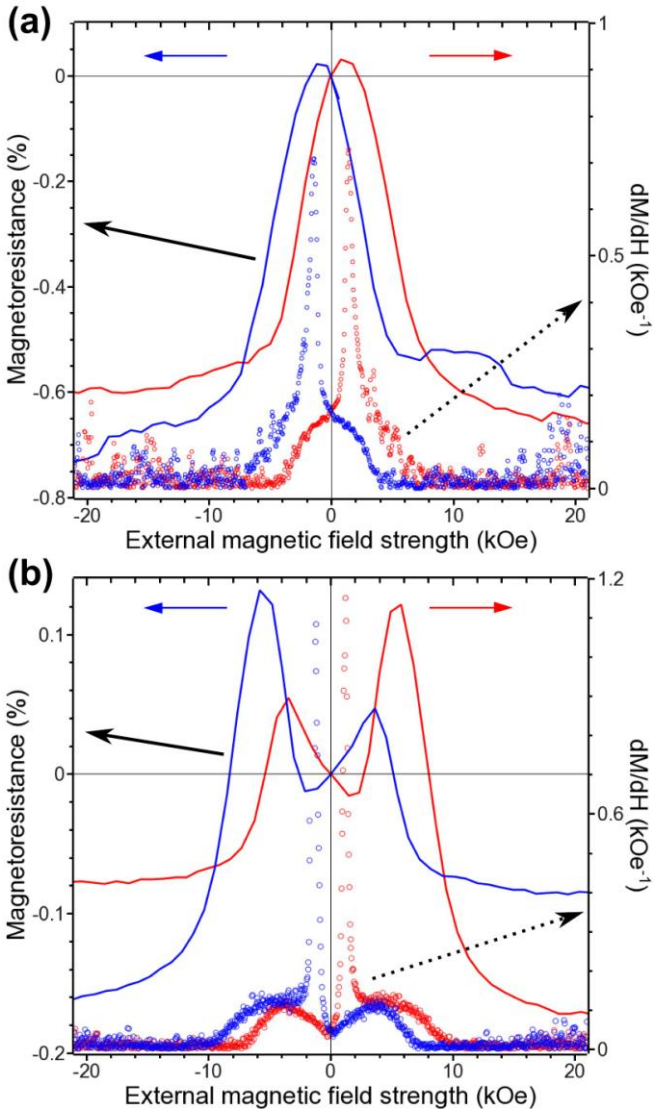

Figure 13. Magnetoresistance (lines) and dM/dH curves measured at 77 K with magnetic field applied out of the film plane for (a) the individual $Co_xFe_{3-x}O_4$ film deposited at -1.03 $V_{Ag/AgCl}$ and (b) superlattice #1 on Au(111) single crystals. Blue curves represent the scan from positive to negative while red curves represent the scan from negative to positive in magnetic field.

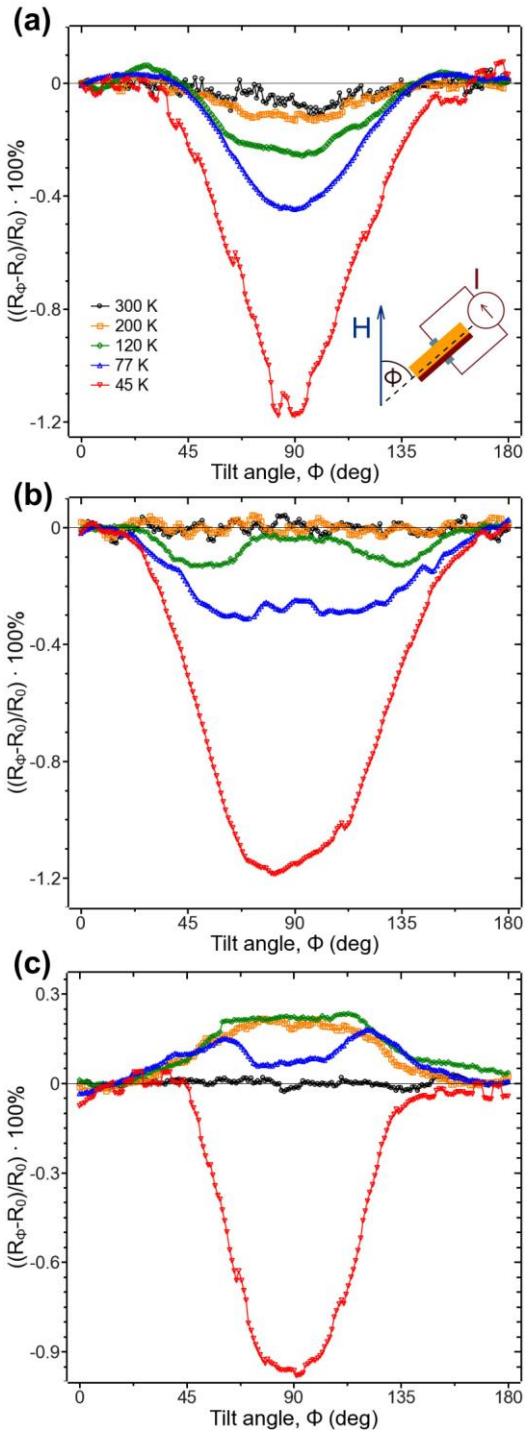

Figure 14. Normalized angular-dependent magnetoresistance measured with an applied magnetic field of 20 kOe at different temperatures for the $Co_xFe_{3-x}O_4$ individual films deposited at (a) -0.95 and (b) -1.03 $V_{Ag/AgCl}$ and (c) superlattice #1 on Au(111) single crystals.

III. Electrodeposition of crystalline Co_3O_4 – a potent oxygen evolution catalyst

Jakub A. Koza‡, Zhen He‡, Andrew S. Miller, and Jay A. Switzer*

Department of Chemistry and Graduate Center for Materials Research, Missouri University of Science and Techology, Rolla, MO 65409-1170, USA

KEYWORDS: water electrolysis, oxygen evolution catalyst, cobalt oxide, Co_3O_4, electrodeposition

ABSTRACT

Films of Co_3O_4 are deposited by electrochemically oxidizing a tartrate complex of Co^{2+} in an aqueous, alkaline solution at elevated temperatures. The Co_3O_4 films deposited from refluxing electrolyte are crystalline without any heat treatment. The films deposit with the normal spinel structure, with a lattice parameter of 0.8097 nm and crystallite size of 26 nm. Co_3O_4 films exhibit excellent catalytic activity towards the oxygen evolution reaction (OER), with a Tafel slope of 49 mV/decade. The films deposit epitaxially on single-crystal Au(100). This opens up the possibility to study the catalytic activity of different Co_3O_4 planes exposed to the electrolyte.

INTRODUCTION

The kinetic bottleneck of electrochemical and photoelectrochemical (PEC) water splitting is the oxygen evolution reaction (OER).[1,2] OER catalysts include transition metal oxides such as RuO_2, IrO_2, PtO_2, MnO_2, and Co_3O_4.[3] Although the most active of these catalysts are the expensive noble metal oxides RuO_2, IrO_2, and PtO_2, there is interest in developing OER catalysts based on earth-abundant metals such as Co. Co_3O_4 is slightly

less active than the noble metal oxides for water oxidation in alkaline solution.[3] Kanan and Nocera have also shown that an amorphous cobalt-phosphate (CoPi) OER catalyst can be electrodeposited, which works in neutral solution.[4] Here, we report that crystalline spinel Co_3O_4 films with *Fd3m* space group can be produced by electrochemical oxidation of Co(II) complexed with tartrate (tart) at elevated temperatures. Co_3O_4 is reported to be a p-type semiconductor with a bandgap of about 2.4 eV.[5-7] The bandgap is larger than that of Si (1.1 eV), which makes it a promising candidate for silicon-based PEC water splitting applications. That is, it will catalyze the oxygen evolution reaction, but it will not significantly attenuate light absorption by Si. Co_3O_4 is also a good candidate for a PEC cell using other n-type semiconductors as photoanodes, such as TiO_2, Fe_2O_3 or WO_3. In contrast to Si these oxides are stable in alkaline solution. Co_3O_4 is generally produced by thermal methods such as thermal decomposition, hydrothermal, or spray pyrolysis.[3,8,9] To the best of the authors' knowledge, attempts to electrodeposit Co_3O_4 films have led to the formation of amorphous and/or hydrated layers.[10,11] In our work, crystalline Co_3O_4 films are deposited galvanostatically from a solution of 5 mM Co(II) and 6 mM L-tartrate in 2 M NaOH at temperatures ranging from 50 to 103 ^oC (reflux). The method does not require heat treatment of the deposit, because the as-deposited material is fully crystalline. Moreover, the films can be grown epitaxially on a single crystal Au(100) substrate. This opens up the possibility to study the catalytic activity towards OER of different Co_3O_4 crystal planes exposed to the electrolyte.

EXPERIMENTAL SECTION

Deposition solution: The electrolyte used for deposition of Co_3O_4 is of following composition: 5 mM Co^{2+} and 6 mM tartrate (tart) in 2 M NaOH. In order to prepare the electrolyte a Co^{2+}-(tart) stock solution was prepared by dissolving an appropriate amount of $Co(NO_3)_2.7H_2O$ and L-tartaric acid powders into de-ionized (DI) water to form 0.1 M Co^{2+} and 0.12 M tartrate solution. Finally, a proper volume of the stock solution was dissolved into NaOH solution to form the nominal composition. The tartaric acid was used to complex Co^{2+} ions to be soluble at pH of 14, where according to the Pourbaix diagram Co_3O_4 is thermodynamically stable.

Electrochemical methods: All electrodeposition experiments were performed in a three-neck flask with an electrolyte volume of 200 ml in a standard three-electrode setup using a Princeton Applied Research EG&G 273A potentiostat. A condenser was attached to one of the necks of the flask in order to prevent electrolyte losses due to evaporation. The temperature was maintained with a heating mantle and monitored by a thermometer. The electrolyte prior to depositing was purged with Ar for about 60 min to prevent atmospheric oxidation of Co^{2+}. An Ar atmosphere above the electrolyte was maintained during all experiments. A stainless steel type 430 (SS), an Au sputtered glass, and a single crystal Au(100) were used as the working electrodes. An ultra-high purity pyrolytic graphite rod served as the counter electrode and a $Ag/AgCl/KCl_{sat.}$ reference electrode was used. The SS and Au(100) substrates were mechanically polished, sonicated in acetone and rinsed with DI water prior to experiments. The Au(100) substrate was also electropolished prior to depositing according to procedure described elsewhere.[12] All films were deposited by passing a constant charge of 0.9 C cm^{-2}.

The catalytic properties of the deposits were investigated in 1 M KOH solution at room temperature (RT) in a three-electrode cell using a Brinkmann PGSTAT 30 Autolab potentiostat. The deposit served as the working electrode and a Pt mesh was the counter electrode. The OER experiments were performed on fresh layers immediately (after rinsing with DI water) after deposition. The overpotentials were calculated with respect to the thermodynamic potential of oxygen evolution at pH 14 (0.401 V vs. NHE.).

Characterization: The structure of the films was determined using a high-resolution Philips X-Pert MRD X-ray diffractometer (XRD) with a $CuK\alpha_1$ radiation source (λ=1.54056 Å). The morphology of films was studied by scanning electron microscopy (SEM – Hitachi S4700 FESEM) and optical microscopy. The thickness of deposited films was determined with a profilometer (Solan – DEKTAK II).

RESULTS AND DISCUSSION

The electrochemistry of the Co(II)tartrate electrolyte was studied by linear sweep voltammetry (LSV) and galvanostatic depositions. Figure 1a shows the LSVs at a stainless steel (SS) working electrode obtained at different temperatures. As the potential increases, a wave in the LSV is observed, which corresponds to the Co(II)/Co(III) redox couple (Eq. 1) followed by a steep increase of the current due to the OER. The Co_3O_4 deposition is believed to proceed via an electrochemical-chemical (EC) route:

$$2Co^{2+}(tart) \rightarrow 2Co^{3+} + 2(tart) + 2e^- \quad (1)$$

$$2Co^{3+} + Co^{2+}(tart) + 8OH^- \rightarrow Co_3O_4 + 4H_2O + (tart) \quad (2)$$

The deposition scheme is analogous to that proposed by Kothari et al. for Fe_3O_4 deposition[13] and is in agreement with the deposition mechanism proposed by Casella for hydrated cobalt oxide compounds.[10,11] From the temperature dependence on the LSVs it is clear that by increasing the electrolyte temperature, the current density of the oxidation peak increases and the onset of the oxidation peak shifts towards lower potentials. This leads to a decrease of the potential at which films can be grown at a given current density. Figure 1b shows the dependencies of the deposit thickness on the charge density passed during galvanostatic depositions from a refluxing electrolyte at 0.1 and 0.25 mA cm^{-2} current densities.

A linearity obtained at 0.25 mA cm^{-2} can be seen, whereas, the dependence obtained at 0.1 mA cm^{-2} shows a negative deviation from linearity. This suggests that at 0.1 mA cm^{-2} another parallel reaction consumes a significant portion of charge. The most probable explanation is the ligand (tartrate) oxidation, as it was observed in the cyclic voltammograms measured in the electrolyte without Co ions (Figure S1 – Supporting Information). An estimation of the current efficiency at 0.25 mA cm^{-2} based on the proposed deposition mechanism, the film thickness, assuming the density of the deposit equal to that of bulk material (6.056 g cm^{-3}), gave a value of roughly 100 %, regardless of the deposition time. In the case of the deposition at 0.1 mA cm^{-2} the efficiency decays from 100 % at the beginning to about 60 % after 2.5 h (0.9 Ccm^{-2}) of the process.

Figure 2 shows optical micrographs of the films deposited at 0.25 mA cm^{-2} and different temperatures. The layers deposited at low temperatures exhibit very poor adhesion. Films peel off from the substrate upon drying, as shown for the film deposited at 50 ^{o}C in Figures 2a-d, which represent a time sequence. The adhesion of the film

deposited at 75 ^{o}C (Figure 2e) improved significantly, but the film has a cracked-mud morphology (some peeling off at the electrode edges was noticed).

A similar observation was made by Kanan and Nocera for electrodeposited CoPi films.[4] Spataru et al. also reported that electrodeposited, amorphous/hydrated Co_3O_4 films display very non-uniform morphology, i.e., the films appeared discontinuous with isolated particles and a preferential deposition at the edges.[14] However, the film deposited from a refluxing electrolyte is very adherent, with a smooth and crack-free surface (Figure 2f).

The structure of the deposit was determined by X-ray diffraction (XRD). Figure 3a shows XRD patterns of the layers deposited at 0.25 mA cm^{-2} and temperatures of 50 (black curve) and 103 ^{o}C (refluxing electrolyte – blue curve). The XRD pattern of the film deposited at 50 ^{o}C displays the SS substrate peaks and very broad and low intensity peaks, which can be assigned as Co_3O_4. This indicates a nanocrystalline nature of the film. The pattern is similar to the one published by Nakaoka et al. for an electrodeposited Co_3O_4 film.[15] They observed only a single, broad and low intensity (311) peak. Similar results were also published on Co_3O_4 electrodeposition by other researchers. It was reported that as-deposited Co_3O_4 films are amorphous and/or hydrated[10,11,14,16] and require heat treatment to crystallize.[16-18] However, the film deposited from a refluxing electrolyte (103 ^{o}C) appears fully crystalline, with sharp peaks in the XRD pattern corresponding to Co_3O_4 (a = 0.8097 nm).

The crystallinity of the electrodeposited Co_3O_4 was a strong function of the deposition temperature and current density. The crystallite size was estimated from the line broadening of the (311) peak using the Scherrer equation. As shown in Figure 3b, the

crystallite size increases as the temperature is increased, with a dramatic increase in size at reflux. The crystallite size increases from a value of about 2 nm at 50 ^{o}C to about 26 nm at 103 ^{o}C. For a series of films grown at reflux temperature, the crystallite size decreases as the current density is increased (see Figure 3c). These results are consistent with the EC mechanism proposed in Eq. 1 & 2. Although the rate of the electrochemical reaction (Eq. 1) is constant at a constant current density, the rate of the chemical reaction (Eq. 2) would be faster at higher temperatures. Hence, at higher temperatures and lower currents there would be lower supersaturation of Co(III) at the electrode surface, leading to more crystallographically ordered films.

The electrodeposition from a refluxing electrolyte can be considered to be an electro-hydrothermal process.[19-23] Yoshimura and co-workers introduced the electro-hydrothermal method for $BaTiO_3$ synthesis in 1997.[19] The deposition of $BaTiO_3$ employs an anodic dissolution of the working electrode, which serves as a source of one of the metal ions. In our case, the Co_3O_4 is deposited from solution precursors, which gives a larger degree of freedom regarding the choice of the substrate. Preliminary investigations have shown, for example, that Co_3O_4 can be deposited onto p^+-Si (Figure S2 – Supporting Information).

The catalytic properties of the Co_3O_4 films towards OER were studied in 1 M KOH at room temperature. Figure 4a shows the steady state polarization curve measured on a film deposited at 0.25 mA cm^{-2} from a refluxing electrolyte (red line and open circles). The data was not corrected for IR drop. A fit to the linear part of the polarization curve at low overpotentials gave a Tafel slope of 49 mV dec^{-1}, which is close to, and in many cases lower than, the values of Co_3O_4 films synthesized via different

methods (50 – 189 mV dec^{-1}).[24] Our film is comparable to the Co_3O_4 deposited via spray pyrolysis method on Ni (Tafel slope of 51 mV dec^{-1} – wine diamonds in Figure 4a).[8] In addition, the data of CoPi film in neutral solution is shown. The catalytic activity of Co_3O_4 is higher than that of CoPi. At an overpotential of 0.41 V the current density was 1 mA cm^{-2} on CoPi and is approximately 17 mA cm^{-2} on the Co_3O_4 film. Also the Tafel slope obtained on the Co_3O_4 film (49 mV dec^{-1}) is lower then that reported for CoPi (60 mV dec^{-1}). The films operating in neutral solutions may have advantages over the films operating in base with respect to silicon-based PEC applications. However, there are several reports in which Si was stabilized to work in alkaline solutions, such as an electrodeposited Tl_2O_3 film on n-Si[25] or a tunnel oxide layer of TiO_2 on n-Si produced by atomic layer deposition.[26] Our results are compared to the data reported by Spataru at al. for electrodeposited, amorphous/hydrated Co_3O_4 films (Tafel slope of 67 mV dec^{-1} – squares in Figure 4a).[14] Our film is considerably more active at current densities higher than 1 mA cm^{-2}. This is a desirable property, as the PEC water splitting requires current densities of 10-20 mA cm^{-2} and commercial water electrolysis is run at current densities as high as 1 A cm^{-2}.[1]

The stability of the Co_3O_4 films was studied in 1 M KOH at 10 and 100 mA cm^{-2} for 48 h (Figure 4b). The overpotential vs. time dependence obtained at 10 mA cm^{-2} does not show significant changes over time. The curve measured at 100 mA cm^{-2} shows an increase in overpotential during the initial 24 h and then stabilizes. Similar results were previously reported by Singh et al. during long time anodic polarization at 25 mA cm^{-2} of Co_3O_4 films deposited via chemical spray pyrolysis.[27,28] XRD studies of the film after the long time polarization did not reveal any changes of the crystal structure. SEM

investigations also did not show any significant changes in the film morphology. This suggests that the films prepared by our method may be suitable for use in PEC devices by fulfilling the long term stability requirement.

It is also possible to electrodeposit epitaxial films of Co_3O_4. Figure 5a shows the XRD pattern of the Co_3O_4 film deposited on a Au(100) single crystal substrate. The film grows with a preferred {111} out-of-plane orientation. Only a very small intensity peak of the (311) reflection can be seen. A (311) pole figure was measured (Figure 5b), which shows distinct peaks revealing that the film is epitaxial.

The pole figure was compared to the stereographic projections (Figure S3 – Supporting Information) and the epitaxial relationship was found to be $Co_3O_4(111)[11\ \bar{2}]||Au(100)<001>$. The low intensity peak in the center of the pole figure corresponds to the (311) plane observed in the XRD pattern (Figure 5a). The epitaxial growth of Co_3O_4 films opens up the possibility to study catalytic activity towards the OER of different planes exposed to the electrolyte. Both the in- and out-of-plane orientations can be controlled by carefully choosing the substrate and deposition parameters as shown for other electrodeposited oxide films.[29-31] It is known that different atomic planes have not only different atomic densities but also differ with respect to their electronic structure.[32] Xie et al. have shown that the {110} planes in Co_3O_4 have the highest catalytic activity towards CO oxidation at low temperature due to its highest density of Co^{3+} ions.[33] Hu et al. have also shown that the {112} planes in Co_3O_4 are more reactive in the catalytic combustion of methane than the {001} and {011} planes.[9] It is reasonable to assume that different planes of Co_3O_4 will differ with respect to the OER

catalytic activity. This should improve the fundamental understanding of the processes involved in the OER at Co_3O_4.

CONCLUSIONS

We have shown that films of spinel Co_3O_4 can be deposited by electrochemical oxidation of Co(II)tartrate in alkaline solution at elevated temperatures (reflux). The as-deposited films are fully crystalline and do not require any further heat treatment. The films deposited from refluxing electrolyte grow with the normal spinel structure, with a lattice parameter of 0.8097 nm and crystallite size of 26 nm. The electrolyte temperature is the most critical parameter controlling the crystallinity of the film. A dramatic increase of the crystallite size was observed at the reflux temperatures. The films are very smooth, crack-free, and adherent. Co_3O_4 films exhibit excellent catalytic activity towards the OER, with a Tafel slope of 49 mV/decade, and very good chemical stability over time in 1 M KOH. We have also shown that the films can be electrodeposited epitaxially on single-crystal Au(100). The film grows with a preferred {111} out-of-plane orientation on Au(100). The epitaxial relationship is $Co_3O_4(111)[11\ \bar{2}]||Au(100)<001>$. The epitaxial growth of Co_3O_4 opens up the possibility to study the catalytic activity towards OER of different crystal planes exposed to the electrolyte. In future work we plan to electrodeposit the Co_3O_4 OER catalyst onto n-type semiconductor photoanodes such as n-Si, TiO_2, Fe_2O_3 and WO_3 for photoelectrochemical water splitting.

ASSOCIATED CONTENT

Supporting Information. XRD pattern and Raman spectrum of the film deposited on p^+-Si, stereographic projections, LSVs of the substrates and films deposited on SS and Ti, and Tafel plots of the film with and without IR correction. This material is available free of charge via the Internet at http://pubs.acs.org.

AUTHOR INFORMATION

‡ These authors contributed equally

Corresponding Author

*E-mail: jswitzer@mst.edu

ACKNOWLEDGEMENT

This work was supported by the U.S. Department Of Energy, Office of Basic Sciences under Grant No. DE-FG02-08ER46518.

REFERENCES

(1) Walter, M. G.; Warren, E. L.; McKone, J. R.; Boettcher, S. W.; Mi, Q.; Santori, E. A.; Lewis, N. S. *Chem. Rev.* **2010**, *110*, 6446.

(2) Zhong, D. K.; Gamelin, D. R. *J. Am. Chem. Soc.* **2010**, *132*, 4202.

(3) Trasatti, S. *Electrochim. Acta* **1984**, *29*, 1503.

(4) Kanan, M. W.; Nocera, D. G. *Science* **2008**, *321*, 1072.

(5) Petitto, S. C.; Langell, M. A. *J. Vac. Sci. Technol. A* **2004**, *22*, 1690.

(6) Long, M.; Cai, W.; Cai, J.; Zhou, B.; Chai, X.; Wu, Y. *J. Phys. Chem. B* **2006**, *110*, 20211.

(7) Kandalkar, S. G.; Gunjakar, J. L.; Lokhande, C. D.; Joo, O.-S. *J. Alloys Compd.* **2009**, *478*, 594.

(8) Singh, S. P.; Samuel, S.; Tiwari, S. K.; Singh, R. N. *Int. J. Hydrogen Energ.* **1996**, *21*, 171.

(9) Hu, L.; Peng, Q.; Li, Y. *J. Am. Chem. Soc.* **2008**, *130*, 16136.

(10) Innocenzo G, C. *J. Electroanal. Chem.* **2002**, *520*, 119.

(11) Casella, I. G.; Di Fonzo, D. A. *Electrochim. Acta* **2011**, *56*, 7536.

(12) Boonsalee, S.; Gudavarthy, R. V.; Bohannan, E. W.; Switzer, J. A. *Chem. Mater.* **2008**, *20*, 5737.

(13) Kothari, H. M.; Kulp, E. A.; Limmer, S. J.; Poizot, P.; Bohannan, E. W.; Switzer, J. A. *J. Mater. Res.* **2006**, *21*, 293.

(14) Spataru, N.; Terashima, C.; Tokuhiro, K.; Sutanto, I.; Tryk, D. A.; Park, S.-M.; Fujishima, A. *J. Electrochem. Soc.* **2003**, *150*, E337.

(15) Nakaoka, K.; Nakayama, M.; Ogura, K. *J. Electrochem. Soc.* **2002**, *149*, C159.

(16) Wu, J. B.; Lin, Y.; Xia, X. H.; Xu, J. Y.; Shi, Q. Y. *Electrochim. Acta* **2011**, *56*, 7163.

(17) Yuan, Y. F.; Xia, X. H.; Wu, J. B.; Huang, X. H.; Pei, Y. B.; Yang, J. L.; Guo, S. Y. *Electrochem. Commun.* **2011**, *13*, 1123.

(18) Xia, X. H.; Tu, J. P.; Zhang, J.; Xiang, J. Y.; Wang, X. L.; Zhao, X. B. *ACS Appl. Mater. Interfaces* **2009**, *2*, 186.

(19) Yoo, S. E.; Yoshimura, M.; Sōmiya, S. *J. Mater. Sci. Lett.* **1989**, *8*, 530.

(20) Yoshimura, M.; Yoo, S.-E.; Hayashi, M.; Ishizawa, N. *Jpn. J. Appl. Phys.* **1989**, *28*, L2007.

(21) Yoshimura, M.; Suchanek, W. *Solid State Ionics* **1997**, *98*, 197.

(22) Suchanek, W. L.; Watanabe, T.; Sakurai, B.; Kumagai, N.; Yoshimura, M. *Rev. Sci. Instr.* **1999**, *70*, 2432.

(23) Song, S.-W.; Han, K.-S.; Yoshimura, M. *J. Am. Cer. Soc.* **2000**, *83*, 2839.

(24) Hamdani, M.; Singh, R. N.; Chartier, P. *Int. J. Electrochem. Sci.* **2010**, *5*, 556.

(25) Switzer, J. A. *J. Electrochem. Soc.* **1986**, *133*, 722.

(26) Chen, Y. W.; Prange, J. D.; Dünen, S.; Park, Y.; Gunji, M.; Chidsey, C. E. D.; McIntyre, P. C. *Nat. Mater.* **2011**, *10*, 539.

(27) Singh, R. N.; Hamdani, M.; Koenig, J. F.; Poillerat, G.; Gautier, J. L.; Chartier, P. *J. Appl. Electrochem.* **1990**, *20*, 442.

(28) Singh, R. N.; Koenig, J. F.; Poillerat, G.; Chartier, P. *J. Electrochem. Soc.* **1990**, *137*, 1408.

(29) Switzer, J. A.; Shumsky, M. G.; Bohannan, E. W. *Science* **1999**, *284*, 293.

(30) Liu, R.; Vertegel, A. A.; Bohannan, E. W.; Sorenson, T. A.; Switzer, J. A. *Chem. Mater.* **2001**, *13*, 508.

(31) Sorenson, T. A.; Morton, S. A.; Waddill, G. D.; Switzer, J. A. *J. Am. Chem. Soc.* **2002**, *124*, 7604.

(32) Xu, X.-L.; Chen, Z.-H.; Li, Y.; Chen, W.-K.; Li, J.-Q. *Surf. Sci.* **2009**, *603*, 653.

(33) Xie, X.; Li, Y.; Liu, Z.-Q.; Haruta, M.; Shen, W. *Nature* **2009**, *458*, 746.

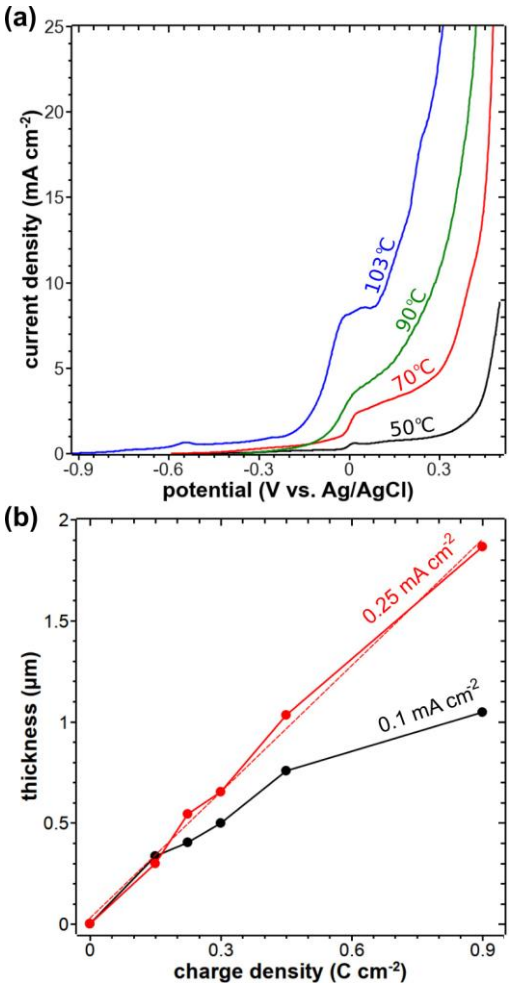

Figure 1. Electrochemistry of the Co(II)(tart) electrolyte. (a) Linear sweep voltammograms measured at different electrolyte temperatures at a scan rate of 50 mV s^{-1} on a SS substrate. (b) Thickness vs. charge density dependencies obtained in a refluxing electrolyte (103 ^{o}C) at current densities of 0.1 (black) and 0.25 mA cm^{-2} (red), Au/glass substrate. The dashed red line is a linear fit to the 0.25 mA cm^{-2} data.

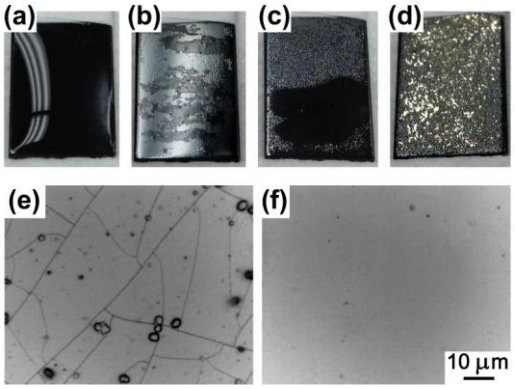

Figure 2. Morphology of deposited films. (a-d) Optical images of the film deposited at 50 ^{o}C representing a time sequence upon drying. (a) The as-deposited film with a water film on it. The film was dried in air at room temperature; time passed between (b) and (d) was 2.5 minutes. (e) and (f) optical microscope images of the films deposited at 75 (e) and 103 ^{o}C (f). Same scale bar for (e) and (f). All films were deposited on a SS substrate at 0.25 mA cm^{-2} by passing a charge density of 0.9 C cm^{-2}.

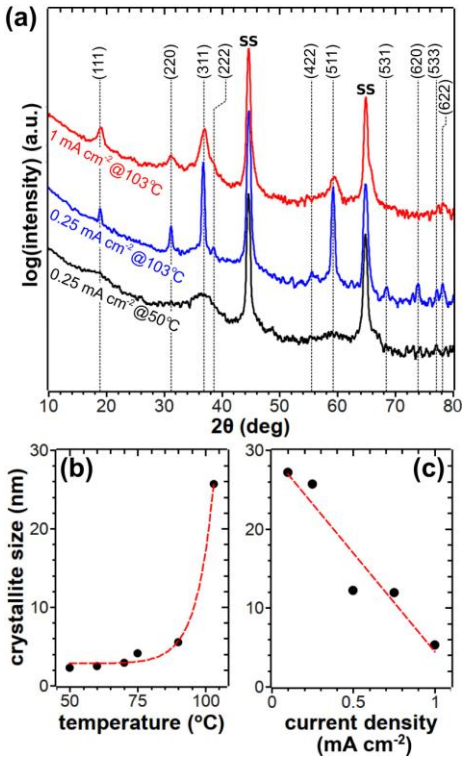

Figure 3. XRD analysis of deposited films. (a) XRD patterns of the films deposited at different conditions as indicated. Dependence of the Co_3O_4 crystallite size on, (b) the electrolyte temperature at 0.25 mA cm^{-2}, and on (c) the current density at 103 ^{o}C. All films were deposited on a SS substrate by passing a charge density of 0.9 C cm^{-2}.

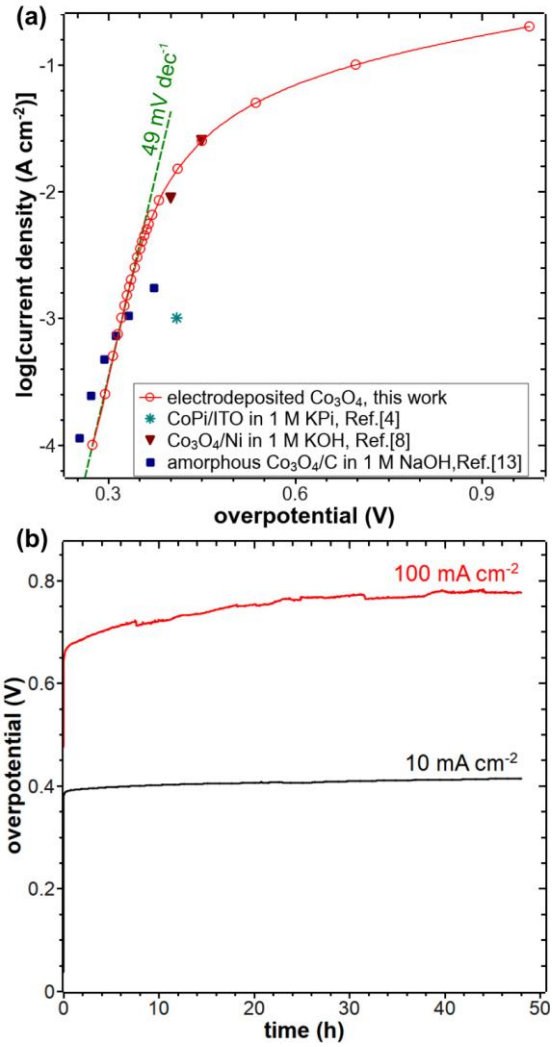

Figure 4. Electrocatalytic activity and electrode stability of electrodeposited Co_3O_4 towards OER. (a) Steady state polarization curve (red line and open circles), with a fit to the linear portion of the curve (dashed green line). Literature data of Co_3O_4 (squares and triangles) and CoPi (asterisk) are plotted for comparison.[4,8,14] (b) Plot of overpotential as a function of time at current densities of 10 (black) and 100 mA cm^{-2} (red). Co_3O_4 deposited at 0.25 mA cm^{-2} from a refluxing electrolyte on a SS substrate by passing a charge density of 0.9 C cm^{-2}. The overpotential was calculated with respect to the thermodynamic potential at pH of 14 of 0.401 V vs. NHE. The data was not corrected for IR drop.

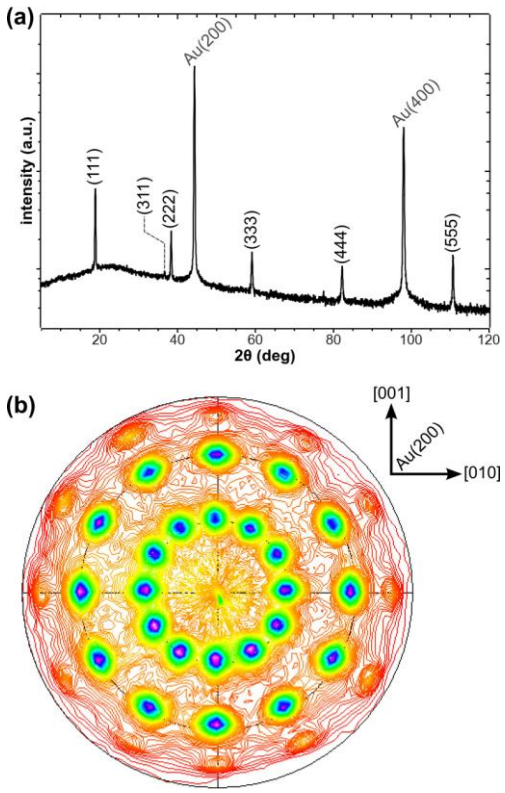

Figure 5. XRD evidence of the epitaxial growth of Co_3O_4 on a Au(100) substrate. (a) X-Ray diffraction pattern of the film. (b) (311) pole figure. The arrows in (b) show the substrate orientation.

2. CONCLUSIONS

The focus of this dissertation is the electrodeposition and electrochemical reduction of epitaxial metal oxide thin films and superlattices. The electrochemical reduction of metal oxides to metals has been studied for decades as an alternative to pyrometallurgical processes for the metallurgy industry. However, the previous work was conducted on bulk polycrystalline metal oxides. Paper I in this dissertation shows that epitaxial face-centered cubic magnetite (Fe_3O_4) thin films can be electrochemically reduced to epitaxial body-centered cubic iron (Fe) thin films in aqueous solution on single-crystalline substrates at room-temperature. This is the first time that the transformation of a solid epitaxial film to another solid epitaxial film by electrochemical reduction is shown. The orientations of the Fe films are controlled by the Au single-crystalline substrates instead of the precursor Fe_3O_4 films. The reduction starts from the Fe_3O_4/Au interface instead of the Fe_3O_4/electrolyte interface. Our preliminary results also show that alloy films can be obtained by electrochemically reducing mixed metal oxide films. This technique opens new possibilities to produce special epitaxial metal/metal oxide heterojunctions and a wide range of epitaxial metallic alloy films from the corresponding mixed metal oxides.

Electrodeposition, like biomineralization, is a soft solution processing method which can produce functional materials with special properties onto conducting or semiconducting solid surfaces. The morphology, orientation and chirality of the materials can be controlled through solution additives, pH or by controlling the applied potential or current density at the electrode surface. In Paper II in this dissertation, the electrodeposition of cobalt-substituted magnetite ($Co_xFe_{3-x}O_4$, $0<x<1$) epitaxial thin films

and superlattices on Au single-crystalline substrates is presented. The atomic Co:Fe ratio in the deposited $Co_xFe_{3-x}O_4$ thin films can be tuned by controlling the deposition potential. Effects of the chemical composition on the structure and the electrical and magnetic properties of the $Co_xFe_{3-x}O_4$ thin films are investigated. Superlattices in the $Co_xFe_{3-x}O_4$ system are also electrodeposited from the same deposition solution by pulsing between two potentials. $Co_xFe_{3-x}O_4$ superlattices and individual films show resistance switching and angular-dependent magnetoresistance. Resistance switching has potential applications in resistive random access memory devices and spintronics. The angular-dependent magnetoresistance mimicks the magnetoreception systems in animals such as homing pigeons and magnetotactic bacteria.

Paper III in this dissertation reports the direct electrodeposition of crystalline cobalt oxide (Co_3O_4) thin films on stainless steel and Au single-crystalline substrates. Crystalline Co_3O_4 has never been electrodeposited without heat treatments before. The crystalline Co_3O_4 thin films exhibit high catalytic activity towards the oxygen evolution reaction (OER) and excellent stability in an alkaline solution. A possible application of the electrodeposited Co_3O_4 is the fabrication of highly active and low-cost photoanodes for photoelectrochemical water-splitting cells.

APPENDIX A.

SUPPORTING INFORMATION FOR PAPER I

Materials and Methods

1. **Direct electrodeposition of Fe/Fe_3O_4 heterojunctions on Au single crystals.**

In this case, both the Fe and Fe_3O_4 layers in the Fe/Fe_3O_4 heterojunction were electrodeposited from a stirred solution of 87 mM Fe(III), 100 mM triethanolamine (TEA), and 2 M NaOH at 80 ℃. The Fe layer was first electrodeposited on Au single crystals by applying a constant potential of -1.35 V vs. Ag/AgCl until 1 C/cm^2 charge passed. After the Fe deposition, the surface of the Au single crystal was completely covered by a shiny iron layer. Then, the Fe_3O_4 layer was electrodeposited on top of the pre-deposited Fe layer by applying a constant potential of -1.065 V vs. Ag/AgCl until 0.5 C/cm^2 charge passed. The out-of-plane and in-plane orientations of the directly deposited Fe and Fe_3O_4 layer layers were determined by X-ray θ-2θ scans and pole figures, as shown in Figure. S1.

2. **Special Fe/Fe_3O_4 heterojunctions produced by partially reducing pre-deposited Fe_3O_4 films.**

The pre-deposited Fe_3O_4 films on Au(100), Au(110) and Au(111) single crystals were partially reduced by applying a constant potential of -1.20 V vs. Ag/AgCl in 2 M NaOH at room-temperature. X-ray θ-2θ scans of all three partially reduced Fe_3O_4 films are shown in Figure. S2, which confirm that part of the Fe_3O_4 films has been reduced to Fe. The unreduced Fe_3O_4 layers have the same out-of-plane orientations as the as-deposited Fe_3O_4 films shown in Figure. 2 in the main text and the orientations of the formed Fe layers are controlled by the Au substrates instead of the precursor Fe_3O_4 films. Therefore, three different types of Fe/Fe_3O_4 heterojunctions,

Au(100)/Fe(100)/Fe_3O_4(111), Au(110)/Fe(211)/Fe_3O_4(110), and Au(111)/Fe(110)/ Fe_3O_4(111), were produced.

These Fe/Fe_3O_4 heterojunctions are special because in this situation the orientations of both the Fe and Fe_3O_4 layer are controlled by the Au substrate. This property is not likely obtainable by direct deposition techniques in which the orientation of the upper layer is usually controlled by the directly contacted bottom layer. For example, if we first electrochemically deposit Fe on Au single crystal, then electrochemically deposit Fe_3O_4 on the pre-deposited Fe layer, the orientation of the Fe_3O_4 layer will be controlled by the Fe layer instead of Au substrate. This is proved by the X-ray diffraction θ-2θ scans and pole figure measurements (Figure S1) on the directly deposited Fe_3O_4/Fe heterojunctions on Au single crystals. The directly deposited Fe layer has the same out-of-plane orientation as the Fe layer reduced from precursor Fe_3O_4 (Figures. S1 & S2). But the orientations of the directly deposited Fe_3O_4 layers on the pre-deposited Fe layer are different from those directly deposited Fe_3O_4 on Au. In the situation of directly deposited Fe_3O_4/Fe heterojunctions on Au(100), the produced Fe_3O_4/Fe heterojunction is Fe_3O_4(100)/Fe(100)/Au(100). On Au(110), the Fe_3O_4 layer has two different out-of-plane orientations, (110) and (311). On Au(111), the Fe_3O_4 layer also has both (111) and (100) out-of-plane orientations. Thus, by partially reducing pre-deposited Fe_3O_4 films on single-crystalline Au substrates, we are able to produce singly oriented Fe_3O_4/Fe heterojunctions on Au(110) & Au(111), which are not producible by direct deposition.

Determination of the in-plane orientation of Fe films reduced from Fe_3O_4 films using X-ray pole figures. The in-plane orientations of the Fe films after reduction on

Au(100), Au(110), and Au(111) single crystals were measured by the X-ray pole figures as shown in Figures. S3e, S3e', and S3e'' (also in the main text Figure. 2g-i). The in-plane orientations of the Fe films could be solved by comparing the measured X-ray pole figures with the corresponding stereographic projection generated using CaRIne 3.1 software. A stereographic projection is a plot which shows the angular relationships of the faces in the crystal based on its crystallographic structure. The (110) pole figure of the Fe film on Au(100) in Figure. S3e shows four equally spaced ($\Delta\varphi = 90$ º) peaks appearing at tilt angle, χ, of 45 º, which matches with the interplanar angle between the {110} and {100} planes of Fe. Four peaks indicate that there is only one (100) domain of Fe. A Fe(100) stereographic projection probing Fe(110) type reflections is shown in Figure. S3a which matches with the Fe(110) pole figure in Figure. S3e except for that there is another broad peak at the center in the pole figure. This peak is due to the high-angle tail of the Au(200) peak at the 2θ angle of 44.431 º. Because the Au(200) peak is broad at the base as shown in Figure. 2a in the main text, the high-angle tail of the Au(200) peak extends past 44.671 º, which is the 2θ angle used in this Fe(110) pole figure. The Au(100) stereographic projection of Au probing Au(200) type of reflection is shown in Figure. S3c. If we overlap the stereographic projections of Fe in Figure. S3b and the stereographic projections of Au in Figure S3c (as shown in Figure S3d), the combined projections match the measured Fe(110) pole figure of the Fe film. Based on the matched stereographic projection, the in-plane orientation relationship of the Fe film and the Au substrate can be determined using the CaRIne software to point out any two orthogonal directions in the Fe and Au. Combining the out-of-plane orientation relationship based on the θ-2θ scan (Figure. 2a in the main text) with the in-plane orientation relationship based

on the pole figure (Figure. 2g), the epitaxial relationship for the Fe film on Au(100) is Fe(100)[001]//Au(100)[011].

On the Au(110), the (110) pole figure of Fe (Figure. 2h) shows two peaks at both $\chi \approx 30^{\circ}$ and 54° which are due to the reflection of in-plane [211] orientation of the Fe film. The presence of two peaks at $\chi \approx 54^{\circ}$ indicates two antiparallelly aligned {211} domains of Fe on Au(110) which matches with the corresponding stereographic projections in Figures. S3a' and S3b'. Because the peaks from these two domains overlap with each other at $\chi \approx 30^{\circ}$, there are only two peaks at $\chi \approx 30^{\circ}$. Similar to the situation in the Fe(110) pole figure on Au(100), the two more intense peaks at tilt angle of 45° arise from the Au(110) substrate and match well with the angle between the (110) and (200) planes of Au. Because the difference between the 2θ values of Au(200) and Fe(110) is only 0.24°, so the reflection of the (110) plane of Au is very intense. This causes the four peaks from the reflection of the in-plane [211] orientation of the Fe film at $\chi \approx 73^{\circ}$ (which are shown in the stereographic projection in Figure. S3b') to be absent because the intensity of high tilt angle reflection is too low compared with the strong reflection of (110) plane of Au substrate. Therefore, the epitaxial relationships for the two Fe domains on Au(110) are Fe(211)[$01\bar{1}$]//Au(110)[001] and Fe(211)[$01\bar{1}$]//Au(110)[$00\bar{1}$].

The (211) pole figure of Fe film on Au(111) shown in Figure. 2i is more complicated than the first two. It appears to have 6 "elongated" peaks at $\chi \approx 30^{\circ}$, 6 peaks at $\chi \approx 54^{\circ}$, and 9 weak peaks at $\chi \approx 73^{\circ}$, 3 of which are more intense than the others. These tilt angles are matched with the interplanar angles of {211} and {110} for Fe. The presence of 6 peaks at $\chi \approx 54^{\circ}$ suggests there are three {110} domains of Fe that are rotated by $\Delta\varphi = 120^{\circ}$ relative to each other. By comparing the (211) pole figure of Fe on

Au(111) with the Fe(110) stereographic projection probing the (211) types of reflections (Figures. S3a'' and S3b''), it reveals that the 6 "elongated" peaks at $\chi \approx 30^{o}$ are actually 12 peaks, each two of which are close to each other. The three stronger peaks at $\chi \approx 72^{o}$ and the one peak at the center are, again, due to the high-angle tail of the Au(222) peak. There should also be 12 peaks from the reflection of {110} planes of Fe at $\chi \approx 73^{o}$. However, some of them are absent because of the low intensity of the reflection at high tilt angle. Therefore, the epitaxial relationship for three domains of Fe film on the Au(111) substrate are Fe(110)[$1\bar{1}0$]//Au(111)[$\bar{1}\,\bar{1}2$], Fe(110)[$1\bar{1}0$]//Au(111)[$2\bar{1}\,\bar{1}$], and Fe(110)[$1\bar{1}0$]//Au(111)[$\bar{1}2\bar{1}$].

3. **SEM images of the precursor Fe_3O_4 film and the Fe film reduced from the precursor Fe_3O_4 film.**

The SEM images of the precursor Fe_3O_4 film and the Fe film reduced from the precursor Fe_3O_4 film as shown in Figure. S4 were taken on the Hitachi S4700 FE-SEM. The precursor magnetite film has the crystal size about 200-300 nm. After the reduction, the Fe film has the crystal size about 100-150 nm.

4. **Hysteresis loops of the as-deposited Fe_3O_4 film and the Fe film after reduction on Au(110).**

The hysteresis loops of the as-deposited Fe_3O_4 film and the Fe film after reduction on a Au(110) single crystal are measured in the Quantum Design Physical Property Measurement System (PPMS, San Diego, CA) using the VSM mode. The Au(110) single crystal used in this experiment has a diameter of 5 mm and a thickness of 1 mm.

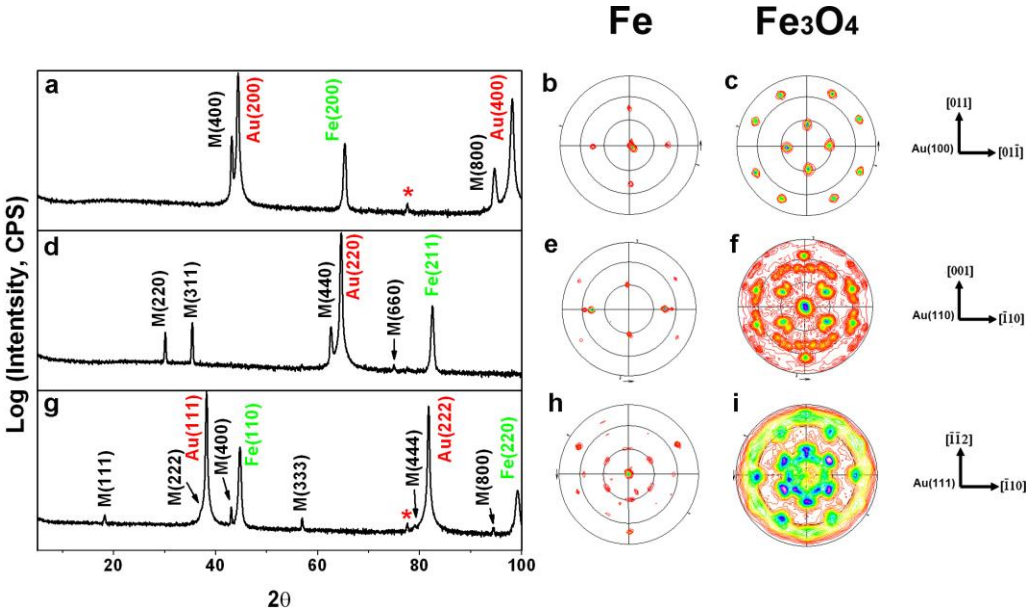

Figure S1. Figure S1. X-ray θ-2θ scans and pole figure measurements of electrochemically deposited Fe_3O_4/Fe heterojunctions on Au single crystals. X-ray θ-2θ scans of Fe_3O_4/Fe on (a) Au(100), (d) Au(110) and (g) Au(111). Fe(110) pole figures of Fe_3O_4/Fe on (b) Au(100) and (e) Au(110) and Fe(211) pole figure of Fe_3O_4/Fe on (h) Au(111). Fe_3O_4 (311) pole figures of Fe_3O_4/Fe on (c) Au(100), (f) Au(110), and (i) Au(111). (Peaks marked with a red star are from Au.)

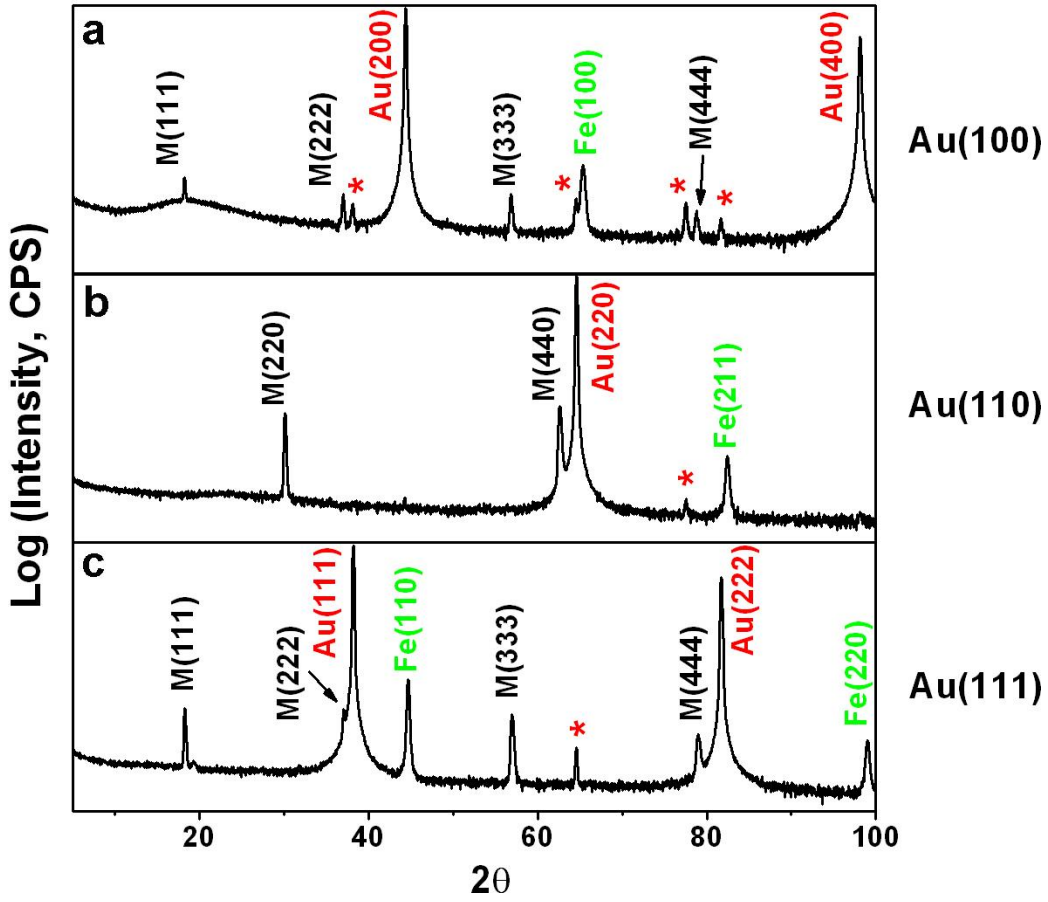

Figure S2. X-ray θ-2θ scans for partially reduced Fe_3O_4 films on (A) Au(100), (B) Au(110) and (C) Au(111) single crystals. (Peaks marked with a red star are from Au.)

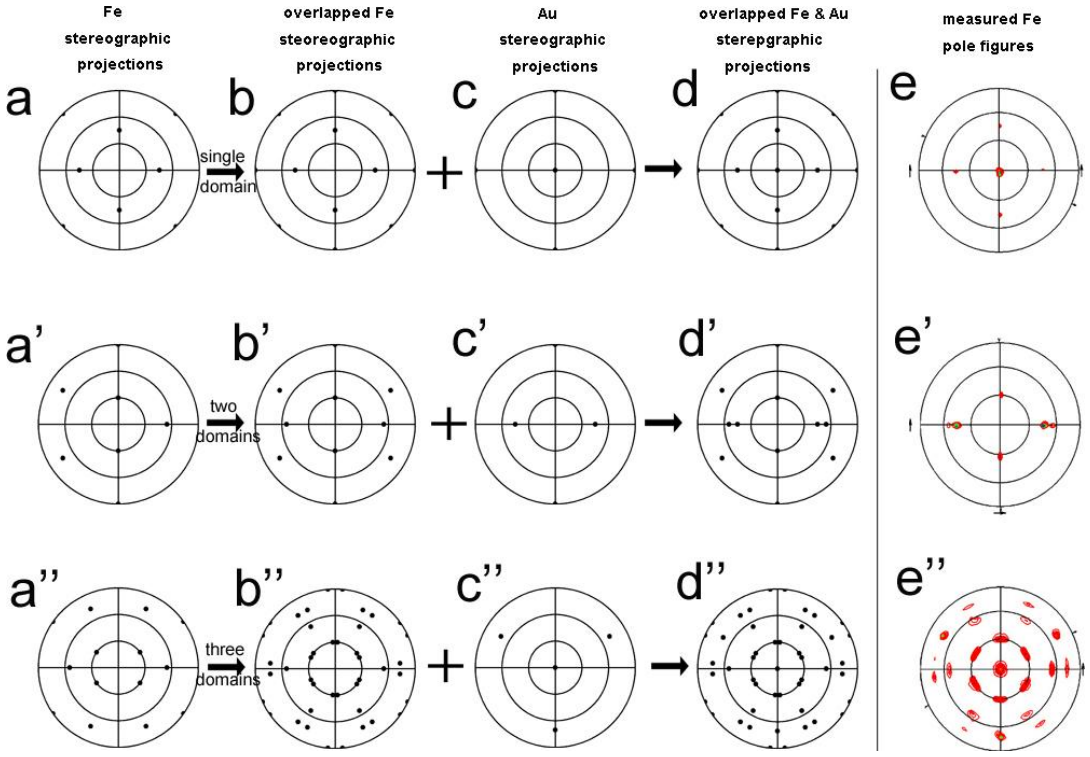

Figure S3. Fe(100) stereographic projection probing the Fe(110) reflection, Fe(211) stereographic projection probing the Fe(110) reflection, and Fe(110) stereographic projection probing the Fe(211) reflection are shown in a, a' and a'' (column a), respectively. Single domain of Fe(100) stereographic projection probing Fe(110) type of reflection is shown in b which remains the same as the one in a. Overlapping of two antiparalleled domains of Fe(211) stereographic projection probing Fe(110) type of reflection is shown in b'. Overlapping of three 120º rotated domains of Fe(110) stereographic projection probing Fe(211) type of reflection is shown in b''. Au(100) stereographic projection probing Au(200) type of reflection, Au(110) stereographic projection probing Au(200) type of reflection, and Au(111) stereographic projection probing Au(222) type of reflection are shown in c, c' and c'' (column c), respectively. The overlapping of corresponding Fe stereographic projection in column b and Au stereographic projection in column c are shown in column d. The measured (110), (110), and (211) pole figures of Fe on Au(100), Au(110) and Au(111) are shown in e, e', and e'', respectively.

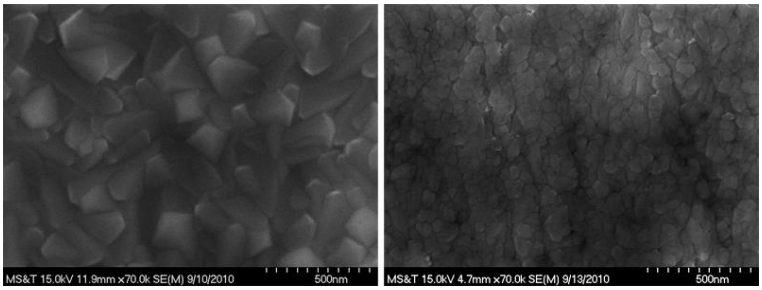

Figure S4. Top-view SEM images of the Fe_3O_4 film (left) and the Fe film (right) reduced from the Fe_3O_4 film on Au(111).

APPENDIX B.

SUPPORTING INFORMATION FOR PAPER II

1. Surface Morphology of the $Co_xFe_{3-x}O_4$ Films on Au Sputtered Glass.

The surface morphologies of the $Co_xFe_{3-x}O_4$ films deposited at different potentials were characterized using a Hitachi FE-S4700 scanning electron microscope (SEM) with an accelerating voltage of 15 kV and the ultra-high resolution mode. The films were electrodeposited on the Au sputtered glass substrates (the thickness of the sputtered Au layer is about 100 nm) from the standard $Co_xFe_{3-x}O_4$ deposition solution at -0.95, -0.97, -0.99, -1.01, and -1.03 $V_{Ag/AgCl}$. Each film was deposited by passing 1 C/cm^2 charge, resulting in a film thickness of about 2 μm. Top-view SEM images of these films are shown in Figure S1 below. For every investigated deposition potential, a dense film with a pyramidal-like morphology on the top surface was observed. All the films look similar under SEM except for the -1.03 V film, which is less facet and much smoother on the top surface.

2. Lattice Parameters of the $Co_xFe_{3-x}O_4$ Films Deposited at Different Potentials.

The crystal structure of the $Co_xFe_{3-x}O_4$ deposited at different potentials was characterized using a high-resolution Philips X-pert MRD X-ray diffractometer (XRD) with a CuKα1 radiation source (λ=0.154056). The films were electrodeposited on the Au sputtered glass substrates from our standard $Co_xFe_{3-x}O_4$ deposition solution at -0.95, -0.97, -0.99, -1.01, and -1.03 $V_{Ag/AgCl}$. Each film was deposited by passing 1 C/cm^2 charge, resulting in a film thickness of about 2 μm. X-ray diffraction (XRD) 2θ scans of these films are shown in Figure S2 with different colors and as labeled. Each of the films has a 2θ pattern which matches with that of the face-centered cubic (fcc) cobalt ferrite ($CoFe_2O_4$, or CFO for short). A closer analysis shows that the positions of the

corresponding peaks in these films slightly shift to higher 2θ angles as the deposition potential goes to more negative, which is probably due to the slightly different stoichiometries of these films. This also indicates that the lattice parameters of the films deposited at different potentials are slightly different.

In order to more accurately determine the lattice parameters of these $Co_xFe_{3-x}O_4$ films deposited at different potentials, Nelson-Riley function plots were used for processing the XRD data of each of these films. For the cubic system, the lattice parameter can be calculated according the following equation.

$$sin^2\theta = \frac{\lambda^2}{4a^2}(h^2 + k^2 + l^2) \qquad (1)$$

where θ is the diffraction angle of a peak shown in the 2θ scan, λ is the wavelength of the x-ray source, a is the lattice parameter, and h, k, and l are Miller indices of the corresponding diffraction peak. Theoretically, the lattice parameter of a cubic crystal can be derived from any diffraction peak in the 2θ scan. However, the answer will have less error if it is calculated with a high angle of θ. This can be done by putting the lattice parameter values calculated from every diffraction peak in the 2θ scan as a function of the Nelson-Riley function $((\cos^2\theta/\sin\theta) + (\cos^2\theta/\theta))$, and extrapolating the linear fit of them to $\theta = 90°$. Although several other functions can be used to extrapolate the calculated lattice parameter values (such as θ, $\sin^2\theta$, etc.), the Nelson-Riley function is considered to give the best result. Thus, as shown in Figure S3 (a) to (e) we calculated the lattice parameter values of the $Co_xFe_{3-x}O_4$ films from all the diffraction peaks, put them in the Nelson-Riley function plots, linearly fit them, and extrapolate to $\theta = 90°$ to get the

most accurate lattice parameters. Figure 3S (f) is the overlap of the plots (a) to (e), which clearly shows the lattice parameter (at θ = 90 °) of the $Co_xFe_{3-x}O_4$ film change with the deposition potential.

3. Epitaxial Relationship of the $Co_xFe_{3-x}O_4$ film on a Au(111) Single Crystal.

The epitaxial relationship of the $Co_xFe_{3-x}O_4$ film on a Au(111) Single Crystal was determined by the XRD 2θ scan and pole figure measurements, which are shown in Figure 5 in the main text. The $Co_xFe_{3-x}O_4$ film shows a [111] out-of-plane orientation, based on the presence of the {111} family planes of the $Co_xFe_{3-x}O_4$ film in the XRD 2θ scan in Figure 5a. In addition, the (333) peak has a much higher intensity than other peaks, which indicates the presence of a [511] out-of-plane orientation. The observed <511> orientations are the result of the twinning on {111} planes. The in-plane orientation relationships between the $Co_xFe_{3-x}O_4$ film and the Au(111) substrate are determined by comparing the XRD pole figure measurements of the $Co_xFe_{3-x}O_4$ film and the Au substrate with the corresponding stereographic projections. The in-plane orientations of the Au substrate are easy to figure out and are shown by arrows with the directions in Figure 5b. However, determining the in-plane orientations of the $Co_xFe_{3-x}O_4$ film is more complicated. The (111) and (511) stereographic projections of $Co_xFe_{3-x}O_4$ probing (311) reflections are shown in Figure S4 (a) and (b). By comparing them with the (311) pole figure of $Co_xFe_{3-x}O_4$ in Figure 5b in the main text, it is determined that the spots in the pole figure at the tilt angles of 9.5 °, 41.0 °, 66.0 °, and 86.7 ° are due to [511] orientations and the spots at the tilt angles of 29.5 °, 58.5 ° and 80.0 ° are the overlapped reflections from [111] and [511] orientations. Single domain of the [511] orientation only

shows one spot at the tilt angle of 9.5 °based on the stereographic projection in Figure S4 (b) and there are 6 spots appearing in the measured pole figure. Therefore, 6 domains of [511] orientation are present. The number of (111) domain(s) could be 1 or 2 and is not easy to determine based on the comparison of the pole figure and the stereographic projections in Figure S4 (a), due to the overlapped diffraction spots of [111] and [511] orientations in the pole figure. However, if the similarities of the $Co_xFe_{3-x}O_4$ film and our previously deposited Fe_3O_4 film in crystal structure is considered, there are probably 2 antiparalleled domains of [111] orientation. In summary, the epitaxial relationships of the $Co_xFe_{3-x}O_4$ film and the Au(111) substrate are: $Co_xFe_{3-x}O_4[511](01\bar{1})//Au[111](0\bar{1}1)$, $Co_xFe_{3-x}O_4[511](0\bar{1}1)//Au[111](0\bar{1}1)$, $Co_xFe_{3-x}O_4[511](\bar{1}41)//Au[111](0\bar{1}1)$, $Co_xFe_{3-x}O_4[511](1\ \bar{4}\ \bar{1})//Au[111](0\ \bar{1}\ 1)$, $Co_xFe_{3-x}O_4[511](\ \bar{1}\ 14)//Au[111](0\ \bar{1}\ 1)$, $Co_xFe_{3-x}O_4[511](1\ \bar{1}\ \bar{4})//Au[111](0\ \bar{1}\ 1)$, $Co_xFe_{3-x}O_4[111](01\ \bar{1})//Au[111](0\ \bar{1}\ 1)$ and $Co_xFe_{3-x}O_4[111](0\bar{1}1)//Au[111](0\bar{1}1)$

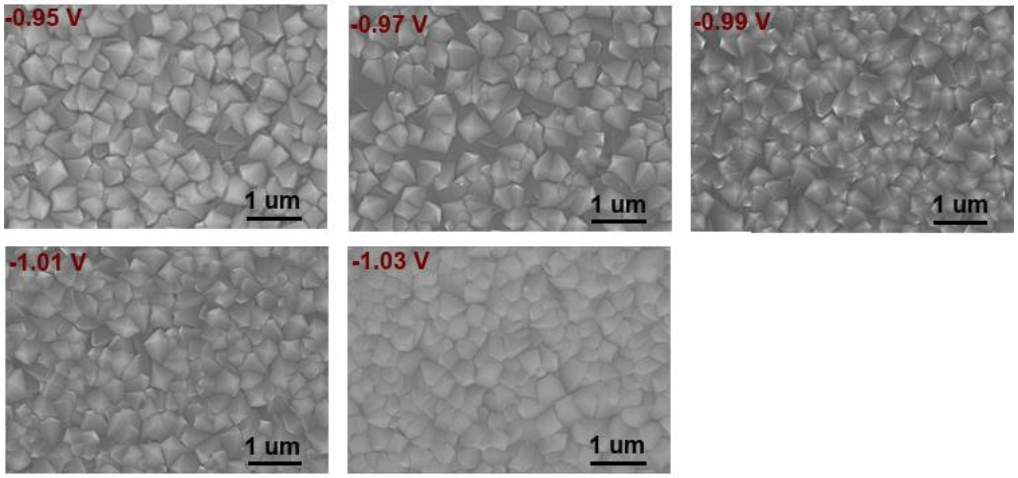

Figure S1. SEM images of the $Co_xFe_{3-x}O_4$ films deposited at different potentials on Au sputtered glass. The thickness of the films is about 1 μm.

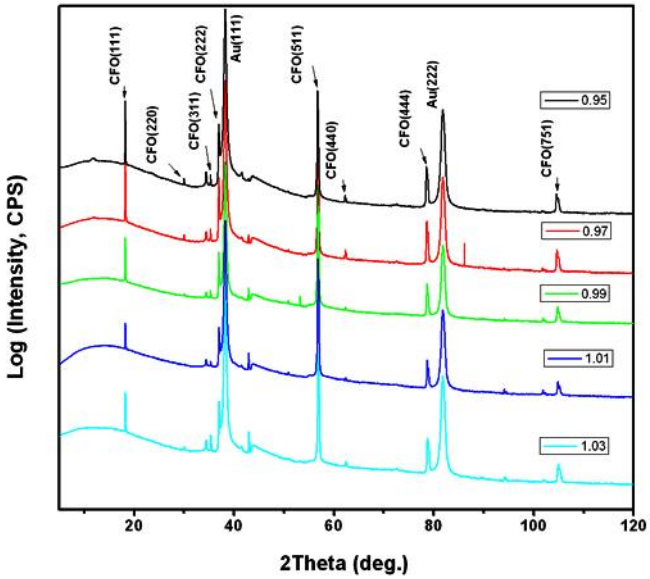

Figure S2. X-ray diffraction θ-2θ scans of the $Co_xFe_{3-x}O_4$ films deposited at different potentials. The unlabeled peaks and the hump at about 15 degree are from the buffer layers (mostly Cr) and the glass part of the substrates.

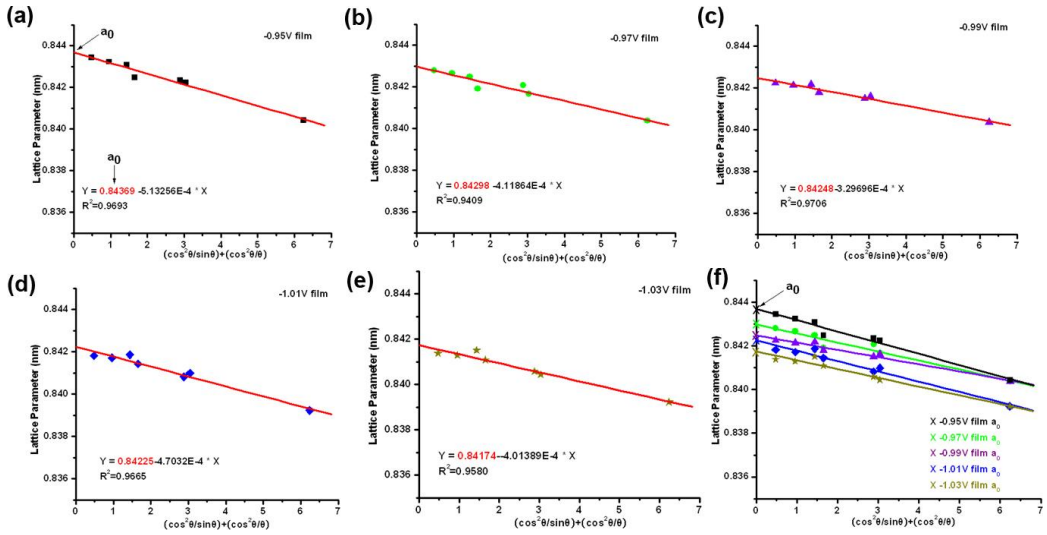

Figure S3. Nelson-Riley function plots for $Co_xFe_{3-x}O_4$ films deposited at (a) -0.95 V, (b) -0.97 V, (c) -0.99 V, (d) -1.01 V, and (e) -1.03 V vs. Ag/AgCl. (f) The overlapped plot of (a)-(e). The calculated lattice parameters based on every peak in the X-ray diffraction θ-2θ scans (Figure S2) are shown as the scattered data points in the plots. The straight lines the plots are the linearly fitted functions of the calculated lattice parameters. The accurate lattice parameters of $Co_xFe_{3-x}O_4$ films are obtained by extrapolating the linearly fitted lines to where the Nelson-Riley function is equal to zero (x=0), then taking the interception with Y axis as the lattice parameters of $Co_xFe_{3-x}O_4$ films.

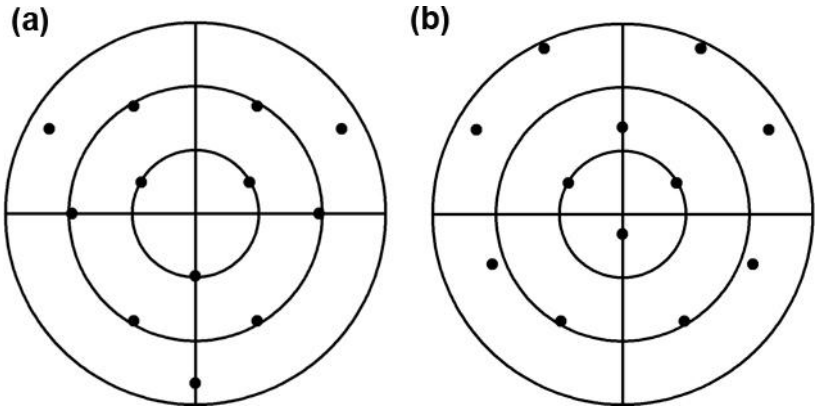

Figure S4. (a) (111) and (b) (511) stereographic projections of $Co_xFe_{3-x}O_4$ probing (311) reflections shown as the black spots.

APPENDIX C.

SUPPORTING INFORMATION FOR PAPER III

1. Electro-oxidation of the ligand (tartrate) – Cyclic voltammogram in the electrolyte without Co^{2+} ions

Figure S1 show a cyclic voltammogram (CV) measured in 6 mM tartrate in 2 M NaOH electrolyte at reflux. Two peaks in the CV can be observed, one in the forward scan with a maximum at a potential of about 175 mV (A) and a second one in the backward scan with a maximum at a potential of about 100 mV (B). Both of the peaks have positive charge. This is a characteristic feature for the tartaric acid electro-oxidation in alkaline electrolyte.[S1,S2,S3]

2. Experimental conditions, XRD pattern, and Raman spectrum of the Co_3O_4 film deposited on p^+-Si(110)

The Experimental conditions were the same as for deposition on a SS substrate unless otherwise mentioned. The film was deposited from a refluxing electrolyte at 400 mV vs. Ag/AgCl for 100 s. The substrate was H-terminated, p^+-Si(110) (boron doped, 0.005 Ω cm). The H-terminated substrate was prepared by immersing it in 5 % HF for one minute followed by immersion in hot HPLC H_2O for about 20 min. Finally, just prior to depositing, the substrate was immersed in 5 % HF for 10 s and rinsed with HPLC H_2O.

In the case of the deposition on Si it was not possible to use galvanostatic conditions as on other substrates. This is because at the current densities, which resulted in good quality deposits on the SS, the potentials at the Si substrate were in the range of the Si oxidation and no film deposition was noticed. Instead, the potentiostatic conditions were chosen. Figure S2a shows the XRD pattern of the Co_3O_4 film deposited on Si(110)

substrate at 400 mV. Although, the pattern is noisy, due to the thickness of the film and the grazing incident geometry employed, the peaks of the Co_3O_4 are revealed. The spinel Co_3O_4 structure formation on Si substrate was further confirmed by Raman spectroscopy investigations. Raman spectroscopy measurements were carried out using a Horiba Jobin-Yvon LabRam Aramis Microscope with a HeNe laser (λ=633 nm) as the excitation source with an incident power of about 0.5 mW to minimize sample heating. Figure S2b shows the Raman spectrum of the film deposited on Si substrate. The measured spectrum is in a very good agreement with that of Co_3O_4,[S4,S5] the peak at about 520 cm^{-1} originates from the Si substrate.

3. Determination of the in-plane orientation of Co_3O_4 film electrodeposited on Au(100) substrate

The (311) pole figure for Co_3O_4 on Au(100) is shown in the main text (Figure 5b). The pole figure was acquired by setting the 2θ angle to 36.853 ° and azimuthally rotating the sample from 0 to 360 ° (Φ angle), at tilt angles (ψ) from 0 to 90 °. The peaks are observed in the pole figure aligned in rings, 12 equally spaced peaks at each ring, at ψ angles of 29.5, 58.5, and 80 °. The low intensity peak in the center of the pole figure corresponds to the (311) plane, which was also observed (very low intensity) in the XRD pattern (Figure 5a in the main text). The in-plane orientation of the film could be resolved by comparing the measured pole figure with the corresponding stereographic projection generated using CaRIne 3.1 software. A single domain stereographic projection is shown in Figure S3a. By comparing the projection with the measured pole figure it is apparent that all the observed peaks match the interplanar angles between {311} and {111}.

However, the single domain projection does not predict 12 peaks at each of the rings but only 3 peaks at ψ=29.5 °, 6 peaks at ψ=58.5 °, and 3 peaks at ψ=80 °. This is because the Au(100) plane has 4-fold symmetry and the measured pole figure represents 4 domains of Co_3O_4(111) rotated by 90 °. This is clearly visible in the stereographic projection shown in Figure S3b, where 4 domains are rotated by 90 °. The intensity of peaks at each of the rings is predicted to be equal, as observed in the measured pole figure, because the peaks originating from different domains either do not overlap or overlap twice (at ψ=58.5 °).

The epitaxial relationship was determined with a help of the stereographic projections (Figure S3a,b) and comparing the azimuthal (Φ) scans of the Co_3O_4 film (2θ = 36.853 °, ψ = 29.5 °) and the Au(100) substrate (2θ = 64.7 °, ψ = 45 °) (Figure S3c). Based on the azimuthal scans, with a support of stereographic projections of the film and the substrate, it was found that the film is rotated in plane by 45 ° with respect to the substrate. Hence, considering the four domains, the epitaxial relationship is found to be $Co_3O_4(111)[11\ \bar{2}]||Au(100)<001>$.

4. Scanning electron microscope (SEM) images of the Co_3O_4 films deposited on SS substrates

Figure S4 shows the SEM images of the Co_3O_4 films deposited at different current densities from a refluxing electrolyte. It can be seen that films deposited at current densities higher than 0.5 mA cm^{-2} show significant cracking. This, most probably, cause the substrate to be exposed to the electrolyte. In the case of photoelectrochemical water splitting with n-Si as a substrate this would cause corrosion of the substrate (Co_3O_4 requires alkaline electrolyte).

5. LSVs of the Co_3O_4 films and substrates

Figure S5a shows the LSVs measured on a Co_3O_4 film as well as on the SS substrate in 1 M KOH at room temperature. The Co_3O_4 film is significantly more active than the substrate. The onset overpotential for oxygen evolution on Co_3O_4 appears at about 0.325 V, which is approximately 50 mV lower than on the SS substrate. Also the slope of the rising part of the curve (OER) is higher for the Co_3O_4 film compared to the SS substrate. Additionally, the LSVs measured on Co_3O_4 film deposited on Ti substrate together with the bare Ti substrate are shown in Figure S5b. From Figure S5b it is clear that the catalytic properties are related purely to the film, without any significant contribution of the substrate (Ti has negligible OER current noticed in the studied potential range). A peak observed just prior to the onset of OER is consisted with the oxidation of Co^{3+} to Co^{4+}.[S6,S7,S8]

6. Tafel plots of Co_3O_4 film deposited on SS without and with the electrolyte IR correction

Figure S6 shows the steady state polarization curves measured on a Co_3O_4 film in 1 M KOH at room temperature. The red curve was not corrected for electrolyte *IR*. The blue curve was corrected for the electrolyte *IR*. The resistance (R = 1.3 Ω) was determined with electrochemical impedance spectroscopy (EIS). At low current densities the correction is insignificant and does not affect the Tafel slope (49 mV dec^{-1}). However, at high current densities (higher than about 10 mA cm^{-2}) the curves deviate.

REFERENCES

(S1) Bohannan, E. W.; Kothari, H. M.; Nicic, I. M.; Switzer, J. A. *J. Am. Chem. Soc.* **2004**, *126*, 488.

(S2) Switzer, J. A. *Interface* **2004**, *winter*, 34.

(S3) Sarkar, S. K.; Burla, N.; Bohannan, E. W.; Switzer, J. A. *J. Am. Chem. Soc.* **2007**, *129*, 8972.

(S4) Hadjiev, V. G.; Iliev, M. N.; Vergilov, I. V. *J. Phys. C* **1988,** *21*, L199.

(S5) Wang, G.; Shen, X.; Horvat, J.; Wang, B.; Liu, H.; Wexler, D.; Yao, J. *J. Phys. Chem. C* **2009,** *113*, 4357.

(S6) Innocenzo G, C. *J. Electroanal. Chem.* **2002**, *520*, 119.

(S7) Casella, I. G.; Di Fonzo, D. A. *Electrochim. Acta* **2011**, *56*, 7536.

(S8) Singh, R. N.; Koenig, J. F.; Poillerat, G.; Chartier, P. *J. Electrochem. Soc.* **1990**, *137*, 1408.

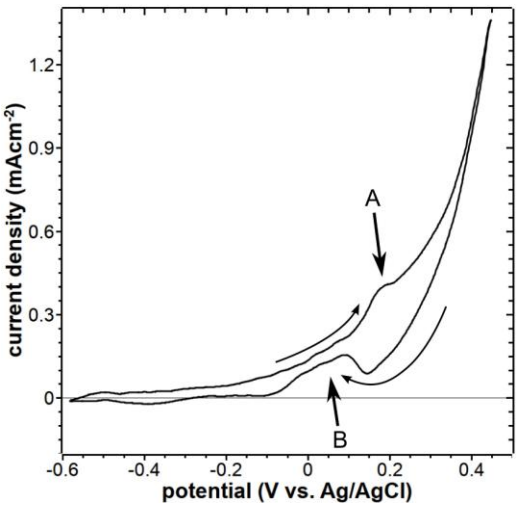

Figure S1. Cyclic voltammogram of the 6 mM tartrate in 2 M NaOH electrolyte. Au electrode, 103 ℃ (reflux), 50 mV s^{-1}.

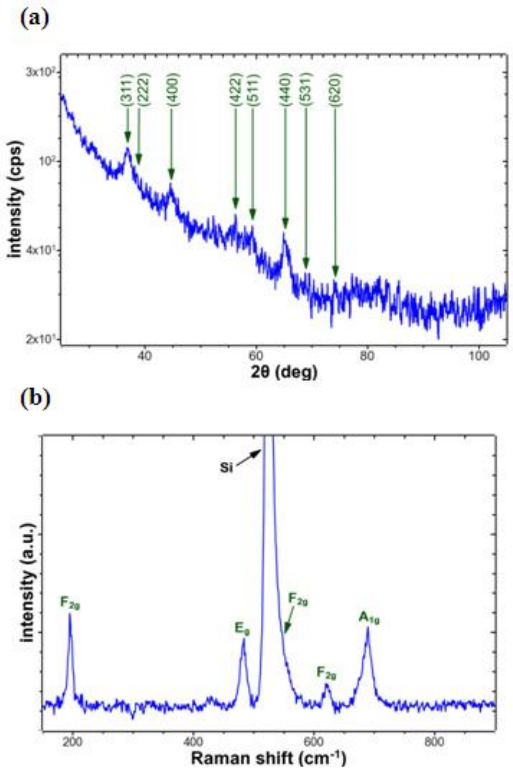

Figure S2. (a) XRD pattern (grazing incidence geometry) of a Co_3O_4 film deposited on H-Si(110) substrate with the indicated indices (JCPDS#42-1467), (b) Raman spectrum of a Co_3O_4 film deposited on H-Si(110) substrate with the indicated Raman-active phonon modes.[S4, S5] The film was deposited at 400 mV vs. Ag/AgCl for 100 s at 103 ℃ (reflux).

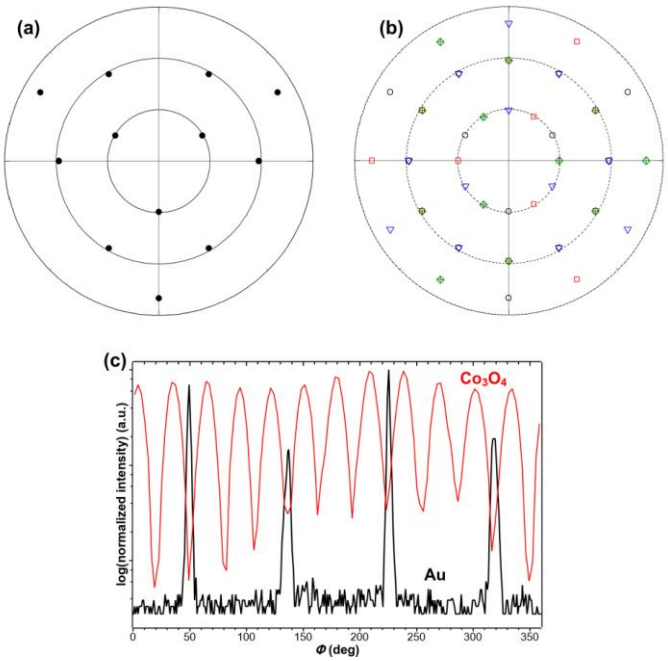

Figure S3. Stereographic projections of the (311) pole figures of Co_3O_4(111): (a) single domain, and (b) four superposed domains, different shapes and colors stand for different domains rotated in-plane by 90°. (c) Experimentally observed azimuthal (Φ) scans of the Co_3O_4 film (red) and Au substrate (black). Au(100) substrate, 0.25 mA cm^{-2}, 0.9 ℃ cm^{-2}, 103 ℃ (reflux).

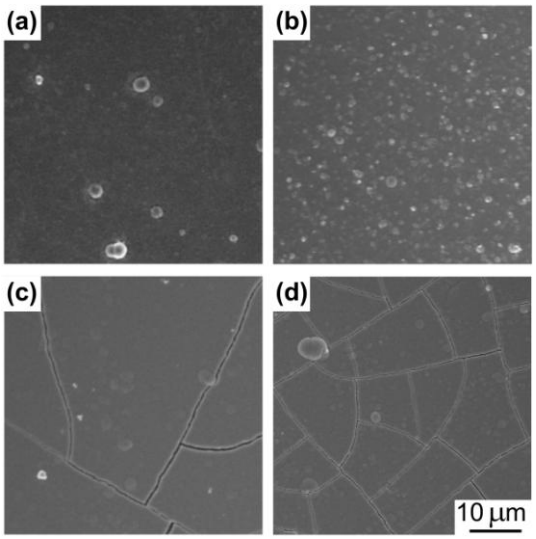

Figure S4. SEM images of the Co_3O_4 films deposited from a refluxing electrolyte at (a) 0.25 mA cm^{-2}, (b) 0.5 mA cm^{-2}, (c) 0.75 mA cm^{-2}, and (d) 1 mA cm^{-2}. SS substrate, 0.9 C cm^{-2}.

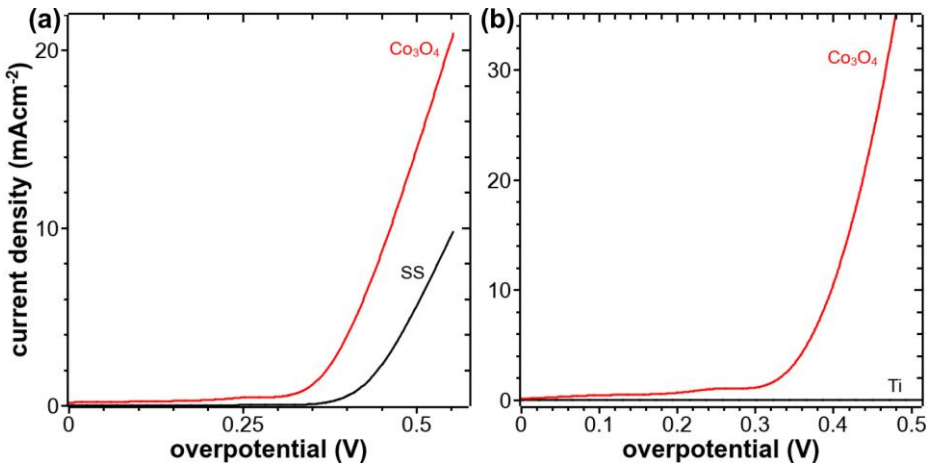

Figure S5. (a) LSV measured on the Co_3O_4 film (red) deposited on SS and the LSV of bare SS substrate (black). (b) LSV measured on the Co_3O_4 film (red) deposited on Ti and the LSV of bare Ti substrate (black). The films were deposited at 0.25 mA cm^{-2} from refluxing electrolyte at constant charge density of 0.9 C cm^{-2}.

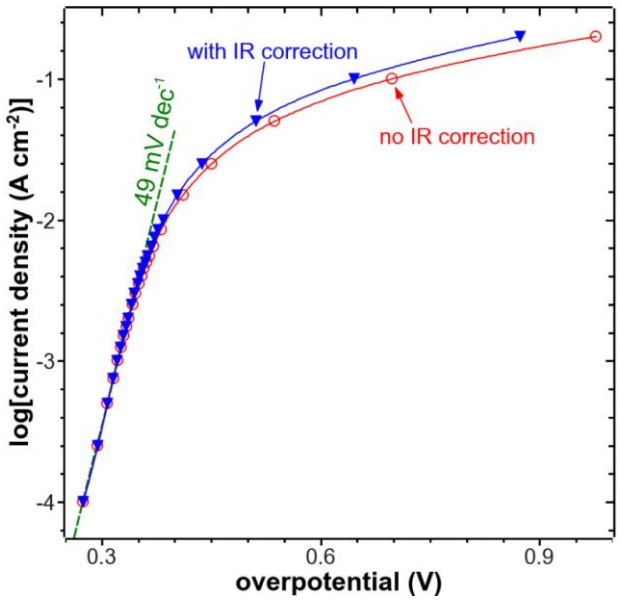

Figure S6. Steady state polarization curves of electrodeposited Co_3O_4 film without (red line and open circles) and with (blue line and triangles) the electrolyte *IR* correction. Co_3O_4 deposited at 0.25 mA cm^{-2} from a refluxing electrolyte on a SS substrate by passing a charge density of 0.9 C cm^{-2}. The overpotential was calculated with respect to the thermodynamic potential at pH of 14 of 0.401 V vs. NHE.

APPENDIX D.

ELECTROCHEMICAL REDUCTION OF MIXED METAL OXIDE THIN FILMS TO ALLOY THIN FILMS

INTRODUCTION

In Paper I in this dissertation, we showed that predeposited epitaxial Fe_3O_4 thin films can be electrochemically reduced to epitaxial Fe thin films.[1] We also mentioned that this method opens up possibilities to produce alloys by electrochemically reducing the corresponding mixed metal oxides. In Paper II in this dissertation, we showed that a series of Co-substituted Fe_3O_4 ($Co_xFe_{3-x}O_4$) with different Co/Fe ratios can be electrodeposited from the same deposition bath by simply varying the deposition potential.[2] Our preliminary results show that a series of CoFe alloy films with different Co/Fe ratios can be obtained by electrochemically reducing $Co_xFe_{3-x}O_4$ thin films with different Co/Fe ratios. Moreover, the Co/Fe ratio in the final CoFe alloy is almost the same as in the precursor $Co_xFe_{3-x}O_4$ thin film.

EXPERIMENTS

The $Co_xFe_{3-x}O_4$ thin films used for the electrochemical reduction experiments were electrodeposited onto Au-sputtered glass substrates from a stirred solution containing 50 mM Fe^{3+}, 50 mM Co^{2+}, 100 mM triethanolamine (TEA), and 2 M NaOH at 80 ℃ by applying constant potentials of -0.97, -0.99, -1.01, and -1.03 V vs. Ag/AgCl. These $Co_xFe_{3-x}O_4$ thin films were then electrochemically reduced in 2 M NaOH at room-temperature by applying a constant potential of -1.22 V vs. Ag/AgCl. X-ray diffraction (XRD) θ-2θ scans were used to characterize the structures of the $Co_xFe_{3-x}O_4$ films before and after the reduction. A Hitachi field-emission scanning electron microscope (FE-SEM) S4700 equipped with energy dispersive spectroscopy (EDS) was used to study the morphologies and the elemental compositions of the films before and after the reduction.

The K lines of Co and Fe in the EDS histograms were used to estimate the Co/Fe ratios in the precursor $Co_xFe_{3-x}O_4$ films and the final CoFe alloy thin films. The magnetic properties of the precursor $Co_xFe_{3-x}O_4$ thin films and the CoFe alloy thin films were measured using the Quantum Design Physical Property Measurement System (PPMS) with a Vibrating Sample Magnetometer (VSM) option normal to the film plane direction up to a field strength of 3.5 T. This filed is sufficient to saturate all the investigated samples.

RESULTS AND DISCUSSION

The XRD θ-2θ pattern of a $Co_xFe_{3-x}O_4$ thin film deposited at -1.03 V vs. Ag/AgCl and the CoFe film reduced from the precursor $Co_xFe_{3-x}O_4$ thin film are shown in Figure S1 as an example. As shown in Figure S1 (a), the $Co_xFe_{3-x}O_4$ thin film has a [111] preferred orientation in the XRD θ-2θ scan. The XRD θ-2θ patterns of the $Co_xFe_{3-x}O_4$ thin films deposited at different potentials are very similar except for slightly peak shifting, due to the composition differences in these films. After reduction, the XRD θ-2θ pattern of the CoFe alloy film matches with the cubic CoFe structure and has a [110] preferred out-of-plane orientation. The $Co_xFe_{3-x}O_4$ and CoFe thin films both show a preferred out-of-plane orientation because the Au-sputtered glass substrate has a [111] preferred out-of-plane orientation.

The surface morphologies of the $Co_xFe_{3-x}O_4$ thin films deposited on Au-sputtered glass substrates at different potentials and the CoFe alloy thin films reduced from the precursor $Co_xFe_{3-x}O_4$ thin films were characterized using SEM. There is no significant morphological difference between the $Co_xFe_{3-x}O_4$ thin films deposited at different

potentials. The morphologies of the CoFe alloy films reduced from the different $Co_xFe_{3-x}O_4$ thin films are also very similar. The top-view SEM images of a $Co_xFe_{3-x}O_4$ thin film deposited at -0.97 V vs. Ag/AgCl and the CoFe alloy film reduced from this $Co_xFe_{3-x}O_4$ thin film are shown in Figure S2 (a) and (b), respectively. It can be seen that the $Co_xFe_{3-x}O_4$ film has a pyramidal-like morphology on the top surface with a crystallite size of about 0.5 to 1 μm, whereas the CoFe alloy film has a particle-like top surface with a much smaller crystallite size of about 100 to 150 nm.

The atomic percent Co concentrations in the precursor $Co_xFe_{3-x}O_4$ films deposited at different potentials and the CoFe films after reduction were also measured by using EDS and are listed in Table 1. The EDS results show that the Co content in the CoFe alloy film after reduction is almost the same as in the corresponding precursor $Co_xFe_{3-x}O_4$ film. Since we can control the Co/Fe ratio in the $Co_xFe_{3-x}O_4$ films by varying the deposition potential, the Co/Fe ratio in the CoFe alloy films produced by electrochemical reduction of the $Co_xFe_{3-x}O_4$ films can also be controlled.

In order to further analyze the CoFe alloy product, magnetic investigations were performed. The out-of-plane hysteresis loops for $Co_{0.27}Fe_{2.73}O_4$ deposited at -1.03 V vs. Ag/AgCl and $Co_{0.1}Fe_{0.9}$ alloy produced by electrochemical reduction were measured (shown in Figure S3). Based on their out-of-plane hysteresis loops, the anisotropy fields of the $Co_{0.27}Fe_{2.73}O_4$ and $Co_{0.1}Fe_{0.9}$ alloy films are estimated (indicated by arrows in Figure S3) to be about 0.58 and 2.0 T, respectively. The measured anisotropy fields of the cobalt ferrite films grown by pulsed laser ablation on MgO and $SrTiO_3$ substrates are 0.668 and 0.596 T,[3] respectively. The value of the anisotropy field for $Co_{0.27}Fe_{2.73}O_4$ from our measurement is very close to the reported ones. The difference between these values

is probably due to the stress variances between the films on different substrates.[3] It is also know that near equiatomic CoFe alloys have the highest saturation magnetic flux density with B_S of 2.4 T.[4] Our estimated value (2.0 T) for $Co_{0.1}Fe_{0.9}$ is a little bit lower, which is probably due to a low Co content in our alloy film. However, the hysteresis loop for the $Co_{0.1}Fe_{0.9}$ film has a significantly larger anisotropy field than the precursor $Co_{0.27}Fe_{2.73}O_4$ film, which further proves the transformation of the oxide to the metal alloy.

CONCLUSIONS

Our preliminary results show that CoFe alloy films can be produced by electrochemically reducing Co-substituted Fe_3O_4. The Co/Fe ratio in the alloy film is almost the same as in the precursor $Co_xFe_{3-x}O_4$ film. This method could probably be used to produce other metal alloys from the corresponding mixed metal oxides. It opens up possibilities to produce alloys composed of metals with very different electrochemical reduction potentials (e.g., ZnFe alloys), which are not easy to make by direct electrodeposition.

REFERENCES

(1) He, Z.; Gudavarthy, R. V.; Koza, J. A.; Switzer, J. A. *J. Am. Chem. Soc.* **2011**, 133, 12358.

(2) He, Z.; Koza, J. A.; Mu, G.; Miller, A. S.; Bohannan, E. W.; Switzer, J. A. *Chem. Mater.*, to be submitted soon.

(3) Dhakal, T.; Mukherjee, D.; Hyde, R.; Mukherjee, P.; Phan, M. H.; Srikanth, H.; Witanachchi, S. *J. Appl. Phys.* **2010**, 107, 053914.

(4) Elhalawaty, S.; Carpenter, R. W.; George, J.; Brankovic, S. R. *J. Electrochem. Soc.* **2011**, 158, D641.

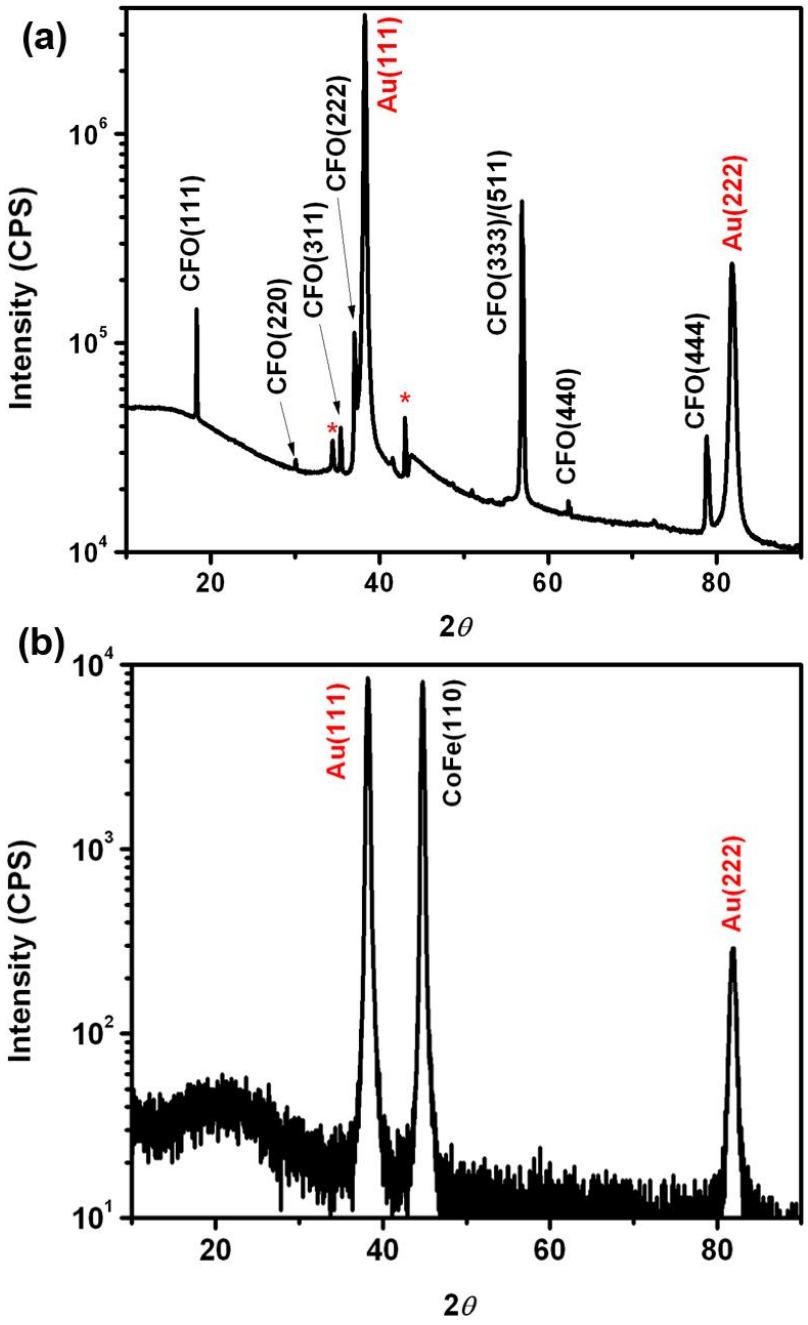

Figure S1. XRD θ-2θ scans of (a) a $Co_xFe_{3-x}O_4$ thin film deposited on a Au sputtered glass substrate at -1.03 V vs. Ag/AgCl and (b) the CoFe alloy film reduced from the precursor $Co_xFe_{3-x}O_4$ thin film by applying -1.2 V vs. Ag/AgCl in 2 M NaOH at room-temperature. CFO represents $Co_xFe_{3-x}O_4$. The peaks marked with red stars are from the Au-sputtered glass substrate.

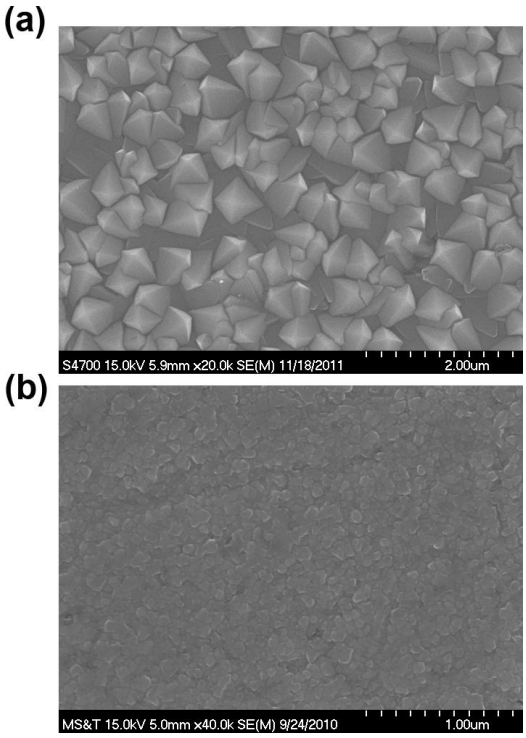

Figure S2. Top-view SEM images of a $Co_xFe_{3-x}O_4$ film deposited on a Au sputtered glass substrate at -0.97 V vs. Ag/AgCl and the CoFe alloy film reduced from this $Co_xFe_{3-x}O_4$ film.

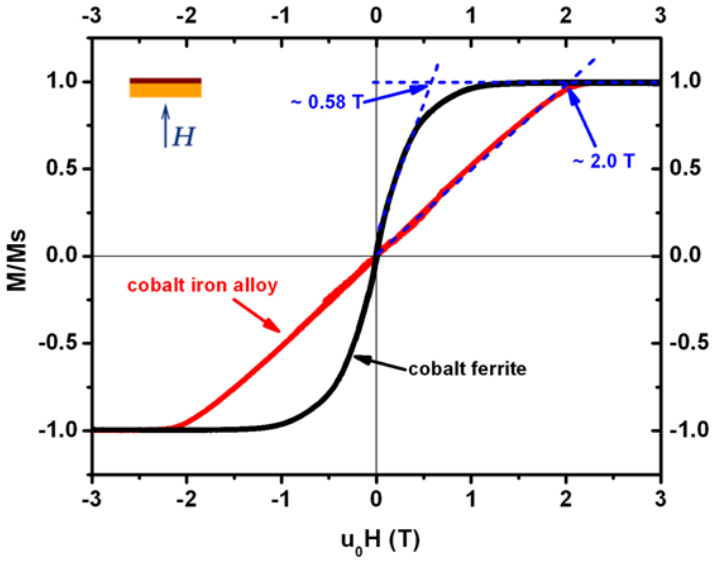

Figure S3. Out-of-plane hysteresis loops for $Co_{0.27}Fe_{2.73}O_4$ deposited at -1.03 V and $Co_{0.1}Fe_{0.9}$ alloy produced by electrochemical reduction.

Table 2. Atomic percent Co concentrations in the precursor $Co_xFe_{3-x}O_4$ films and in the CoFe alloy films after reduction.

$Co_xFe_{3-x}O_4$ film deposition potential (V)	atomic Co concentration (%)	
	in $Co_xFe_{3-x}O_4$ films	in CoFe films
-0.97	15.2	16.5
-0.99	12.9	12.4
-1.01	10.0	10.7
-1.03	9.1	10.5

APPENDIX E.

EPITAXIAL ELECTRODEPOSITION OF Co_3O_4 THIN FILMS

INTRODUCTION

Cobalt oxide (Co_3O_4) is of interest because of its several important applications. As a catalyst, Co_3O_4 is one of the most active metal oxides for CO oxidation.[1-3] It can also be used to catalyze other reactions such as methane combustion, NO_x reduction, trace ethylene oxidation, oxygen evolution reaction (OER) and oxygen reduction reaction (ORR).[4-10] Besides, Co_3O_4 is a promising anode material for lithium-ion batteries with a high theoretical capacity of about 890 mA h g^{-1}.[11,12]

Co_3O_4 has a normal spinel structure with a lattice parameter of 0.807 nm (space group *Fd3m*). Co_3O_4 nanocrystals with different shapes (e.g., cubes, sheets, wires, hollow spheres and tubes) have been synthesized via different methods.[13-19] It is known that Co_3O_4 nanocrystals with different shapes have different catalytic activities towards reactions such as CO oxidation and methane combustion, due to the differently exposed crystal planes of Co_3O_4.[1,4] Therefore, the synthesis of Co_3O_4 structures with certain exposed crystal planes is important for studying the catalytic-activity differences between the crystal planes of Co_3O_4 and enhancing the overall catalytic efficiency of Co_3O_4 as a catalyst. We have shown that crystalline Co_3O_4 films can be produced by electrochemical oxidation of Co(II) complexed with tartrate (tart) at elevated temperatures in Paper III in this dissertation.[20] Here, we report that epitaxial Co_3O_4 films can be electrodeposited by using the same method onto epitaxial Fe_3O_4 films predeposited on Au single-crystalline substrates. The orientations of the Co_3O_4 films completely follow the orientations of predeposited Fe_3O_4 films. Fe_3O_4 prelayers are used to control the orientations of Co_3O_4 films because Fe_3O_4 has a similar crystal structure and lattice parameter compared to

Co_3O_4. That is, the lattice mismatch between an epitaxial Co_3O_4 film and an epitaxial Fe_3O_4 film will be very small if they grow with the same orientation.

EXPERIMENTAL SECTION

Three types of Au single crystals, Au(100), (110), and (111) were used as the substrates. Before deposition, all the Au single crystals were electropolished for 30 s in a polishing solution containing 25% HCl, 25% ethylene glycol, and 50% ethanol at 55 ℃ by applying an anodic current density of 1.25 A/cm^2. The Fe_3O_4 prelayers were electrodeposited onto the electropolished Au single-crystalline substrates from a solution containing 87 mM Fe(III), 100 mM triethanolamine (TEA) and 2 M NaOH at 80 ℃ by applying a constant potential of -1.065 V vs. Ag/AgCl.[21-23] Each Fe_3O_4 layer was deposited by passing 0.5 C/cm^2 charge, resulting in a film thickness of about 1 μm. Co_3O_4 films were electrodeposited on Au and Ni single crystals (for comparison) and the Fe_3O_4 prelayers from a solution containing 5 mM Co(II), 6 mM tartrate, and 2 M NaOH at about 103 ℃ (refluxing electrolyte) by applying an anodic current density of 0.1 mA/cm^2 for 1 hr. All electrodeposition was done by using a Brinkmann PGSTAT 30 Autolab potentiostat.

The electrodeposited Co_3O_4/Fe_3O_4 films on Au single crystals were analyzed by using a high-resolution Philips X-Pert MRD X-ray diffractometer with a CuKα1 radiation source (λ = 0.154056 nm). The θ-2θ scans were obtained using the line focus mode with a hybrid monochromator consisting of a Göbel X-ray mirror and a Ge[220] 2-bounce, 2-crystal monochromator as the primary optic and a 0.18° thin film collimator as the secondary optic. The texture analysis (pole figure) was operated in the point focus mode

using a 2 mm × 2 mm crossed slit collimator with a Ni filter as the primary optic and a 0.27 ° parallel plate collimator with a flat graphite monochromator as the secondary optic. Pole figures were run by first setting the diffraction angle, 2θ, for a plane that was not parallel with the surface of the material. Then, the tilt angle, χ, was changed from 0° to 90 ° with an interval of 3 °, rotating the azimuthal angle at each tilt angle from φ = 0 ° to 360 ° with an interval of 3 °.

A dual FEI Helios NanoLab 600 FIB/FESEM was used to image the cross-section of a Co_3O_4/Fe_3O_4 film on a Au(110) single crystal. The duality of this instrument allows for site-specific FIB cross-sectioning and high resolution SEM imaging. For this work, the FIB was used to prepare a TEM lift-out. Prior to milling, a platinum layer was deposited to protect an area of the Co_3O_4/Fe_3O_4 film from the ion bombardment of the gallium source for the FIB milling. Two trenches were milled on either side of the protective Pt layer. An undercut was milled to release the sample from the bulk. The sample was then lifted from the bulk and attached with Pt to a special TEM grid. The attached sample was milled to a thickness of about 100 nm. This FIB prepared lift-out was then imaged with the high angle annular dark field (HAADF) STEM detector to image the double-layer structure of the Co_3O_4/Fe_3O_4 film. Energy dispersive spectroscopy (line scan mode) was used to further identify the Co_3O_4 and Fe_3O_4 layers respectively and show the sharp edge between the Co_3O_4 and Fe_3O_4 layers.

RESULTS AND DISCUSSION

Epitaxial electrodeposition of Co_3O_4 thin films onto Au(100) single crystals has been shown in Paper III in this dissertation.[20] The Co_3O_4 film deposited on Au(100)

single crystal has a [111] out-of-plane orientation. In order to compare the catalytic activities of different Co_3O_4 crystal planes towards certain reactions, epitaxial films of Co_3O_4 with other out-of-plane orientations are needed. However, the Co_3O_4 films deposited by the same method onto Au(110) and Au(111) single crystals all have a [111] preferred out-of-plane orientation as shown by the XRD θ-2θ scans of these films in Figure S1. Ni(110) and (111) single crystals were also used as substrates for the deposition of Co_3O_4. However, on Ni(110), Co_3O_4 grows with both [100] and [511] out-of-plane orientations, whereas on Ni(111), Co_3O_4, again, grows with a [111] preferred orientation (Figure S2).

Fe_3O_4 thin films were chosen to be the prelayers in order to control the out-of-plane orientation of the Co_3O_4 film because it has the same Bravais lattice (face-centered cubic) and a very similar lattice parameter compared to Co_3O_4 (0.8396 nm for Fe_3O_4 and 0.808 nm for Co_3O_4). Besides, we have shown that Fe_3O_4 can be epitaxially electrodeposited onto Au single crystals with different out-of-plane orientations.[23-25] The Fe_3O_4 films deposited on Au(100), Au(110) and Au(111) single crystals have [100]/[111], [110] and [111] out-of-plane orientations, respectively. Fe_3O_4 and Co_3O_4 both have the spinel structure and very similar lattice parameters. The only difference is that Fe_3O_4 is an inverse spinel and Co_3O_4 is a normal spinel. It is known that an epitaxial film usually grows with a certain orientation which minimizes the lattice mismatch between the film and the substrate. Therefore, it is reasonable to speculate that a Co_3O_4 film grown on a Fe_3O_4 prelayer will follow the orientation of the Fe_3O_4 layer (with a small lattice mismatch of about 3.8%). The XRD θ-2θ scans of Co_3O_4 films deposited on Fe_3O_4 prelayers on Au single crystals are shown in Figure S3. The relationships of the

out-of-plane orientations of the Co_3O_4 films, Fe_3O_4 prelayers, and Au single crystal substrates are $Co_3O_4(100)\&(111)//Fe_3O_4(100)\&(111)//Au(100)$, $Co_3O_4(110)//Fe_3O_4(110)//Au(110)$, and $Co_3O_4(111)//Fe_3O_4(111)//Au(111)$. That is, the Co_3O_4 films deposited on Fe_3O_4 prelayers do follow the out-of-plane orientations of the Fe_3O_4 prelayers.

Texture analysis was used in order to probe the in-plane orientations of the electrodeposited Co_3O_4 films and Fe_3O_4 prelayers. The (311) pole figures of Fe_3O_4 on Au(100) and Au(110), and the (220) pole figure of Fe_3O_4 on Au(111) are shown in Figure S4 (a)-(c), respectively. The (220), (311) and (220) pole figures of Co_3O_4 on Au(100), Au(110) and Au(111) with Fe_3O_4 prelayers are shown in Figure S4 (d)-(f), respectively. All the pole figures have a spot pattern instead of a ring pattern, which indicates all the Co_3O_4 and Fe_3O_4 films are not only out-of-plane oriented but also in-plane oriented. That is, they are epitaxial. The out-of-plane and in-plane orientations of the Co_3O_4 films all follow the orientations of the Fe_3O_4 prelayers. The epitaxial relationships of the Co_3O_4 films and Au substrates are the same as that of the epitaxial Fe_3O_4 films and Au single crystals.[20]

A high angle annular dark field cross-sectional image of a multilayer structure of Co_3O_4 on Fe_3O_4 on Au(110) is shown in Figure S5. The contrast between the Co_3O_4 and Fe_3O_4 layers is not very clear, due to the small Z-contrast between Co_3O_4 and Fe_3O_4 (i.e., their molar masses are very close). Thus, an energy dispersive spectroscopy line scan was used to determine the position of the interface of the Co_3O_4 layer and Fe_3O_4 layer as shown in Figure S5. The EDS image better shows double-layer structure. The yellow and

red lines representing Co and Fe clearly show the regions of Co_3O_4 and Fe_3O_4 layers. The Co_3O_4 and Fe_3O_4 layers each have a thickness of about 0.8 μm.

CONCLUSIONS

The results reported herein show that epitaxial Co_3O_4 thin films with different orientations can be electrodeposited onto single crystal Au substrates predeposited with a thin layer of epitaxial Fe_3O_4 film. The orientations of the Co_3O_4 layers completely follow the orientations the Fe_3O_4 prelayers, which is probably due to the similarity in crystal structures and lattice parameters of Fe_3O_4 and Co_3O_4. Synthesis of Co_3O_4 with selective orientations opens up the possibility to study the different catalytic activities of the different Co_3O_4 crystal planes towards certain reactions.

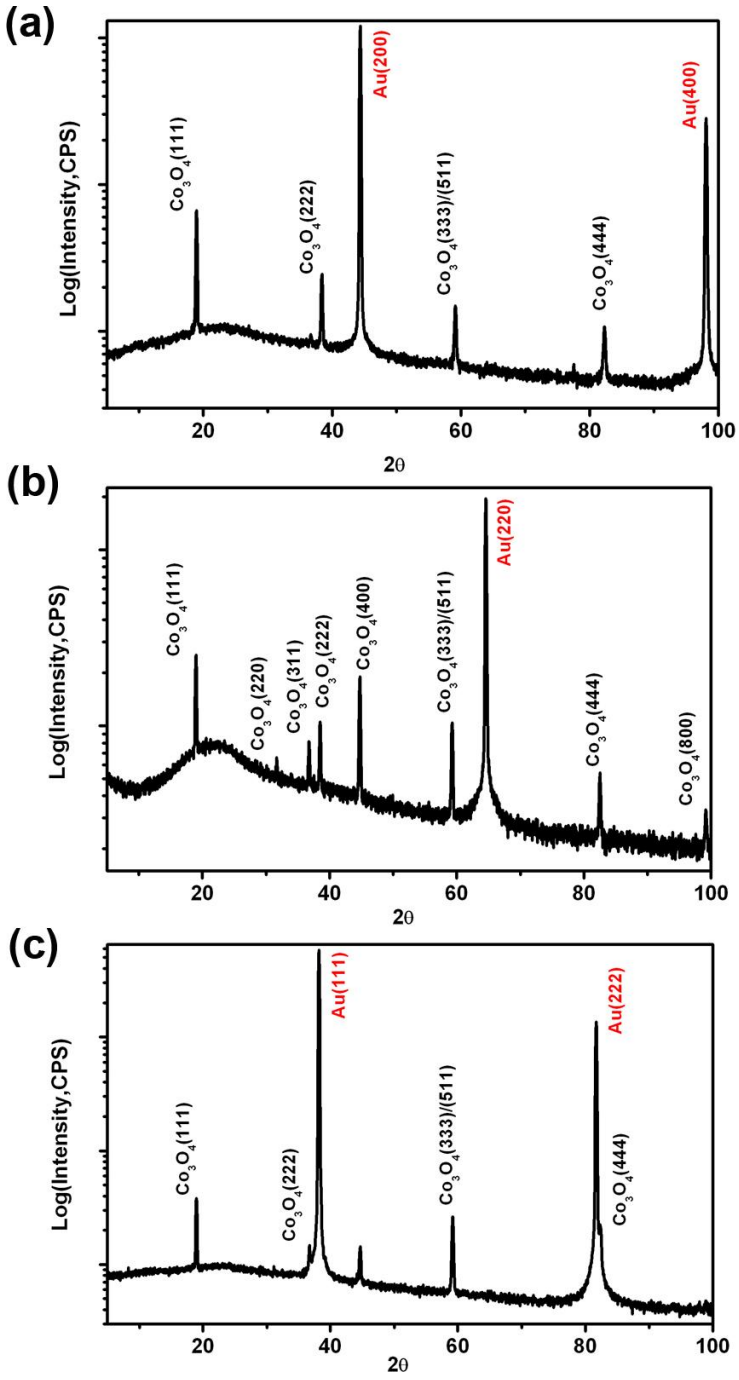

Figure S1. XRD θ-2θ scans of Co_3O_4 films directly deposited on (a) Au(100), (b) Au(110), and (c) Au(111) single crystals.

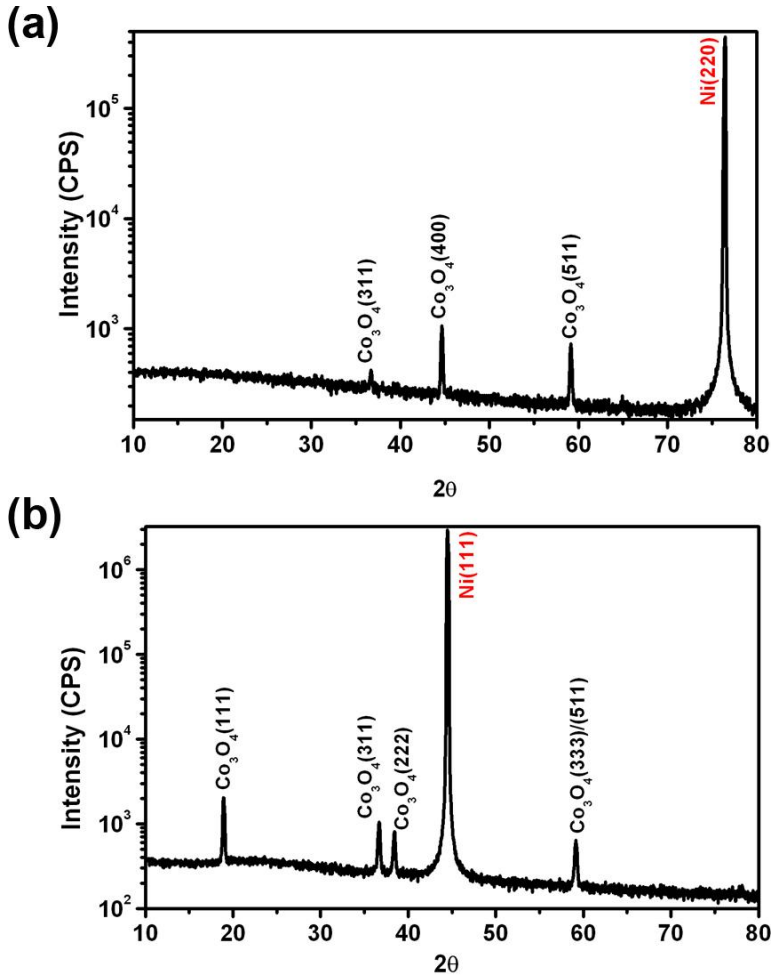

Figure S2. XRD θ-2θ scans of Co_3O_4 films directly deposited on (a) Ni(110) and (b) Ni(111).

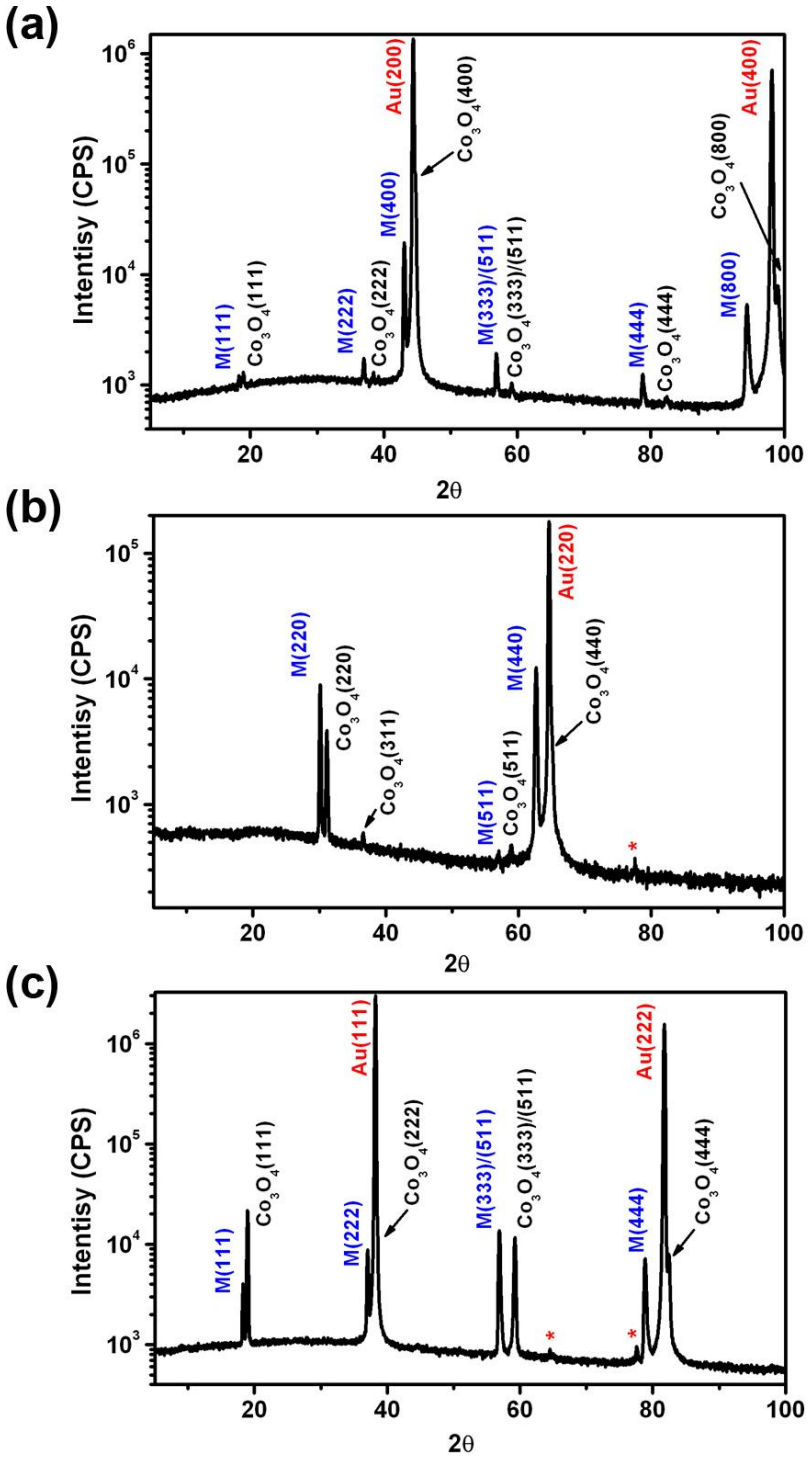

Figure S3. XRD θ-2θ scans of Co_3O_4 films deposited on Fe_3O_4 prelayers on (a) Au(100), (b) Au(110) and (c) Au(111). M represents magnetite (Fe_3O_4). Peaks marked with red stars are from the Au substrate.

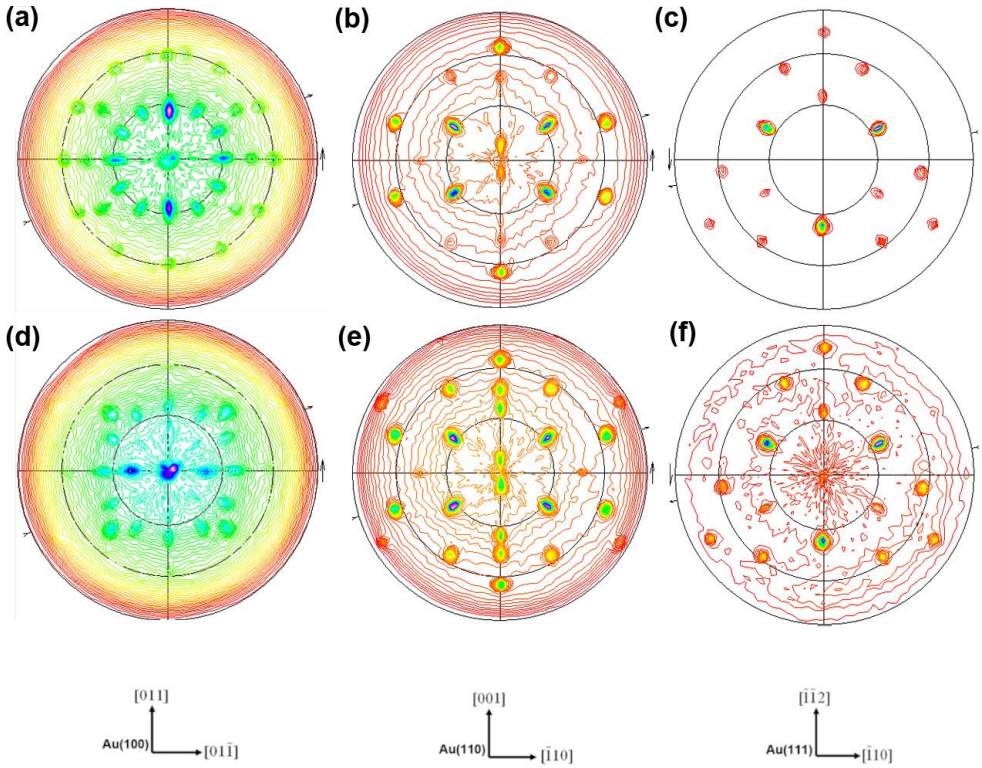

Figure S4. XRD pole figure measurements of electrodeposited Co_3O_4 on Fe_3O_4 prelayers on Au single crystals. Top row shows (311) pole figures of the Fe_3O_4 films on (a) Au(100), (b) Au(110), and (220) pole figure of Fe_3O_4 on (c) Au(111). Bottom row shows the (d) (220) pole figure of Co_3O_4 on Au(100), (e) (311) pole figure of Co_3O_4 on Au(110), and (f) (220) pole figure of Co_3O_4 on Au(111).

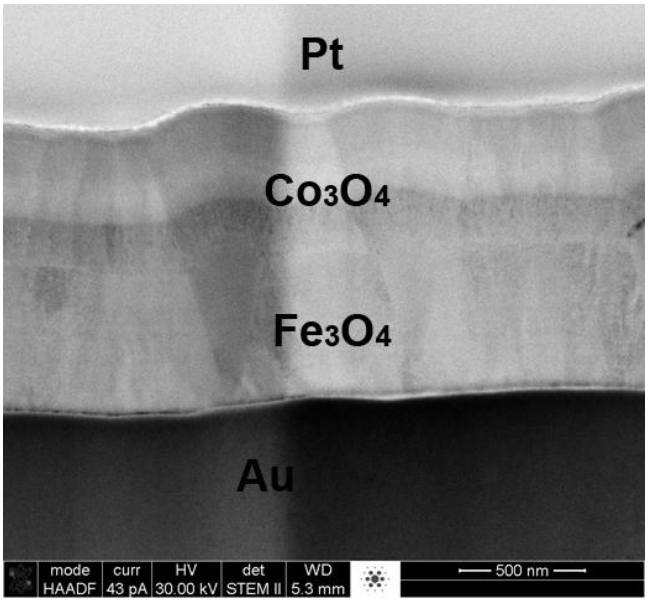

Figure S5. STEM-high angle annular dark field image of Co_3O_4 on Fe_3O_4 on Au(110). The top layer is the sputtered Pt and the bottom layer is Au substrate. Co_3O_4 layer is in contact with the top Pt layer and Fe_3O_4 is in contact with the bottom Au layer.

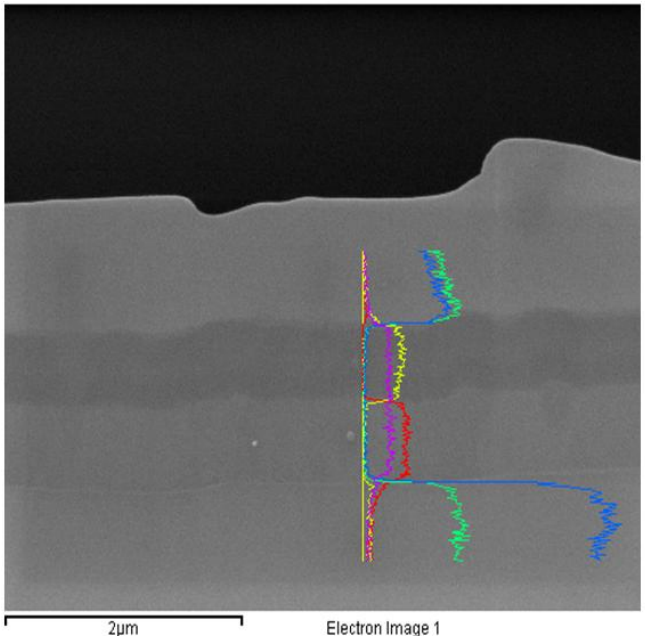

Figure S6. EDS line scan cross a Co_3O_4/Fe_3O_4 multilayer structure on Au(110). Yellow, red, purple, blue and green lines represent Co, Fe, O, Au and Pt signals, respectively.

REFERENCES

(1) Xie, X.; Li, Y.; Liu, Z. –Q.; Haruta, M.; Shen, W. *Nature,* **2009**, 458, 746-749.

(2) Yao, Y. Y. *J. Catal.*, **1974**, 33, 108-122.

(3) Perti, D.; Kabel, R. L. *ALChE J.* **1985**, 31, 1420-1440.

(4) Hu, L.; Peng, Q.; Li, Y. *J. Am. Chem. Soc.* **2008**, 130, 16136-16137.

(5) Fei, Z.; He, S.; Li, L.; Ji, W.; Au, C. –T. *Chem. Comm.* **2012**, 48, 853-855.

(6) Wichterlová, B. *Top. Catal.* **2004**, 28, 131-140.

(7) Ma, C. Y.; Mu, Z.; Li, J. J.; Jin, Y. G.; Cheng, J.; Lu, G. Q.; Hao, Z. P.; Qiao, S. Z. *J. Am. Chem. Soc.* **2010**, 132, 2608-2613.

(8) Liang, Y.; Li, Y.; Wang, H.; Zhou, J.; Wang, J.; Regier, T.; Dai, H. *Nat. Mater.*, **2011**, 10, 780-786.

(9) Singh, R. N.; Mishra, D.; Anindita; Sinha, A. S. K.; Singh, A. *Electrochem. Comm.* **2007**, 9, 1369-1373.

(10) Wang, G.; Cao, D.; Yin, C.; Gao, Y.; Yin, J.; Cheng, L. *Chem. Mater.* **2009**, 21, 5112-5118.

(11) Liu, H. –C.; Yen, S. –K. *J. Power Source* **2007**, 166, 478-484.

(12) Chou, S. –L.; Wang, J. –Z.; Liu, H. –K.; Dou, S. –X. *J. Power Source* **2008**, 182, 359-364.

(13) Xu, R.; Zeng, H. C. *J. Phys. Chem. B* **2003**, 107, 12643-12649.

(14) Ji, F.; Zeng, H. C. *Chem. Mater.* **2003**, 15, 2829-2835.

(15) Li, Y. G.; Tan, B.; Wu, Y. Y. *J. Am. Chem. Soc.* **2006**, 128, 14258-14259.

(16) Lou, X. W.; Deng, D.; Lee, J. Y.; Feng, J.; Archer, L. A. *Adv. Mater.* **2008**, 20, 258-262.

(17) Li, W. Y.; Xu, L. N.; Chen, J. *Adv. Funct. Mater.* **2005**, 15, 851-857.

(18) Wang, X.; Wu, X. –L.; Guo, Y. –G.; Zhong, Y.; Cao, X.; Ma, Y.; Yao, J. *Adv. Funct. Mater.* **2010**, 20, 1680-1686.

(19) Li, L. L.; Chu, Y.; Liu, Y.; Song, J. L.; Wang, D.; Du, X. W. *Mater. Lett.* **2008**, 62, 1507-1510.

(20) Koza, J. A.; He, Z.; Miller, A. S.; Switzer, J. A. *Chem. Mater.*, Submitted.

(21) Kothari, H. M.; Kulp, E. A.; Limmer, S. J.; Poizot, P.; Bohannan, E. W.; Switzer, J. A. *J. Mater. Res.* **2006**, 21, 293-301.

(22) Switzer, J. A.; Gudavarthy, R. V.; Kulp, E. A., Mu, G.; He, Z.; Wessel, A. J. *J. Am. Chem. Soc.* **2010**, 132, 1258-1261.

(23) Kulp, E. A.; Kothari, H. M.; Limmer, S. J.; Yang, J.; Gudavarthy, R. V.; Bohannan, E. W.; Switzer, J. A. *Chem. Mater.* **2009**, 21, 5022-5031.

(24) Sorenson, T. A.; Morton, S. A.; Waddill, G. D.; Switzer, J. A. *J. Am. Chem. Soc.* **2002**, 124, 7604-7609.

(25) Nikiforov, M. P.; Vertegel, A. A.; Shumsky, M. G.; Switzer, J. A. *Adv. Mater.* **2000**, 12, 1351-1353.

PUBLICATIONS

(1) Zhen He, Rakesh V. Gudavarthy, Jakub A. Koza, & Jay A. Switzer, "Room-temperature electrochemical reduction of epitaxial magnetite films to epitaxial iron films," *J. Am. Chem. Soc.*, **133**, 12358 (2011).

(2) Jay A. Switzer, Rakesh V. Gudavarthy, Elizabeth A. Kulp, Guojun Mu, Zhen He, & Andrew S. Wessel, "Resistance switching in electrodeposited magnetite superlattices," *J. Am. Chem. Soc.*, **132**, 1258 (2010).

(3) Zhen He, Jakub A. Koza, Guojun Mu, Andrew S. Miller, Eric W. Bohannan, & Jay A. Switzer, "Electrodeposition of epitaxial $Co_xFe_{3-x}O_4$ thin films and superlattices," *Chem. Mater.*, will be submitted soon.

(4) Jakub A. Koza, Zhen He, Andrew S. Miller, & Jay A. Switzer, "Resistance switching in electrodeposited VO_2 thin films," *Chem. Mater.*, **23**, 4105 (2011).

(5) Jakub A. Koza, Zhen He, Andrew S. Miller, & Jay A. Switzer, "Electrodeposition of crystalline Co_3O_4—a potent oxygen evolution catalyst," *Chem. Mater.*, under review.

(6) Rakesh V. Gudavarthy, Andrew S. Miller, Eric W. Bohannan, Elizabeth A. Kulp, Zhen He, & Jay A. Switzer, "Resistance switching in electrodeposited polycrystalline Fe_3O_4 films," *Electrochimi. Acta*, **56**, 10550 (2011).

(7) Martin R. McPhail, Jacob A. Sells, Zhen He, & Charles C. Chusuei, "Charging nanowalls: Adjusting the carbon nanotube isoelectric point via surface functionalization," *J. Phys. Chem. C*, **113**, 14102 (2009).

VITA

Zhen He was born on March 30, 1984 in Yueyang, Hunan, P. R. China. He moved to Changsha, Hunan, China in 1986 when his parents joined the Department of Chemistry and Chemical Engineering at Hunan Normal University. He fell in love with science in his early teens, when he spent a lot of time in his parents' lab. He received his Bachelor of Engineering (B.E.) degree in Materials Science and Engineering from Beijing University of Chemical Engineering in 2006. His B.E. work with Professor Gang Wei was focused on the electrodeposition of catalytic materials (e.g., PbO_2) for waste water treatments. During his undergraduate studies, he received several awards and scholarships, including the Outstanding Student Award (2002), People Scholarships (2003, 2005, & 2006), and "Color Masterbatch" Special Scholarship (2004).

In June, 2007 he joined in the Department of Chemistry at Missouri University of Science and Technology (known as the University of Missouri-Rolla at that time) to pursue his Ph.D. degree. He worked under the supervision of Dr. Jay A. Switzer from spring, 2008 to summer, 2012. His work in Dr. Switzer's group was focused on the electrodeposition and electrochemical reduction of epitaxial metal oxide thin films and superlattices that can be potentially used in spintronics and photoelectrochemical solar cells. During his Ph.D. studies, he was involved in several research projects supported by the Department of Energy (DOE) and National Science Foundation (NSF) of the United States. He also interned in the through silicon via (TSV) group at Novellus Systems, Tualatin, OR, in the summer of 2011 under the guidance of Drs. Mark Willey and Jon Reid. He received his Ph.D. degree in chemistry from Missouri University of Science and Technology in August, 2012.